JÖNKÖPING UNIVERSITY
School of Engineering

Influence of Molybdenum on mechanical and thermal properties in lamellar graphite cast iron

Influencia del Molibdeno sobre las propiedades mecánicas y térmicas en fundición laminar

PAPER WITHIN *Materials and Manufacturing Engineering*

AUTHOR: *Jose Manuel Amieva Llavona*

TUTOR: *Attila Dioszegi, Juan Carlos Hernando and Manuel Rendueles de la Vega*

JÖNKÖPING May 2016

This exam work has been carried out at the School of Engineering in Jönköping in the subject area Material and Manufacturing. The work is a part of the four-year Bachelor of Science in engineering program.
The authors take full responsibility for opinions, conclusions and findings presented.

Examiner: Nils-Eric Andersson

Supervisor: Juan Carlos Hernando, Attila Dioszegi and Manuel Rendueles de la Vega

Scope: 15 credits

Date: 2016-05-4

Abstract

In this work hypoeutectic lamellar graphite iron alloyed with seven different levels of molybdenum was studied in order to characterize its thermal and mechanical properties. Several tests were conducted and experimental data was collected from, laser flash (LFA), differential scanning calorimeter (DSC), dilatometer and tensile test.

Micrographs taken from the polished specimens were captured and studied through quantitative measurements of several parameters, e.g. graphite fraction, shape, form. Afterward, the same samples were colour etched with picric acid in order to perform a qualitative analysis of the matrix.

It was concluded from the data collected, that molybdenum has a significant influence in the UTS. Such influence, increases the UTS strongly with the amount of molybdenum. It was also found that the pearlitic matrix changes into ausferrite matrix, for the 0.96% of molybdenum, but ausferrite it is detected from 0.65% of molybdenum onwards. Regarding thermal properties, molybdenum does not have noticeable effect but it is possible to see a clear worsen in the conductivity in the specimen, which has ausferrite as matrix.

Graphite does not seem to have a clear behavior with the different concentration of molybdenum but in the other hand, the matrix shows clear differences as it was mention before.

During solid state reaction, it was detected a clear influence of molybdenum additions, where the latent heat and the volumetric change were measured during the eutectoid reaction and show a decreasing behavior for molybdenum contents above 0.65%.

Keywords

Lamellar cast iron, Molybdenum, Ausferrite, Solid state transformation, Ultimate tensile strain (UTS).

Summary

This thesis performed in the department of material and manufacturing at Jönköping University it is part of the project "Cast design" wherein the Department of Materials and Manufacturing of Jönköping University, Swerea Swecast, Volvo and Scania are involved.

In a previous stage of the project lamellar cast iron alloyed with Molybdenum have been studied with respect to the solidification and microstructure. However, this work seeks further understanding on how molybdenum influences on the mechanical and thermal properties in the lamellar graphite iron. The main research questions this work seeks to answer are:

a. What influence does the molybdenum have on mechanical properties?
b. What influence does the molybdenum have on thermal properties?
c. Does molybdenum have any influence on the graphite?
d. Does molybdenum have any influence on the microstructure?
e. How does molybdenum influence on the solid state transformation?

The first stage of the project, was the preparation of the material in the properly shape for the different experiments. The material provided by Volvo Powertrain was lamellar grey iron alloyed with seven different amounts of molybdenum, from 0.05 to 0.96%. After a tedious work in the workshop, all the samples were machined and got ready for the tests. For the thermal properties study, one sample from each composition was used for each device, Laser flash apparatus, dilatometer and differential scanning calorimetry. For the mechanical study it was done tensile test with four samples of each composition. Then with the data collected, it was found, different results and conclusions which were supported with the micrographs taken. Two kinds of micrographs were taken, first directly from the polished sample and then the samples were etched with picric acid and micrographed.

It was found out that molybdenum increases the UTS significantly, this increase is done in two steps, first molybdenum acts as a pearlite refiner until 0.65% of molybdenum content and with more molybdenum as ausferrite promoter. However, it was seen a worsen of the properties due to the carbides at 0.48% of molybdenum. From a thermal point of view, molybdenum does not have a clear effect. Nonetheless, the concentration that has ausferrite as matrix shown the worst thermal properties. Such ausferritic matrix, is achieved in the 0.96% but ausferrite it is detected from 0.65 onwards. From the polished samples the study micrographs did not show a noticeable behavior along the different concentrations of molybdenum. Moreover, during the solid state reaction the latent heat and the volumetric change show a decreasing behavior, especially when the concentration of molybdenum exceeds the 0.65% probably due to the presence of the ausferrite.

Resumen

Introducción

Esta tesis se centra en el efecto que tiene el Molibdeno sobre las propiedades térmicas y mecánicas de una función de hierro laminar. Para ello se ha estudiado las propiedades de siete aleaciones con diferentes contenidos de Mo y los resultados se han explicado y relacionado con la microestructura de cada aleación.

Esta tesis es la culminación de mi grado en Tecnologías Industriales de la Universidad de Oviedo y se ha llevado a cabo en el departamento de materiales y fabricación de la Universidad de Jönköpong. Dicho departamento está dentro de un proyecto común "Cast design" junto con Volvo, Scania y Swerea Swecast con el objetivo de alcanzar un mejor entendimiento sobre el papel de algunos aleantes con el fin de mejorar las propiedades de la fundición. Esta necesidad viene debida a la demanda de motores más eficientes los cuales deben soportar cada vez temperaturas y presiones más altas.

En fases anteriores de este proyecto, ya se ha estudiado el efecto del molibdeno en una fundición laminar durante la solidificación. Sin embargo, esta tesis se centra más en el efecto que tiene sobre las propiedades, térmicas y mecánicas de dicha fundición. Para ello esta tesis busca la respuesta a las siguientes preguntas:

a. ¿Qué influencia tiene el molibdeno sobre las propiedades mecánicas?
b. ¿Qué influencia tiene el molibdeno sobre las propiedades térmicas?
c. ¿Tiene el molibdeno alguna influencia sobre el grafito?
d. ¿Tiene el molibdeno alguna influencia sobre la microestructura?
e. ¿Cómo influye el molibdeno sobre la transformación de estado sólido?

Metodología de trabajo

En el documento original tras la introducción podemos encontrar un gran apartado de teoría en la que se habla de las redes cristalográficas, formas alotrópicas del hierro, diagrama hierro carbono y sus fases, los tipos de fundiciones que hay, también se profundiza en la fundición laminar, se explican los diagramas TTT, el molibdeno en las fundiciones y por último los ensayos de tracción en la fundición laminar. Todos estos apartados son llaves maestras para un buen entendimiento de este proyecto y se ha empleado un gran porcentaje del tiempo total en hacerla lo más resumida, entendible y amena posible para el lector. Por eso se considera que no tiene cabida en este resumen y se da paso a la metodología directamente.

Lo primero de todo fue recibir el material el cual se hizo en la fundición de Volvo. Dicho material como se ha dicho era fundición de hierro laminar aleado con 7 niveles diferentes de molibdeno los cuales iban desde el 0,05% hasta el 0,96%. Una tabla más detallada de todos los componentes de cada aleación se puede encontrar en el apéndice 9.1 pero debajo podemos ver una tabla con los elementos más significativos.

Tabla con los elementos más significativos.

ID del material	Composición química						
	C	**Si**	**Mn**	**Cr**	**Mo**	**Cu**	**CE**
A	3,40	1,89	0,57	0,15	**0,05**	0,90	3,90
2	3,26	1,89	0,60	0,14	**0,16**	0,82	3,91
3	3,24	1,89	0,60	0,13	**0,37**	0,78	3,89
4	3,28	1,9	0,56	0,13	**0,48**	0,76	3,93
5	3,25	1,88	0,56	0,13	**0,65**	0,80	3,89
6	3,26	1,89	0,58	0,13	**0,81**	0,81	3,91
8	3,24	1,86	0,61	0,13	**0,96**	0,93	3,87

El material era un cono con una altura de 150 mm y bases de 50mm y 60mm. Para sacar las muestras necesarias para hacer los experimentos se decidió cortar el cono en cuatro cuartos. De tal forma que de cada cono se usaron dos cuartos para mecanizar dos probetas para el ensayo a tracción y uno para los experimentos térmicos. Se puede ver el cono y la disposición de las probetas en la siguiente figura.

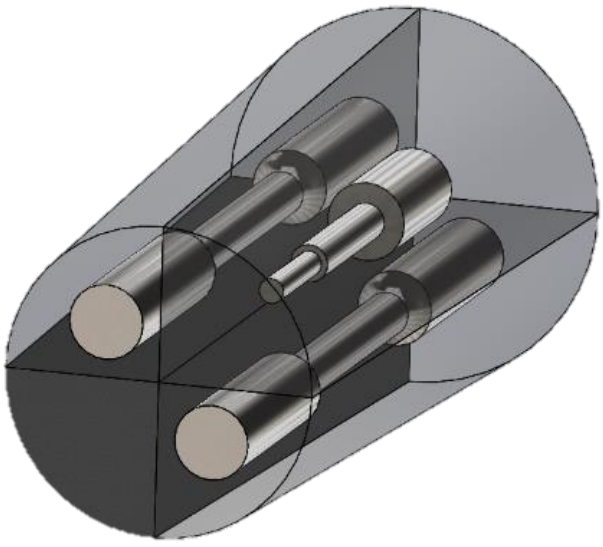

Figura esquemática del material original y las probetas.

Para analizar las propiedades térmicas el objetivo era calcular la conductividad térmica del material, para ello hizo falta utilizar el dilatómetro, el Differential Scaning Calorimeter (DCS) y el Laser Flash. Para utilizar estos equipos el cuarto de

cono que se había cortado, se vuelve a cortar para hacer un prisma cuadrangular y así cilindrarlo más fácilmente. El proceso de cilindrado fue llevado a cabo en un torno convencional, y se mecanizo una probeta por aleación y por experimento.

El dilatómetro utilizado fue el Netzsch Dilatometer 402C junto con el software Proteus. Este dilatómetro es un dilatómetro de varilla de empuje, con atmosfera controlada como se explica en la tesis, junto con todos los parámetros programados en este. La probeta utilizada es un cilindro de 12,5mm de diámetro y 4,375mm de altura y los resultados obtenidos de esta son el cambio dimensional del cilindro a lo largo de su eje con respecto a la temperatura. Con estos resultados es posible calcular el coeficiente lineal de dilatación gracias a la ecuación 2.

El DSC o Calorímetro de barrido diferencial es básicamente un dispositivo que mide la diferencia de temperatura entre una muestra y una referencia a lo largo de un ciclo térmico. Es utilizado para calcular temperaturas características, entalpias, calor especifico, etc. En este caso el dispositivo utilizado fue el Netzch DSC 404C pegasus y se utilizó para calcular el calor especifico. Este valor se calculó con el software Proteus también. La muestra necesaria para este dispositivo es un cilindro de 4mm de diámetro y 42,1mg, por lo que se mecanizo un cilindro de 0,5mm de altura y luego se ajustó al peso con una lija.

Por último, el Laser Flash fue utilizado para calcular la difusividad térmica del material, este dispositivo lo que hace básicamente es lanzar un pulso energético en forma de laser que calienta una superficie de la muestra, y mide el tiempo que tarda en llegar dicho impulso a la otra superficie. Con este tiempo y la formula 3 se puede calcular la difusividad. El dispositivo utilizado es el LFA 427 en el cual es necesaria una muestra de 12,5mm de diámetro y 4,375mm de altura.

Tras este largo proceso de mecanizado, mediciones (solo el Laser Flash tardaba 12 horas en medir un espécimen) y cálculo, se pudo calcular la conductividad gracias a la ecuación 4 en la que la única incógnita que nos quedaba era la densidad del material, la cual se calculó fácilmente gracias al principio de Arquímedes.

Por otra parte, para analizar las propiedades mecánicas se decidió hacer un ensayo de tracción. Dicho ensayo se llevó acabo la maquina Zwick/Roell Bus-hypu testing machine y siguiendo la normativa de Volvo. Donde las probetas debían tener un en su sección mínima un diámetro $7\pm0{,}04$ mm de diámetro y 50 mm de largo y una sección de 12 mm de diámetro en los extremos con una transición redondeada de 5mm de radio. Se mecanizaron cuatro probetas por cada aleación y los parámetros del ensayo de tracción cumplen con la norma SS-EN ISO 6892-1:2009. Dicho ensayo se hizo sin extensómetro, pero el hecho de no usarlo, no supuso una pérdida de calidad en la medida porque como se explica en la teoría el module E de la fundición laminar no sencillo de calcular, y se escapaba fuera del alcance de este proyecto. De todas maneras, todos los resultados como UTS, modulo E elongación etc. fueron medidos.

Una vez obtenidos todos los resultados de conductividad y del ensayo de tracción se procedió a analizar la microestructura del material con el fin de explicar los resultados obtenidos en los experimentos. Las superficies estudiadas fueron

obtenidas de las probetas utilizadas en el ensayo de tracción. Y se estudiaron tres superficies diferentes, de diferentes partes de la probeta como se puede ver en la siguiente figura.

Probeta del ensayo de tracción y las muestras utilizadas para examinar la microestructura.

Una vez cortadas las muestras para examinar la microestructura se procedió a montarlas en una pastilla de baquelita de 30 mm de diámetro. Una vez en la pastilla de baquelita se procedió a lijar y luego pulir la superficie. En total 8 etapas de lijado y pulido para acabar con una superficie de 1μm de rugosidad. Esta superficie era lo suficientemente buena como para poder hacer un análisis del grafito, dicho análisis se hizo con el software Olympus stream motion y siguiendo la norma ASTM A 247. Con lo que se analizaron quince micrografías de cada composición con una magnificación de 10X. Dichas micrografías fueron tomadas con el mismo patrón en todas las composiciones.

Una vez hecho el análisis del grafito, las muestras fueron atacadas con ácido pícrico, con el fin de poder ver la microestructura del material. Para el ataque con pícrico se necesitó calentar este hasta los 92 ^{0}C y luego se sumergió la muestra en él durante 10 minutos. Tras el ataque químico se tomaron diferentes micrografías y se podía ver claramente la microestructura. Todas las micrografías tomadas se tomaron con el microscopio Olympus GX71F. En la siguiente figura podemos ver ejemplos de las micrografías tomadas.

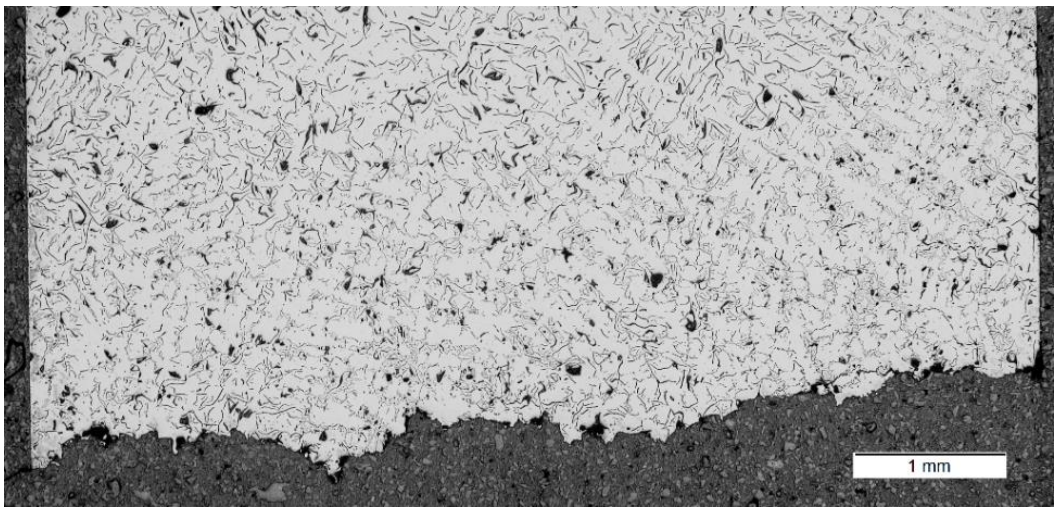

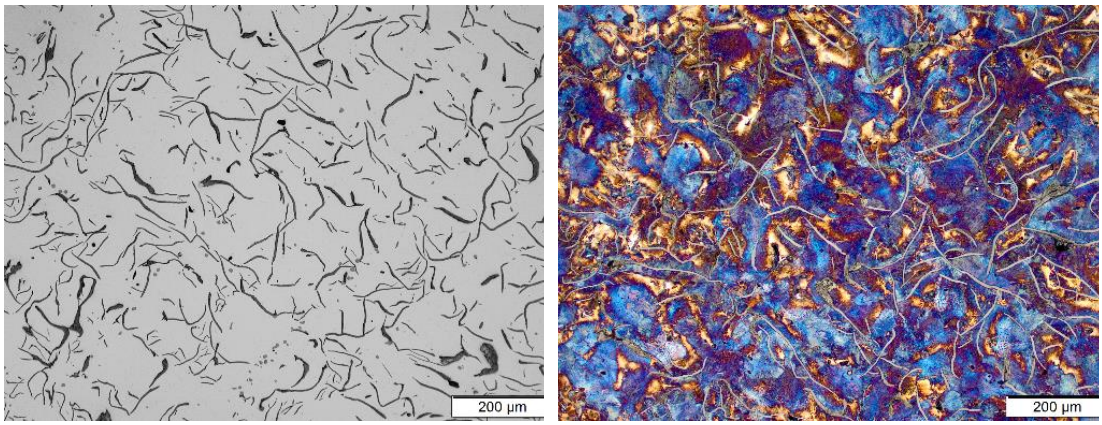

Arriba micrografía de la fractura, debajo a la izquierda micrografía utilizada para el análisis del grafito y a su derecha una micrografía tras el ataque con pícrico.

Resultados y análisis

Tras hablar de la metodología es hora de hablar de los resultados obtenidos, y como se ha dicho anteriormente, la microestructura se analizó para explicar los resultados obtenidos, con el fin de resumir se irán comentando los resultados de la microestructura según sean necesarios.

La carga de rotura obtenida en el ensayo de tracción es el valor más característico para este tipo de material como se explica en la teoría. Los resultados se pueden ver en el grafico inferior. En este se ve una clara tendencia creciente cuando se añade molibdeno. También se puede hacer distintas agrupaciones dentro de esta tendencia.

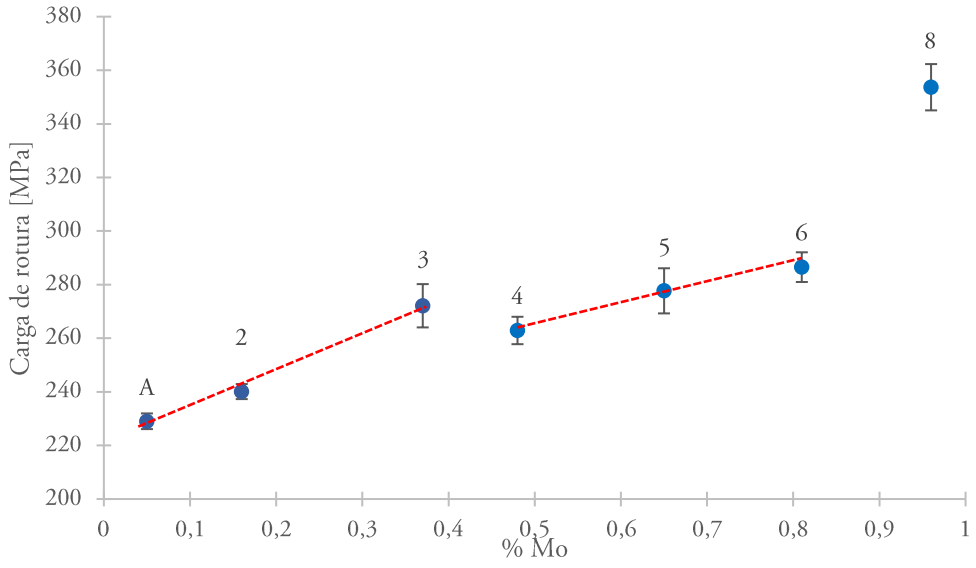

Resultados del ensayo de tracción.

Las diferentes tendencias se pueden explicar de la siguiente manera:

- Primera tendencia, composiciones A, 2 y 3: como se sabe de la teoría molibdeno es conocido por refinar la perlita, este refinamiento aumentaría la carga de rotura, pero para comprobar dicho refinamiento es necesario utilizar un microscopio electrónico el cual durante este proyecto no estuvo disponible y no se pudo demostrar. (Pero tras la defensa del proyecto y antes de escribir este resumen se me contrato y se midió y demostró que la perlita se refinaba). Por tanto, se buscó otra causa que explicase este fenómeno y se notó que el tamaño de grano se hacía más pequeño, fenómeno también puede explicar este aumento en la carga de rotura. Debajo podemos ver como el tamaño de grano se hace cada vez más pequeño.

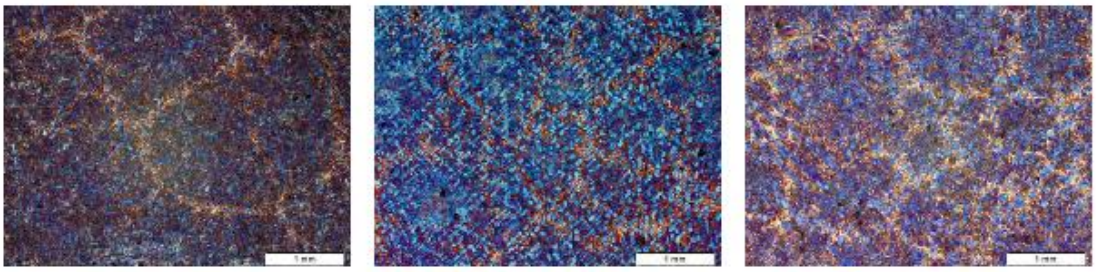

A 2 3

Microestructura de las composiciones A, 2 y 3

- Disminución de la carga de rotura entre las composiciones 3 y 4: aun que se aumenta el contenido de molibdeno entre estas composiciones se puede ver que la carga de rotura está ligeramente por debajo en la composición 4. Esto no era para nada esperado en este punto ya que el tamaño de grano seguía descendiendo y se esperaba un mayor refinamiento de perlita lo cual aumentaría la carga de rotura. Pero analizando la microestructura se vio que hay una cantidad significativamente mayor de carburos en la composición 4 que en la 3. Estos carburos son muy duros y lo que hacen es aumentar la fragilidad del material y disminuye la carga de rotura. Así que en este caso el refinamiento de la perlita y la disminución del tamaño de grano no es suficiente como para compensar el efecto de los carburos. Debajo se puede ver las micrografías en las que se señalan los carburos.

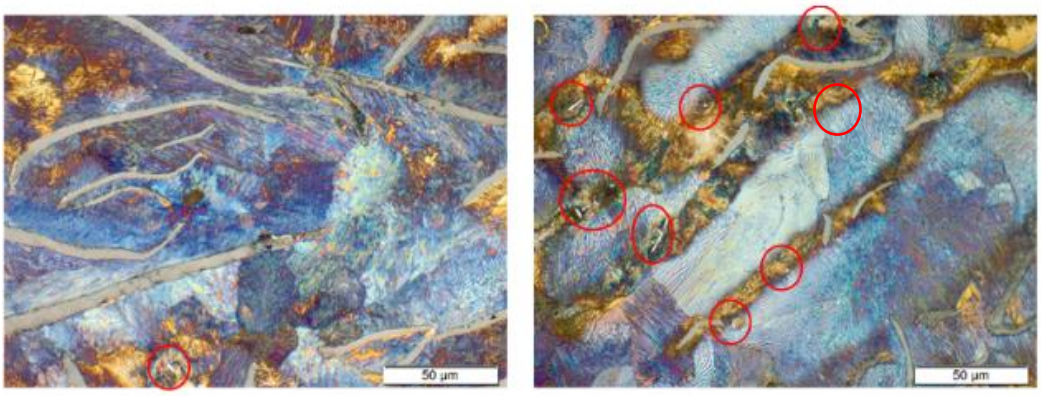

3 4

Microestructura composiciones 3 y 4

- Segunda tendencia, composiciones 4, 5 y 6: se podría pensar que a partir de la composición 3, (0,37% Mo) alear con molibdeno no tendría sentido porque la formación de carburos es tan grande que la carga de rotura desciende. Pero sin embargo no es así en las composiciones 5 y 6 se puede observar un aumento considerable de la carga de rotura. Analizando la microestructura una vez mas de estas composiciones podemos ver que hay más carburos, pero también que aparece una fase nueva, la esperada ausferrita. Esta ausferrita tiene unas propiedades mecánicas muy superiores a las que tiene la perlita, presente hasta ahora. Debajo podemos ver la ausferrita señalada en rojo.

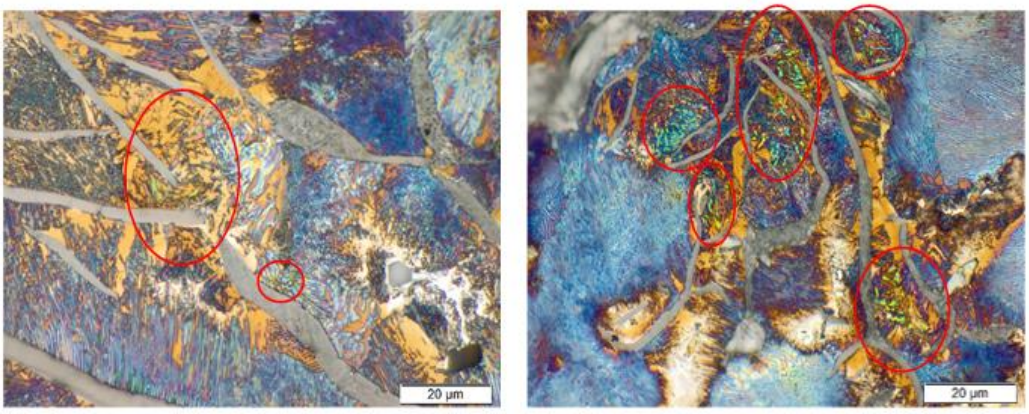

5 6

Microestructura de las composiciones 5 y 6

- Pico de la carga de rotura en la composición 8: Por ultimo podemos ver que la última composición muestra una carga de rotura muy alta que sale de la tendencia. La respuesta está en que la matriz perlítica que predominaba en todas las composiciones anteriores pasa a ser una matriz ausferrítica.

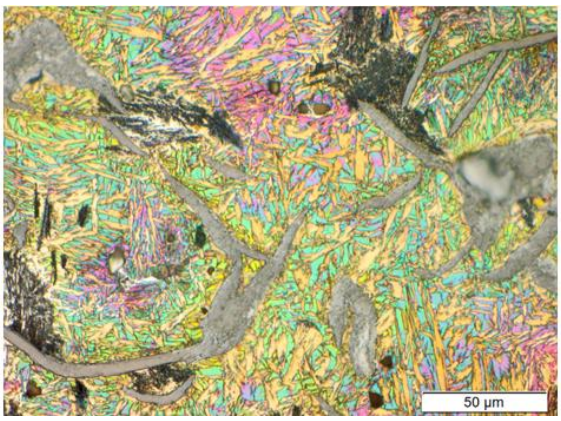

Microestructura de la composición 8

Por el lado de las propiedades térmicas, aunque también se analizó la influencia del molibdeno en el calor especifico, coeficiente de dilatación y la difusividad en este resumen nos centraremos en la conductividad que es el valor final obtenido a partir

de todos los valores antes mencionados. También se obtuvieron más resultados a parte de los necesarios para calcular la conductividad.

Por ejemplo, del dilatómetro, al ejecutarlo hasta los 950 ^{0}C se pudo ver el cambio volumétrico que tiene lugar durante la transformación de estado sólido donde la austenita se transforma en perlita (si enfriamos y viceversa si se calienta). Este cambio volumétrico viene dado por un cambio en la red cristalográfica. En el gráfico de debajo podemos ver tres curvas obtenidas en el dilatómetro en la que en verde se señala el cambio de estado sólido y en azul un cambio volumétrico alrededor de 450^{0}C que solo se encontró en la composición 6 y 8 y ligeramente durante el enfriamiento de la 5.

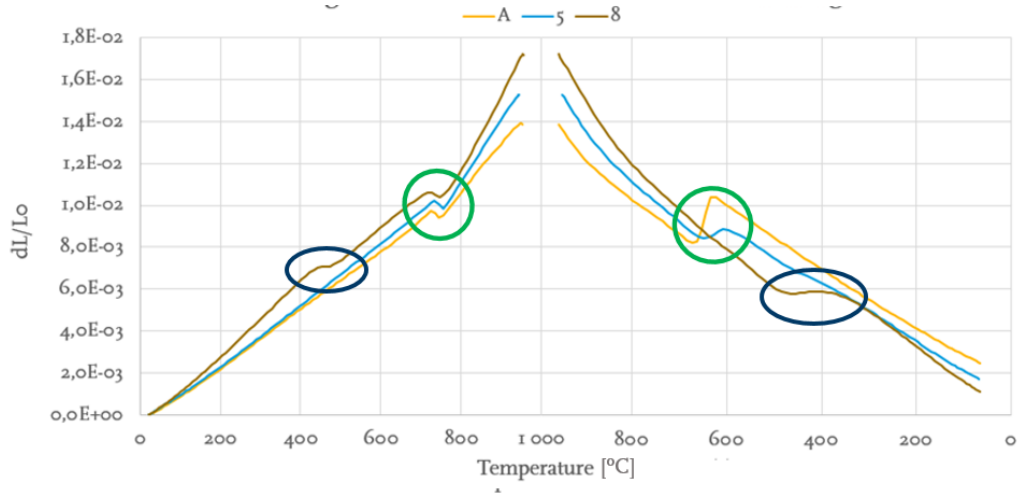

Curvas ejemplo del dilatómetro.

Como se puede ver en el grafico anterior el cambio volumétrico durante la transformación de estado sólido disminuye a medida que se añade molibdeno, llegando a desaparecer durante el enfriamiento en la composición 8. Este cambio volumétrico se midió y se comprobó que a medida que se añade molibdeno el cambio volumétrico es menor lo que quiere decir que menos austenita se está transformando en perlita. También se observó que en las composiciones con poco molibdeno durante el enfriamiento el cambio volumétrico era mayor que durante el calentamiento y en las composiciones con mayor contenido en molibdeno (5, 6 y 8) el cambio volumétrico era menor incluso llegando a desaparecer. Esto es porque una vez que se forma ausferrita el proceso térmico del dilatómetro es comparable a un proceso de austenización. Por otra parte, para explicar el cambio volumétrico que tiene lugar en torno a los 450 ^{0}C se dedujo una hipótesis en la cual se cree que dicho cambio volumétrico es debido a la deformación de la red cristalina FCC de la austenita, la cual al tener átomos de carbono intersticiales no es estable a temperatura ambiente (debido a los diferentes coeficientes de dilatación del C y el Fe) y para hacer sitio al carbono se deforma. Por eso, este cambio volumétrico solo está presente en las muestras que tienen más austenita, 5, 6 y 8 (las que tienen una transformación de estado sólido menor como se ve en las curvas del dilatómetro).

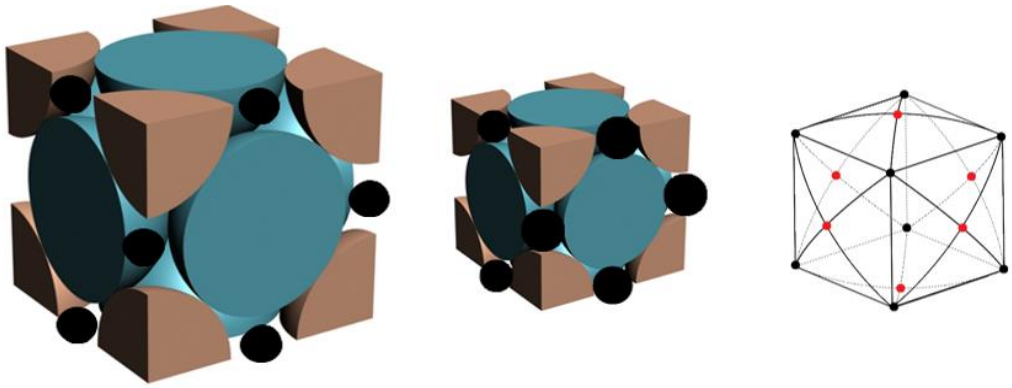

Red cristalográfica de la austenita, donde se muestra como estaría la red a: altas temperaturas, a la temperatura de saturación y a bajas temperaturas.

Por otro lado, del DSC a parte del calor especifico del material para calcular la conductividad, también se midió el calor latente del material. Con esta medición pudimos comprobar la importancia de la solidificación del material ya que durante este experimento el material fue refundido, y se comprobó que después de refundir el material y solidificar bajo unas mismas condiciones el calor latente se ordenaba claramente en función del molibdeno. Lo cual no pasa de igual modo durante el calentamiento. Y debido que el material vino de la fundición sin información del lugar que ocupaba la pieza en el molde, no se puede saber si la muestra medida procedía de un extremo del molde (enfriamiento más rápido) o del interior del molde (enfriamiento más lento).

Por último la conductividad obtenida se muestra en el grafico inferior. Esta se calculó por debajo de la transformación de estado sólido, ya que es el rango de temperatura que tiene iteres industrialmente. Además, tampoco se podría calcular durante dicha transformación ya que no hay coeficiente lineal de expansión. Podemos ver que las cuatro muestras con menos molibdeno tienen una conductividad muy parecida, y las que tienen más molibdeno es decir cuando aparece la ausferrita tienen una conductividad claramente inferior. Esto sería cierto si no fuese porque la composición 6 tiene la conductividad más alta, esto se debe a un resultado del calor especifico anormalmente alto. Se intentó repetir el experimento, pero el DSC se averió y no se pudo volver a hacer. Este valor tan alto puede deber a que el DSC es un aparato muy sensible en cual una simple mota de polvo puede afectar el resultado notablemente, también es tranquilizador que durante el enfriamiento el calor especifico fue el esperado (entre 5 y 8).

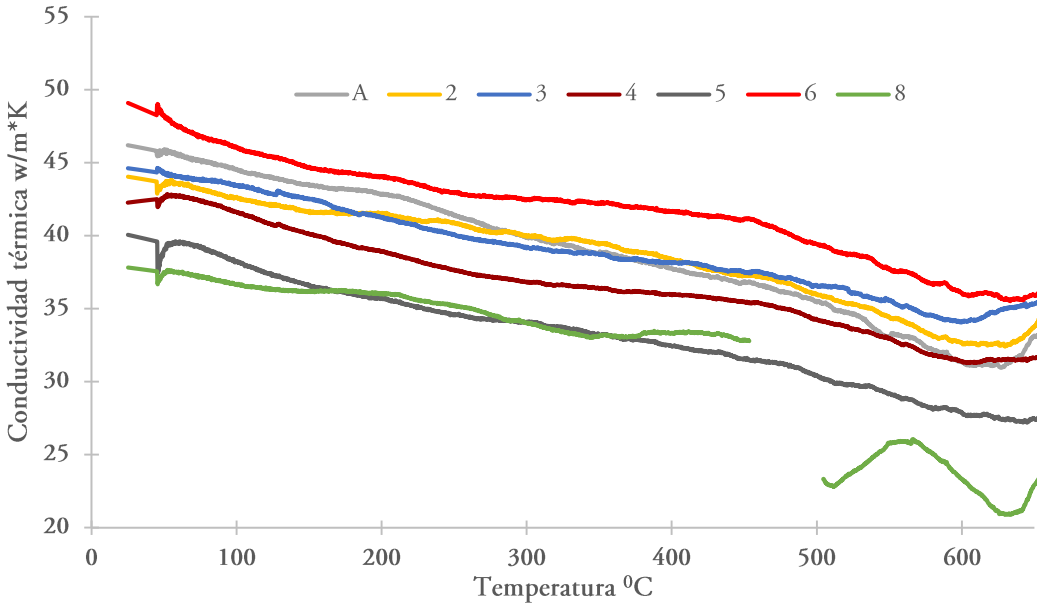

Resultado de la conductividad térmica.

Conclusiones

Así tras este proyecto, se pudo responder a todas las preguntas de investigación al principio formuladas y se concluyó que:

- El molibdeno tiene una notable influencia sobre la carga de rotura. Comportándose como un elemento que refina la perlita y los tamaños de grano incrementando así la carga de rotura. El molibdeno se mostró como como un elemento que promueve los carburos lo cual no mejora en absoluto la carga de rotura, pero este efecto se ve contrarrestado por la aparición de ausferrita.

- En la conductividad no se alcanzaron conclusiones demasiado claras, pero es posible ver que cuando se tiene una matriz de ausferrita la conductividad es claramente menor que cuando se tiene una matriz perlítica.

- El grafito no se ve influenciado por el contenido en molibdeno, ya que la fracción de grafito y el tipo de grafito no muestran ninguna tendencia con el contenido en molibdeno.

- El molibdeno tiene una clara influencia sobre la microestructura. Primero modificando la matriz perlítica: refinando las láminas de perlita, disminuyendo el tamaño de grano y fomentando los carburos y la ausferrita. Y transformando la matriz perlítica a ausferrítica en altos contenidos de molibdeno.

- El molibdeno tiene modifica la transformación de estado sólido de tal manera que a medida que el molibdeno aumenta, el cambio volumétrico y el calor latente correspondiente a dicha transformación disminuyen. En otras

palabras, molibdeno desplaza la aparición de perlita a medida que este aumenta.

Contents

1 Introduction 23
1.1 BACKGROUND 23
1.2 PURPOSE AND RESEARCH QUESTIONS 23
1.3 DELIMITATIONS 24
1.4 OUTLINE 24
2 Theoretical background 25
2.1 CRYSTALLOGRAPHIC LATTICES 25
2.1.1 Bravais lattices 26
2.2 ALLOTROPES FORMS OF PURE IRON 27
2.3 IRON-CARBON DIAGRAM 28
2.4 IRON CARBON PHASES AND MICROSTRUCTURES 29
2.5 CAST IRON 30
2.5.1 Classifications 30
2.5.2 Lamellar graphite cast iron 32
2.5.3 Solidification of lamellar cast Iron 33
2.6 TTT DIAGRAMS 34
2.7 MOLYBDENUM IN CAST IRON 35
2.8 TENSILE TEST 36
3 Method and implementation 38
3.1 MATERIALS 38
3.1.1 Sample preparation 38
3.2 THERMAL TEST 39
3.2.1 Dilatometer 39
3.2.2 Differential Scanning Calorimetry (DSC) 41
3.2.3 Laser flash 43
3.2.4 Thermal conductivity 44

3.3 TENSILE TEST 45
3.4 MICROSTRUCTURE 46
4 Findings and analysis 49
4.1 DILATOMETER 49
4.2 DIFFERENTIAL SCANNING CALORIMETRY 51
4.3 LASER FLASH 53
4.4 THERMAL CONDUCTIVITY 54
4.5 TENSILE TEST 54
4.6 GRAPHITE 56
4.7 MATRIX 57
5 Discussion and conclusions 58
5.1 DISCUSSION OF METHOD 58
5.1.1 Material 58
5.1.2 Thermal tests 58
5.1.3 Tensile test 59
5.2 DISCUSSION OF FINDINGS 59
5.2.1 Tensile test 59
5.2.2 Dilatometer 62
5.2.3 Differential Scanning Calorimetry 63
5.2.4 Laser flash 64
5.2.5 Thermal conductivity 64
6 Conclusions 65
7 Future work 66
8 References 67
9 Appendices 70
9.1 CHEMICAL COMPOSITION OF EACH CASTING 71
9.2 CURVES OF THE DILATOMETER 72
9.3 DIFFUSIVITY 76
9.4 TENSILE TEST 77

9.5 MATRIX MICROGRAPHS 79

9.6 FRACTURE MICROGRAPHS 83

Figures

Figure 1. Unit cell representation. 25

Figure 2. Bravais lattices.[3] 26

Figure 3. Allotropes of pure iron upon heating and cooling [5]. 27

Figure 4. The metastable and stable Fe-C phase diagram shown as solid and dashed lines respectively [7]. 28

Figure 5. The inverse lever rule [10]. 29

Figure 6. Examples of the three graphite morphologies, (a) LGI, (b) SIG, (c) CGI [14]. 31

Figure 7. Schematic representation of graphite crystal structure [15]. 31

Figure 8.The different types of graphite flakes [13]. 32

Figure 9. Representation of the grains and the dendrites formed [17] on the left and schematic representation of the different zones in a mold on the right[16]. 33

Figure 10. Solidification curve and its respective structure at different temperatures [19]. 34

Figure 11. Representation of a TTT diagram and its Jominy specimen [11]. 35

Figure 12. Schematic illustration of the pearlite's shift produced by the molybdenum [24]. 36

Figure 13. Example of tensile test curve. 37

Figure 14. Tangent modulus of the FGI, CGI and SIG [30]. 37

Figure 15. Schematic display of the different samples in the cone. 39

Figure 16. In the left the Netzsch Dilatometer 402C used, and in the right a schematic placement[31]. 40

Figure 17. Dilatometer results, where the red line sows the behavior during the heating and the blue one during the cooling process. 41

Figure 18. Figure 19. Netzsch DSC 404 C Pegasus on the left and schematic picture of the crucibles on the right [32]. 41

Figure 20. Example of the DSC results. 42

Figure 21. On the left the apparatus used, and on the right a schematic representation [33]. 43

Figure 22. Laser flash results. 44

Figure 23. Thermal conductivity. 45

Figure 24. Tensile test graph. 46

Figure 25. Tensile test bar, where the three on right are the ones used and in the left we can see where the samples were. 46

Figure 26. Example of one fracture's micrograph. 47

Figure 27. Example of one micrograph that was used in the Stream motion. 47

Figure 28. Examples of the microstructure after the etching, left pearlitic matrix and right ausferrite matrix. 48

Figure 29. Thermal expansion as function of the Mo percentage. The red points corresponds with the two values of the composition 8 in the first lineal section. 50

Figure 30. Volumetric changes during the heating in red and in blue during the cooling. 50

Figure 31. Specific heat during heating, A) is the full graph and B) correspond with the data used for the conductivity including the interpolation of composition 4. Please note that figures have different scales. 51

Figure 32. Specific heat during the cooling. 52

Figure 33. Graphs integrated in the integration interval. 52

Figure 34. Values of the integration as function of Mo. 53

Figure 35. Results of thermal diffusivity. 53

Figure 36. Results of thermal conductivity. 54

Figure 37. Effect of Molybdenum on UTS. 55

Figure 38. Effect of Molybdenum on E_{mod}. 55

Figure 39. Effect of Molybdenum on dL at F_{max}. 56

Figure 40. Effect of Mo in the graphite shape. 56

Figure 41. Effect of Mo in the graphite fraction. 56

Figure 42. Graphite type of each composition. 57

Figure 43. Example of how was appearing the asuferrite. Composition 2, 6 and 8 respectively. 57

Figure 44. Matrix A, 2 and 3 with 2.5 magnification. 60
Figure 45. Matrix of composition 3 and 4. 60
Figure 46. Matrix 3 and 4, showing the carbides. 61
Figure 47. Matrix of compositions 5 and 6 61
Figure 48. Example of one micrograph from composition 8 62
Figure 49. Deformed lattice of austenite. 63
Figure 50. Dilatometer curve of composition A. 72
Figure 51. Dilatometer curve of composition 2. 72
Figure 52. Dilatometer curve of composition 4. 73
Figure 53. Dilatometer curve of composition 3. 73
Figure 54. Dilatometer curve of composition 5. 74
Figure 55. Dilatometer curve of composition 6. 74
Figure 56. Dilatometer curve of composition 8. 75
Figure 57. Micrographs from the matrix of composition A. 79
Figure 58. Micrographs from the matrix of composition 2. 80
Figure 59. Micrographs from the matrix of composition 3. 80
Figure 60. Micrographs from the matrix of composition 4. 81
Figure 61. Micrographs from the matrix of composition 5. 81
Figure 62. Micrographs from the matrix of composition 6. 82
Figure 63. Micrographs from the matrix of composition 8. 82
Figure 64. Fracture of the composition A. 83
Figure 65. Fracture of composition 2. 83
Figure 66. Fracture of composition 3. 84
Figure 67. Fracture of composition 4. 84
Figure 68. Fracture of composition 5. 84
Figure 69. Fracture of composition 6. 85
Figure 70. Figure of comosition 8. 85

Tables

Table 1. The seven crystals systems. 26

Table 2. Main components of each casting. 38

Table 3. Thermal expansion values. 49

Table 4. Composition of the studied samples 71

Table 5. Diffusivity data. 76

Table 6. Results of the UTS. 77

Table 7. Results of the E modulus. 77

Table 8. Results of the elongation. 78

1 Introduction

This thesis focuses on the effect of lamellar cast iron alloyed with different levels of Molybdenum. The mechanical and the thermal properties are studied in order to find out any relation with the molybdenum content and correlate with the microstructural parameters.

This thesis was a final project work for bachelor level issued on behalf of the Department of material and manufacturing at Jönköping University. Which is the culmination of my four years bachelor in Industrial Engineering conducted at University of Oviedo, Spain.

1.1 Background

Cast iron is the most extended material all over the world, mainly in the automotive industry where day after day have to tolerate higher pressures and temperatures to make engines even more efficient. In order to improve the great properties of the lamellar cast iron is essential to control the solidification and the solid state reactions. Since properties of the lamellar cast iron are extremely linked to both mechanism.

The common project "Cast design" wherein the Department of Materials and Manufacturing of Jönköping University, Swerea Swecast, Volvo and Scania, are involved, has the goal to achieve a better understanding of the cast Iron to produce a good quality castings. The research tries to understand the role of different alloying elements used in the cast iron to improve the properties such as the thermal shock and the fatigue resistance.

1.2 Purpose and research questions

In a previous stage of the project, lamellar cast iron alloyed with Molybdenum has been studied with respect to the solidification and microstructure. Concretely the thesis of Björn Domeij and Huiying Wang study the influence of Molybdenum on Isothermal Coarsening and on the solid state transformation of Austenite in LGI respectively, with which it was achieved a complete characterization of the microstructural features. This thesis intends to characterize mechanical and thermal properties of seven different alloys in order to correlate both microstructural parameters and final properties.

The main questions this work seeks to answer are:

a. **What influence does the molybdenum have on mechanical properties?**
b. **What influence does the molybdenum have on thermal properties?**
c. **Does molybdenum have any influence on the graphite?**
d. **Does molybdenum have any influence on the microstructure?**
e. **How does molybdenum influence on the solid state transformation?**

1.3 Delimitations

This thesis focus in the study on the effect of molybdenum in a hypoeutectic lamellar grey cast iron. The study was carry out exactly with a LGI of 3,9 equivalent carbon and alloyed with seven different molybdenum contents. The different alloys are between 0,05 and 0,96% of molybdenum content and the others components, were fixed in all the alloys.

1.4 Outline

The thesis begins with a theoretical overview of cast iron, where topics such as type of structure, diagrams, phases, solidification and molybdenum are covered. Then the methodology followed during the experiments, the different experiments done, how it was conducted and the results taken is explained. Afterward, the results are exposed objectively and finally in the last section the results are discussed.

2 Theoretical background

Cast iron is a term used for identify a large family of ferrous alloys, with a carbon content higher than 2% and remarkable silicon, common values are between 1% to 3%. Cast iron contain also addition alloying elements but in lower amount such as Mn, P, S, Cr and many others [1]

Primitive people used iron-nickel meteorites until learning how extract iron from iron ore. However, the metallurgy on an industrial scale it wasn't possible without the discovered of the hematite and the quenching to hardening the metal in 1200-1000 B.C. in Armenia's mountains. This development gave rise to the Iron age the steel became essential, from now on. The first iron casting known is a lion made in China in 502 B.C. but the introduction of the cast iron in Europe was about 1200 to 1450 A.D. By that time Chine have already pioneered the structural use of cast iron.

Nowadays cast iron is the material more common in the engineering and building world. Around 70% of the casting, production in the world is Cast iron. This prevalence in the market is mainly due to the great range of the physical and mechanical properties and its competitive price [2]

2.1 Crystallographic lattices

Due to all the metal and alloys has a crystallography lattice it's crucial to know the types and the characteristics of then. In the idealized theory, a crystal is made of infinite parallelepipeds, these parallelepipeds are known as unit cell.

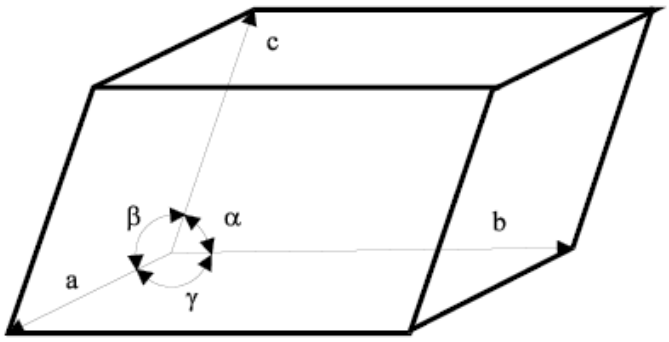

Figure 1. Unit cell representation.

If we look at a generic unit cell, **Figure 1**, we can see some essential parameter to define the cell, as the lengths of the edges (a, b, c) and the angles between them (α, β, γ). According to the shape and symmetry defined by the parameter described above we can classify the crystals into seven different systems as the **Table 1** shows [3].

Table 1. The seven crystals systems.

System	Unit-cell dimensions	Unit-cell angles (°)	Characteristic symmetry
Triclinic	$a \neq b \neq c$	$\alpha \neq \beta \neq \gamma \neq 90$	Only inversion center possible
Monoclinic	$a \neq b \neq c$	$\alpha = \gamma = 90, \beta \neq 90$	Single twofold axis or/and mirror
Orthorhombic	$a \neq b \neq c$	$\alpha = \beta = \gamma = 90$	Three perpendicular twofold axes or/and mirrors
Tetragonal	$a = b \neq c$	$\alpha = \beta = \gamma = 90$	One fourfold axis
Trigonal	$a = b \neq c$	$\alpha = \beta = 90, \gamma = 120$	One threefold axis
	$a = b = c$	$\alpha = \beta = \gamma \neq 90$	
Hexagonal	$a = b \neq c$	$\alpha = \beta = 90, \gamma = 120$	One sixfold axis
Cubic	$a = b = c$	$\alpha = \beta = \gamma = 90$	Four threefold axes

2.1.1 Bravais lattices

In 1850, Bravais discovered more possibilities of unit cells, in all there are fourteen types of unit cell, called Bravais lattices. These lattices were more complex due to the lattice points. In the seven crystal systems or primitive (P) the lattice points are on the cell corners only but Bravais lattices has lattices points in the center of all the faces (F), in the center of the bases (B) and within the cell (I). The fourteen lattices are showed in the **Figure 2**.

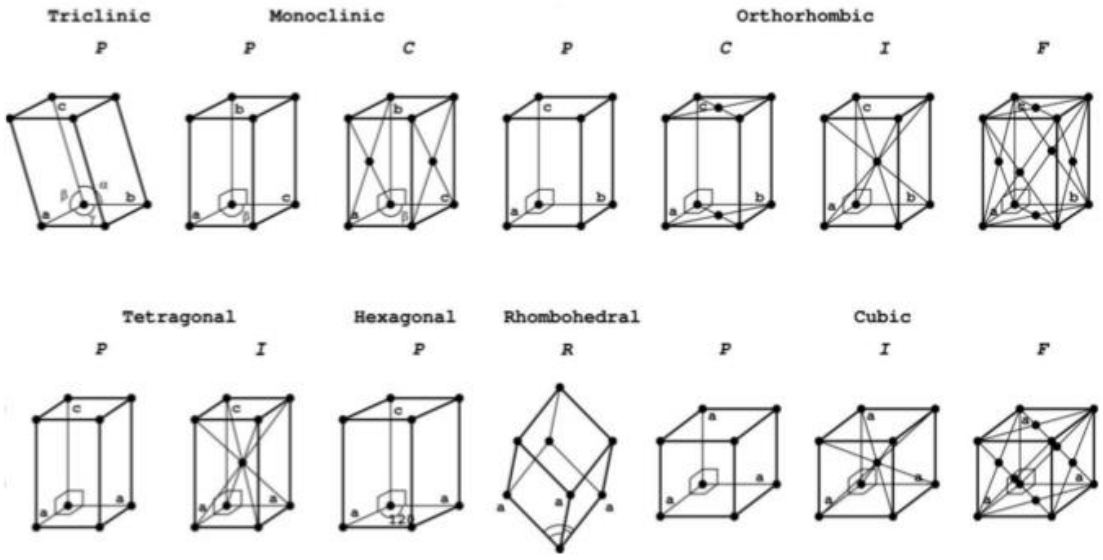

Figure 2. Bravais lattices.[3]

Fortunately, most of the metals crystallize in easy lattice. The metals crystalize basically in three different types, the FCC, BCC and HCP. The HCP is hexagonal Bravais lattices but with one more lattice point in the position $\left(\frac{2}{3}a, \frac{1}{3}b, \frac{1}{2}c\right)$.

It will be useful as well to define the atomic packing factor (APF) to understand later on, the changes in the density of the materials when it changes the crystal structure. The APF of a crystal lattice is the fraction of the space used for the atoms in one cell. Moreover, if we suppose atoms like perfect spheres we can calculate easily. The APF for the FCC, BCC, and HCP structures are 0,74 0,68 and 0,74 respectively [4].

2.2 Allotropes forms of pure iron

Despite that pure iron does not have any industrial application owing to it is the principal component in the cast iron it is important to mention it. When we proceed to cooling an iron sample melted it previously, the first change it is a phase transition, liquid turns into a solid. After the solidification, some changes in the crystal structure are followed. This crystal structure changes in a solid are called allotropes. The allotropes forms of the iron are showed in the **Figure 3**.

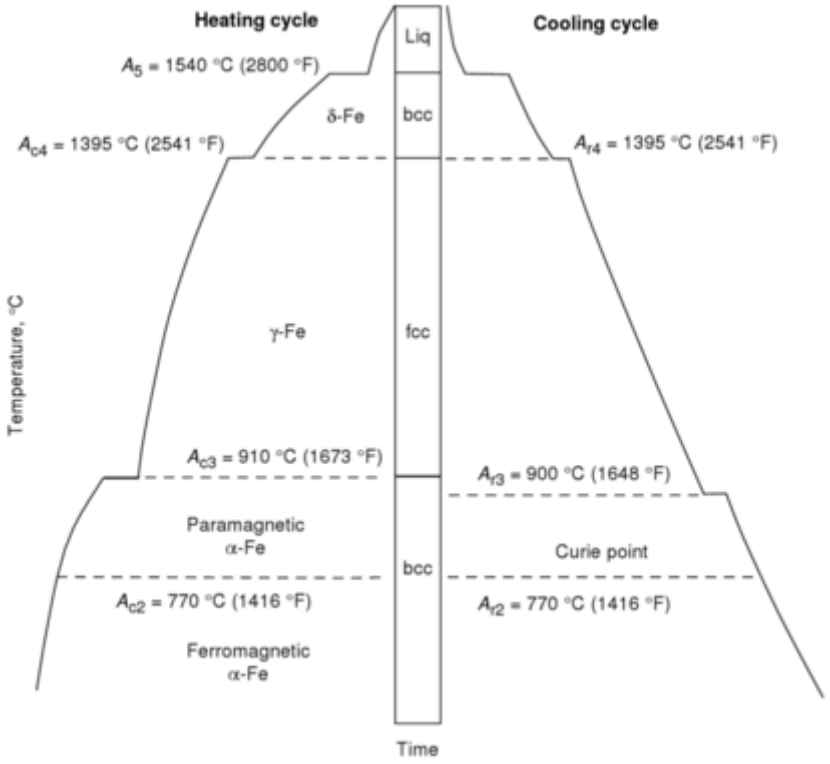

Figure 3. Allotropes of pure iron upon heating and cooling [5].

As we can see in the figure above, the temperature at which the allotropic transformation occurs are not equal for heating and cooling, this is because crystalline system resists its own transformation. That is known as thermal hysteresis and it is as bigger as faster is the cooling or the heating.

If we take as reference the cooling graph, at 1540 ^{0}C the iron solidify into a body centered cubic lattices (BCC), known as iron δ. This structure is stable until 1395 ^{0}C, temperature which, the iron transform itself into iron γ that presents a face centered cubic (FCC) structure. Finally at 900 ^{0}C, the iron γ becomes into iron α, and it's again a centered cubic lattices (BCC), the iron α is stable at room temperature. At 770 ^{0}C we can see another transformation but in this case, it is not a lattice structure transformation, it is just that the iron becomes ferromagnetic which so far, in all other structures it was not, it was non-magnetic. This temperature which the iron becomes ferromagnetic is called Curie temperature.

The allotropic transformation can result in an abrupt volumetric variation, for example in the transformation Iron γ into Iron α, the relation ΔV/V is around the order of 0,8% which is quite big [6].

2.3 Iron-Carbon diagram

Even though the steels and cast irons are alloys with a considerable amount of components, it can be considerate like a binary due to the lower proportion of the others components. The **Figure 4** shows the diagram Fe-C that has industrial interest. The diagram delimits the different phases along the temperature and the carbon concentration at atmospheric pressure.

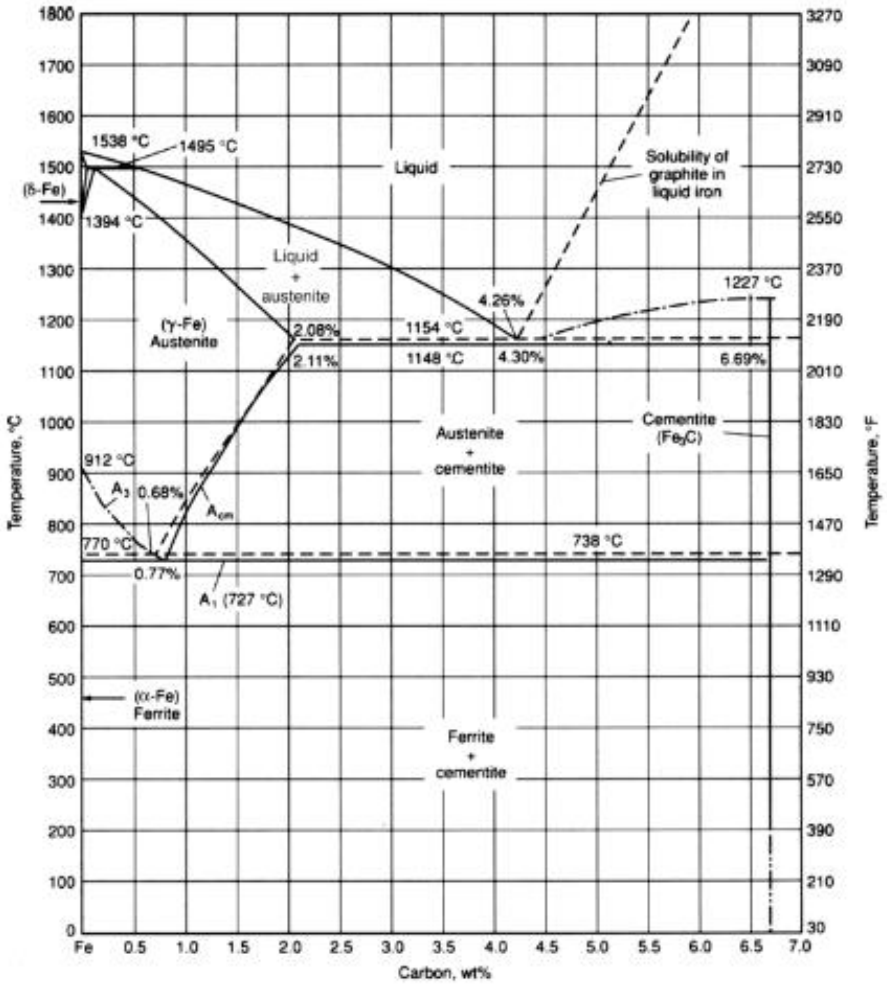

Figure 4. The metastable and stable Fe-C phase diagram shown as solid and dashed lines respectively [7].

As it was said before, although it is considered binary system it is not and there are some particular alloying elements with the ability of reduce the maximum solubility of carbon in austenite and reduce the carbon content for the eutectic point. This components are essentially the Silicon and Phosphorous. Since this components modify the phase diagram it should be taken into account, so for the use of the

binary diagram it is necessary calculate the carbon equivalent (CE). The CE could be calculated with the equation among other [8].

$$CE(\%) = \%C + \frac{1}{3}(\%Si + \%P)$$ [9] (equation1)

The diagram can be used to determine the percentage of the phases in equilibrium. This can be done when the composition and the temperature are located within a two-phase field and it would be done with the lever rule or rather the inverse lever rule. The inverse lever rule is a mathematical expression based in the principle of conservation of matter. The formula is in the following picture, **Figure 5**, where the variables are represented there as well. The W_s is the fraction of solid at the temperature T and the W_l is the fraction of liquid at the same temperature [5].

$$W_s = \frac{W_o - W_l}{W_s - W_l}$$

$$W_l = \frac{W_s - W_o}{W_s - W_l}$$

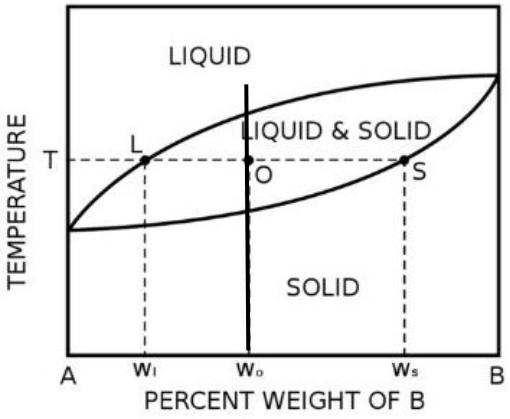

Figure 5. The inverse lever rule [10].

2.4 Iron Carbon phases and microstructures

As was shown before in the diagrams, the constituents of the steels and the cast irons are: austenite (γ), ferrite (α), graphite (Gr), cementite (Fe_3C), perlite, bainite, martensite, ledeburite and ausferrite.

Austenite: it is a face-centered cubic crystalline lattice of Carbon and γ iron. The maximum solubility of carbon it is 2,1% at 1145 ºC, and as the temperature decreases the solubility of carbon also. The austenite is non-magnetic and does not usually exits at room temperature.

Ferrite: It is a body-centered cubic crystalline lattice of carbon and α iron. The interstitial places are very small in this case. Therefore, the amount of carbon in the structure is quite small. The maximum solubility of carbon in the ferrite is 0,02% at 727 ºC and as the temperature decreases the solubility of carbon as well.

Cementite: it is an intermetallic compound and Fe_3C stoichiometrically, that correspond with 6,67% of carbon content. It crystallizes into an orthorhombic structure, which is hard and fragile typically of white cast iron. With the enough time, it decomposes into graphite.

Graphite: is the most stable carbon phase consisting of atom-thick sheets of graphene bond. It usually grows under the eutectic temperature but can appear in the melt as well

Martensite: it is a very hard material formed from the austenite, due to the ferrite formation is not performed. Either for a very fast cooling and the carbon atoms do not have enough time to diffuse out of the crystal or because the high allowing components like Mg, Ni, Cu or Mo. It possess a BCC lattice but with a deformation in the crystal structure owing to the accommodation of the carbon therefore becomes into a body centred tetragonal.

Pearlite: this lamellar constituent, is formed when the carbon content is greater than 0,025 on the Fe-C binary phase diagram, by cooling under the eutectic temperature. This process follow the reaction: Austenite ↔Pearlite (cementite + ferrite) and it has good mechanical properties. When a pearlite matrix is achieved, the mechanical properties are better as finer are the interlamellar spacing.

Bainite: is a constituent formed by ferrite and cementite like the perlite but the difference lies in the ferrite, the ferrite in the bainite has an acicular morphology and the carbides are discrete particles. Due to that, the properties between bainite and perlite are quite different.

Ledeburite: is a coarseeutectic mixture of austenite and cementite which contains 4,3% C and is formed bellow 1146 ^{0}C.

Ausferrite: this constituent consists in bainitic ferrite, embedded within austenite grains. It is produced with a heat treatment or by controlling the alloying additions such as Mo, Mn, Si and Cu. [6, 11, 12]

2.5 Cast Iron

The term cast iron identify a huge family of ferrous alloys, which have three principal components, Iron, Carbon and Silicon. This ferrous family is comprised between 2,1 and 4,5% of CE and it is possible classify it in different ways.

2.5.1 Classifications

The different criteria that can be used for the classification are: by the fracture aspect, it could be Grey or white, by the graphite shape such as spherical, compacted and lamellar, by the microstructure of the matrix, it can be ferritic, pearlitic, austenitic, etc. and by the commercial designation as malleable, ductile etc. In this project is studied the lamellar graphite cast iron which is within the graphite shape classification. [13].

So depending on the form of the graphite are distinguished three different graphite morphologies:

- Spherical graphite iron or SGI where the graphite solidify as nodules. The graphite nodules make it much flexible and elastic than other types of cast iron; it is because of this, that it is also known as ductile cast iron. This cast stands out for the excellent mechanical properties but it is not as good in thermal properties.
- Compacted graphite iron or CGI where the graphite solidify in an intermediate shape between the SGI and LGI. The properties are between both, better thermal properties than SGI but worse than LGI and better mechanical properties than LGI but worse than SGI.
- Lamellar graphite iron or LGI in which the graphite solidify with a flake-like shape. Highlight of this cast is the thermal properties, with very good conductivity and specific heat capacity and with a very good damping capacity as well.

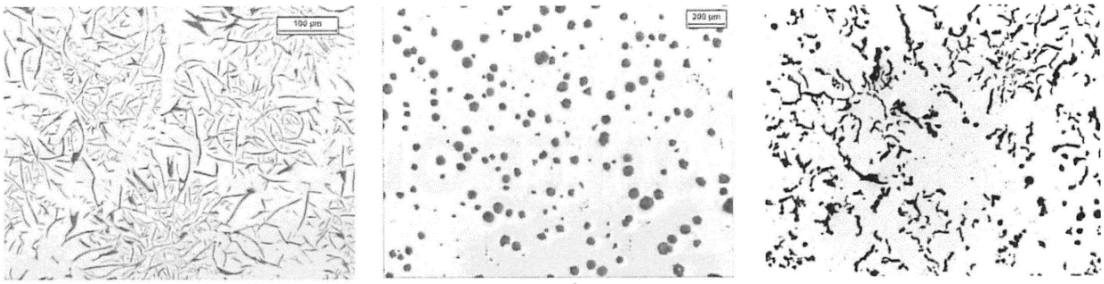

Figure 6. Examples of the three graphite morphologies, (a) LGI, (b) SIG, (c) CGI [14].

The different shapes of the graphite is the result of the growth direction, which the graphite crystal prefers. The graphite has a hexagonal structure and it can grow in the C-axis or in a-axis as we can see in **Figure 7**. If it grows in c-axis the result it would be spherical graphite iron otherwise, in the a-axis it would be lamellar graphite iron.

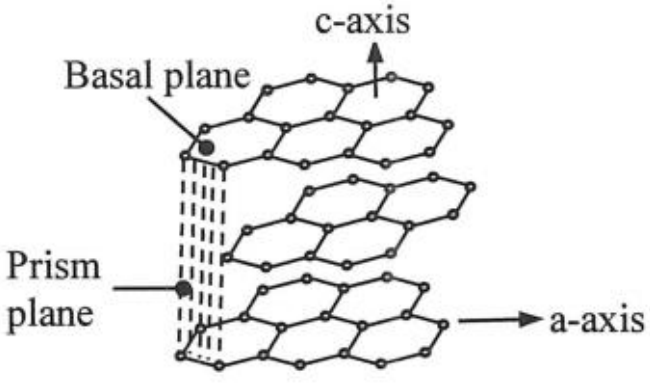

Figure 7. Schematic representation of graphite crystal structure [15].

2.5.2 Lamellar graphite cast iron

The normal structure of the lamellar graphite cast iron is a matrix of pearlite with graphite flakes dispersed, the amount, size and distribution that the flakes take in the structure will govern the properties of the LGI. One method of assess these different ways, that the graphite takes, is given in ASTM A 247. Where there are five graphite-flakes distributions, A to E. The **Figure 8** shows the five graphite-flakes.

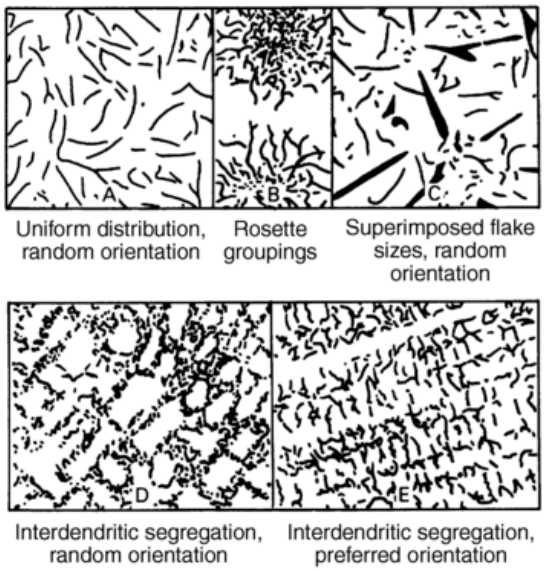

Figure 8.The different types of graphite flakes [13].

Type A graphite is the best structure if the mechanical properties should be optimized. It has a random orientation of graphite flakes and the distribution is uniform throughout the iron matrix. This structure is achieved when the iron solidify with a minimum undercooling.

Type B graphite has a rosette pattern flakes, and it is formed in irons near the eutectic point and with a big undercooling. It is common in pieces with a thin section, around 10 mm, and by the surface of thicker sections.

Type C graphite or also known as Kish graphite is typically from hypereutectic irons with high carbon content. This type of graphite reduce considerably the mechanical properties and after machined the surface is quite rough. Nevertheless, this type of graphite has some interest in the industry, because of its good thermal properties, which make perfect for applications where heat transfer is needed.

Type D and E graphite are founded in interdendritic regions when the undercooling is not enough to cause carbide formation. The D type has a random orientation while the E Type has a preferred orientation in the flakes

Another factor to consider is the graphite-flakes size, the large flakes provide high thermal conductivity and damping capacity, in the other hand short flakes provides good mechanical properties and are desirable when good tensile properties and a smooth surface finish are required.

2.5.3 Solidification of lamellar cast Iron

According on composition cast iron can solidify as Hypoeutectic, eutectic or hypereutectic, it depends on the carbon equivalent factor explained before, where the eutectic point is on 4.3%C. The lamellar graphite iron is usually produced as hypoeutectic, as occurs in our case, that's means with a less carbon equivalent factor than 4.3% [9].

The solidification starts with nucleation and growth of austenite with a maximum solubility of carbon of 2%, once the nuclei surpass the critical radius[1] it follows the growth, usually under the conventional conditions, the austenite grows in dendrites. All the dendrites formed from one nuclei is known as grain and has a uniform crystallographic orientation. The grains are different according with the places in the mold. The nuclei formed on the mold wall, are the first ones appear, this part is known as chill zone or outer equiaxed zone. This zone is followed by the columnar zone where the grains grow perpendicular to the mold wall. Finally there will be some grains formed in the remaining liquid, they are equiaxed grains which have a spherical shape due to the low thermal gradient in the center of the mold [16].

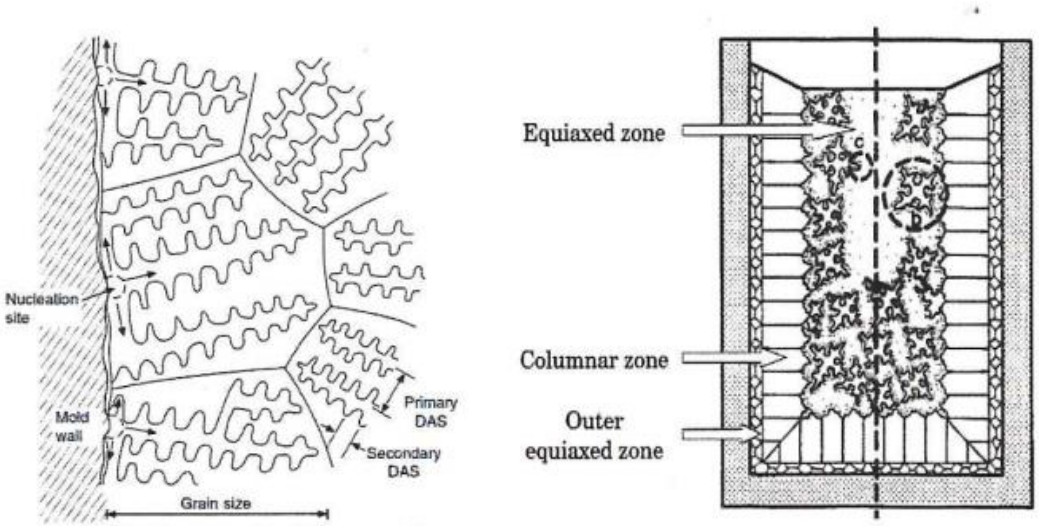

Figure 9. Representation of the grains and the dendrites formed [17] on the left and schematic representation of the different zones in a mold on the right[16].

[1] Critical radius is the minimum radio of a nuclei that must have, to be stable and begin the growth.

At the end of the solidification, after the eutectic temperature the dissolved carbon starts to precipitates as graphite until the eutectoid temperature (723 ^{0}C). However, this step is not as simple because due to a very high undercooling and in non-equilibrium conditions the graphite is not formed, but is formed cementite instead. Moreover, cementite is not a desired component by the fact that is very fragile. In the **Figure 10** is shown the sequence of the lamellar graphite solidification. [18].

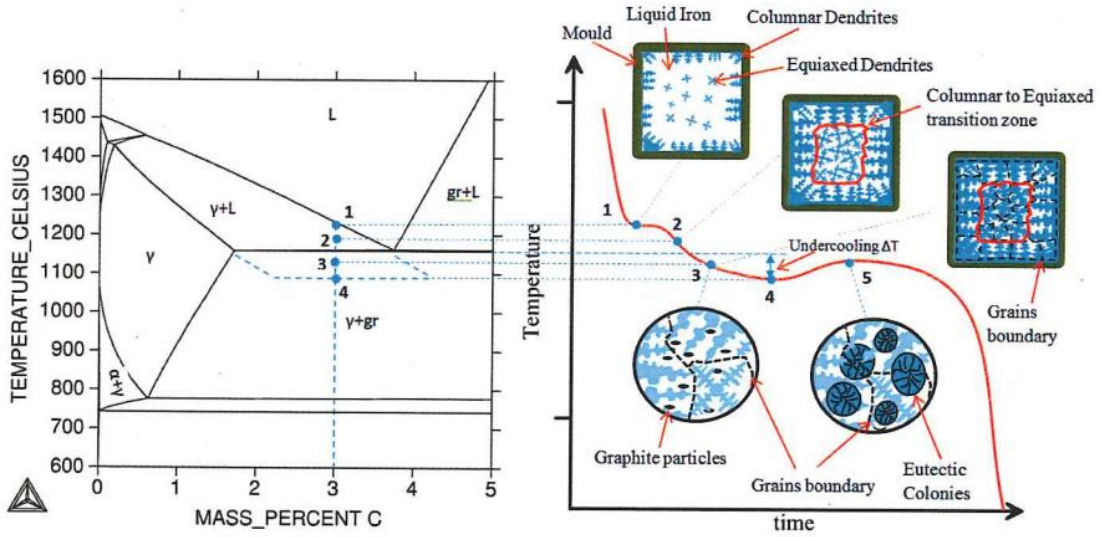

Figure 10. Solidification curve and its respective structure at different temperatures [19].

During the eutectoid reaction, the austenite will be transformed into pearlite or ferrite, or a mixture of both, ferrite and pearlite. This transformation is controlled by the cooling conditions and by adding alloying elements. So if the result is ferrite that means the transformation occurred according to the equilibrium phase diagram otherwise if the result is pearlite the transformation occurred by the metastable phase diagram [20, 21].

2.6 TTT diagrams

A Time-Temperature-Transformation diagram has curves that define the regions where a phase transformation takes place, from either isothermal or athermal conditions. The isothermal transformations, IT diagrams represent the limits of when an isothermal transformation starts, stops, or when a volume transformation or property value occurs. The other kind of diagram is the Continuous Cooling Transformation or CCT, which represent the transformation according to the temperature and to the cooling or heating rate curves.

In the figure 6 it is shown the relation between the CCT and IT diagrams in a steel. The different cooling rates are given by a Jominy end-quench specimen[22].

The Jominy end-quench test, takes the measure of the hardenability, which refers to the ability of a material to be hardened in a particular depth. If you look at the **Figure 11**, you can see the hardness according to the distance from the quenched

in the Jominy representation, if the sample had had a perfect hardenability the plot it would have been horizontal.

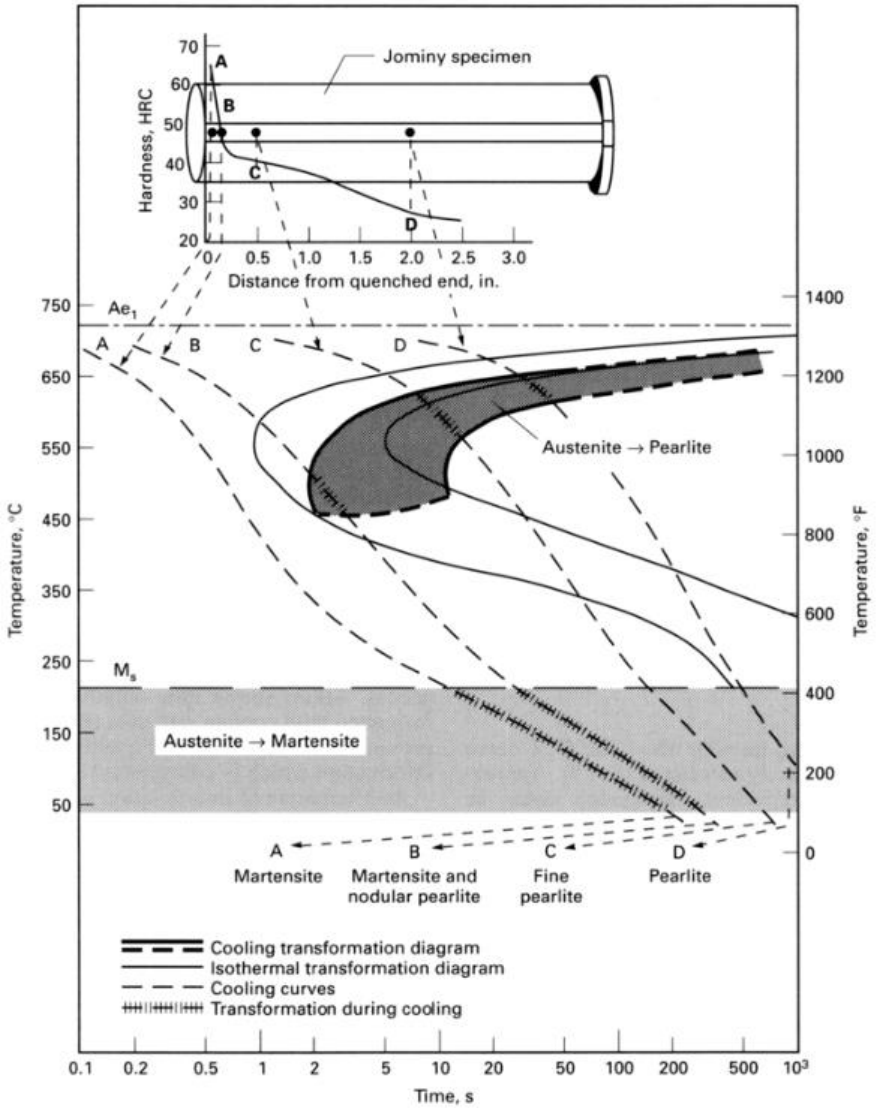

Figure 11. Representation of a TTT diagram and its Jominy specimen [11].

2.7 Molybdenum in cast Iron

The molybdenum is a transition metal with a silver-white appearance, which has 42 protons and 95,94 of atomic weight. It is extremely hard and with a very high melting point (2623 ^{0}C). The molybdenum solidify in a BCC lattice and it usually used in steel and cast iron as an alloy [23].

Molybdenum in cast iron is known as ferrite stabilizer, pearlite refiner and for promoting the bainite and the ausferrite microstructures. Thereby with a certain amount of Mo it is possible to produce a fully ausferritic microstructure, therefore

the austenpering [2] stage can be eliminated but similar properties are achieved But an excess of Mo is synergy with Mn, Ni and Cu generates carbides at eutectic cell boundaries which negative effects in the mechanical properties [12].

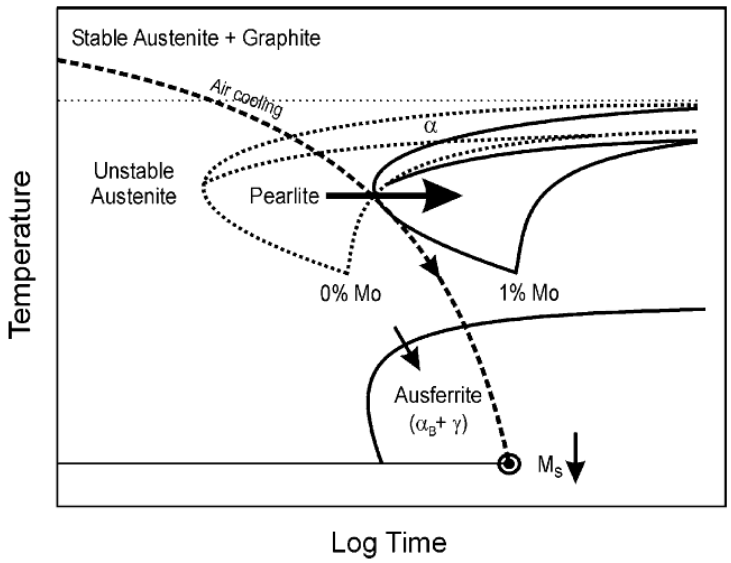

Figure 12. Schematic illustration of the pearlite's shift produced by the molybdenum [24].

Owing to this change in the structure, the thermal properties are affected as well, some studies relate the Mo with a lower thermal conductivity in CGI. Where affects more at lower temperatures than at high.

In addition, Molybdenum adds strength and hardness and helps cast iron tolerate the high pressures and temperatures but an excess of it will generate carbides and large porosities [25-28].

2.8 Tensile test

Basic issues of tensile test it should be explained, due to complicate behavior of lamellar cast iron under this kind of tests. In the **Figure 13** it is possible to see typical data of a tensile test.

[2] Austempering is the process in which the mechanical properties are significantly improved by changing the matrix of ferritic/perlitic to ausferrite. It takes places with a complex heat treatment.

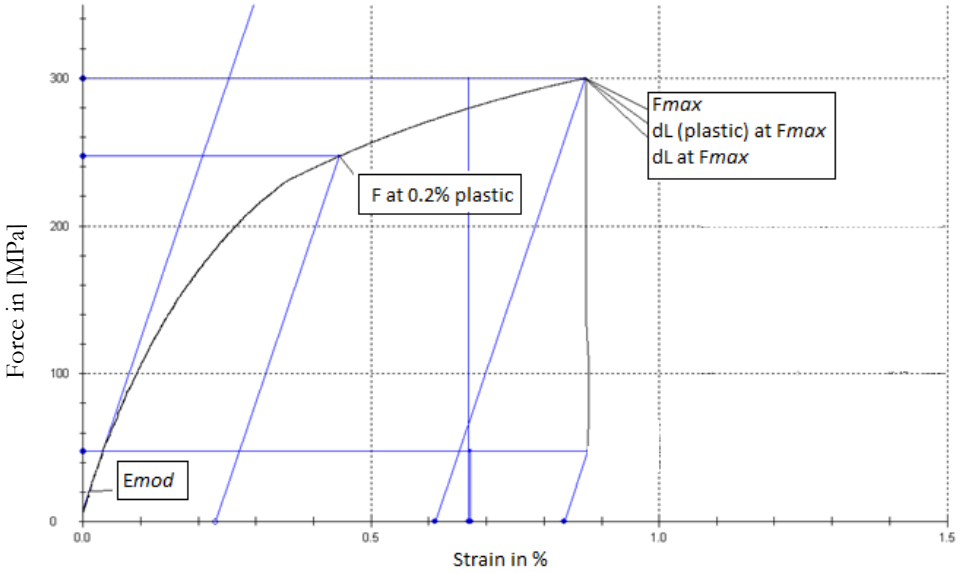

Figure 13. Example of tensile test curve.

The elastic modulus that is possible to see as E_{mod} in the figure is defined as the slope of its stress–strain curve in the elastic deformation region Askeland [29]. However some studies like [30], shows that the flake graphite cast iron doesn't have an elastic zone, and neither a constant tangent on the stress-strain curve. The tangent modulus of the flake graphite cast iron, compacted graphite iron and nodular graphite iron is shown in the **Figure 14** and it is possible see that the CGI and SGI have a constant tangent but the LGI not. Therefore, if it has not an elastic zone and neither a constant region calculate it could be a topic for another thesis, because it does not meet its own definition of E_{mod}.

So due to the non-linear behavior of the lamellar cast iron under mechanical loads the most important parameter for characterizing its mechanical properties is the ultimate tensile strength UTS.

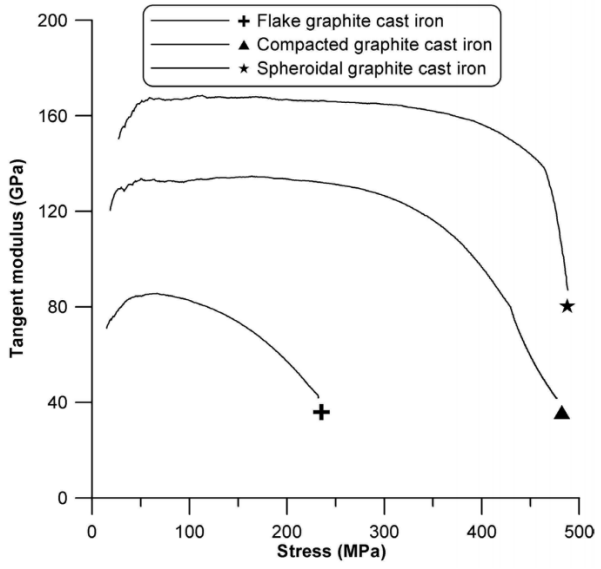

Figure 14. Tangent modulus of the FGI, CGI and SIG [30].

3 Method and implementation

In this section, the methodology that the thesis followed it is explained. In order to explained in a clear way the section was divided material, thermal test, tensile test and microstructure analysis.

3.1 Materials

It was studied a hypoeutectic lamellar grey iron with seven different contents of Mo since 0,05% until 0,96% as it's shown in the table .The material was provided for a research project "Cast design" which the collaborators are Jönköping University, Swerea SWECAST, Scania CV AB and Volvo Group Trucks Operations. The complete chemical analysis table is attached in the appendix 9.1 but the **Table 2** shows the main components of each composition.

Table 2. Main components of each casting.

Material ID	Chemical composition						
	C	**Si**	**Mn**	**Cr**	**Mo**	**Cu**	**CE**
A	3,40	1,89	0,57	0,15	**0,05**	0,90	3,90
2	3,26	1,89	0,60	0,14	**0,16**	0,82	3,91
3	3,24	1,89	0,60	0,13	**0,37**	0,78	3,89
4	3,28	1,9	0,56	0,13	**0,48**	0,76	3,93
5	3,25	1,88	0,56	0,13	**0,65**	0,80	3,89
6	3,26	1,89	0,58	0,13	**0,81**	0,81	3,91
8	3,24	1,86	0,61	0,13	**0,96**	0,93	3,87

3.1.1 Sample preparation

Originally, the material was a cone that, although not all the cones had the same dimension an approximate dimension could be 150mm height and diameters of 50 and 60mm. To take the samples for the thermal and tensile test, several process of machined were required. First of all the material was selected carefully in the warehouse according with the surface quality (without blowholes or some other defects naked eye). Then the cones were cut in quarters. Three of them were cut in quadrangular prisms in order to straight turning in the lathe easily.

For the tensile test, two prisms were taken of each cone and always opposites, to get more reliable data. After machined in a conventional lathe (600 lathes M390), it was obtained a cylinder of 12mm diameter. Then the final shape was given with a

CNC lathe (HAAS CNC ST 10). The sample's dimension was according to the Volvo standard 5C25.

The thermal samples preparation involve diverse machines and operation, such as lathe, grinding, low speed saw, etc. With a final goal of obtaining three different samples for each thermal test, i.e. DSC, Laser Flash and dilatometer. The shape of these samples are cylinders with Ø 4mm and 42,1mg, Ø 12.5mm and 4.375 height and Ø 6mm and 12mm height respectively. The samples of the Laser Flash and the dilatometer were machined with the convectional lathe. First, a straight turn was done with the corresponding diameter, and after a cut off with an approximate height. Finally the height was adjusted in a grinding machine. For the DSC, due to the small shape, it was necessary first to machine a cylinder of 4 mm diameter and then it was cut it in a slow speed saw for small pieces. The result was an approximate height, around 0.5mm which was grind with a sandpaper until the weight was adjusted to 42.1 mg.

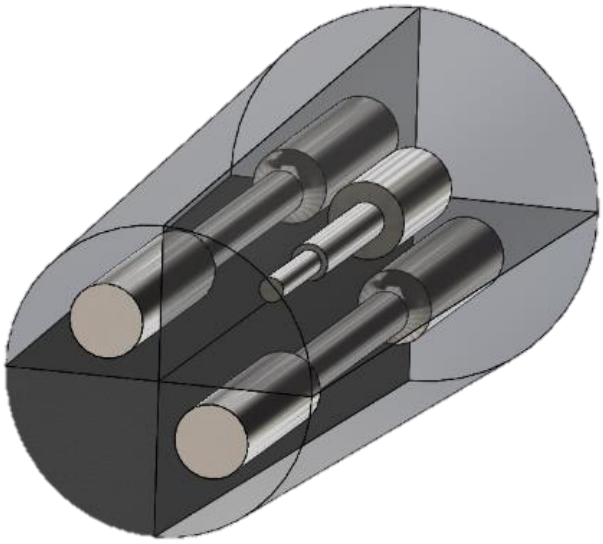

Figure 15. Schematic display of the different samples in the cone.

3.2 Thermal test

3.2.1 Dilatometer

Dilatometry is a method that takes a highly accurate measure, of volumetric changes in solids, melts, powders and pastes at preprogrammed rate of temperature changes and with negligible sample strain. The dilatometer used in the laboratory was the Netzsch Dilatometer 402C, which works along with a software called Proteus.

The dilatometer measurement, is conducted with the pushrod method, where a cylindrical sample is inserted into a sample holder brought into contact with the pushrod. The contact force that the pushrod exerts, is kept it as a constant in the software and allows the operators to measure samples without any breakage or deformation risk. Once the sample is fixed by the pushrod, the furnace can be

closed and the atmosphere set with a gas that prevent the oxidation during the experiment. During the experiment the temperature is controlled with a thermocouple place it by the sample, and the thermal expansion in the cooling or the heating is measured by the displacement system, which the pushrod is connected to.

Figure 16. In the left the Netzsch Dilatometer 402C used, and in the right a schematic placement[31].

In this study, the samples have a shape with 6mm of diameter and 12mm height, and was set it a load of 40 cN in the pushrod and a helium atmosphere. The helium atmosphere was vacuumed and filled three time to ensure the purity of the environmental helium. The experimental variables were, 10 k/min for heating and cooling rate, and maximum temperature of 950 ^{0}C. Once the maximum temperature was achieved, the temperature was held it during 5 minutes, before the cooling started. The device requires calibration before testing samples. This calibration was done with a standard aluminum oxide sample and with the same parameter abovementioned.

The results given from the dilatometer are the dimensional changes in one axis versus the temperature or time. An example of the result is given in the **Figure 17**. With the data collected it is possible to see an anomaly in the trend due to the transformation of the pearlite to austenite and austenite to pearlite. Moreover, it is possible to calculate the lineal thermal expansion in the lineal parts of the graphic with the following formula:

$$\alpha_E = \frac{\Delta L}{\Delta T} \cdot \frac{1}{L_0} \text{ [32]} \qquad \text{(Equation 2)}$$

Where:

α_E: expansion coefficient

ΔL: change in length

ΔT: change in temperature

L_0: initial length

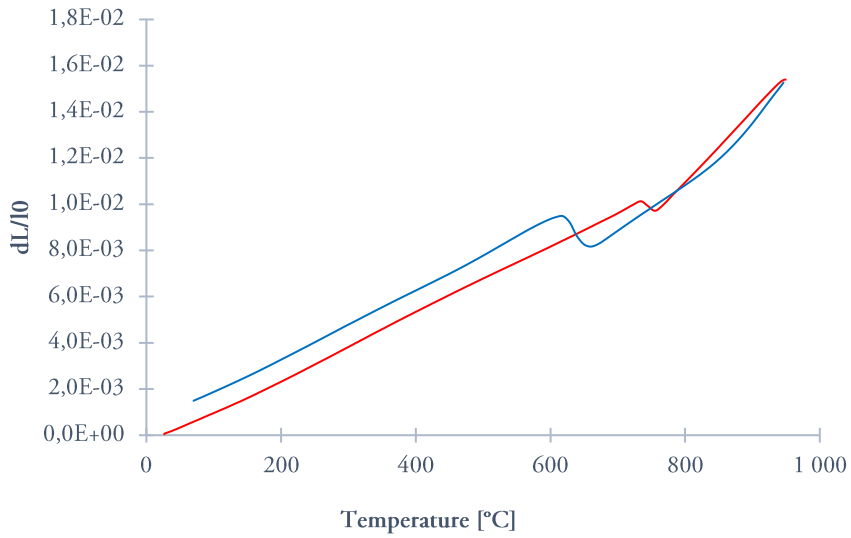

Figure 17. Dilatometer results, where the red line sows the behavior during the heating and the blue one during the cooling process.

3.2.2 Differential Scanning Calorimetry (DSC)

The differential scanning calorimetry is the most used thermal analysis method due to its versatility and explanatory power. From the DSC we can collect a large amount of data such as characteristic temperatures, enthalpies, specific heat capacity, etc. The DSC used was the Netzsch DSC 404 C Pegasus shown in the **Figure 18**, and in this project was useful along with Proteus software to calculate the specific heat at constant pressure Cp.

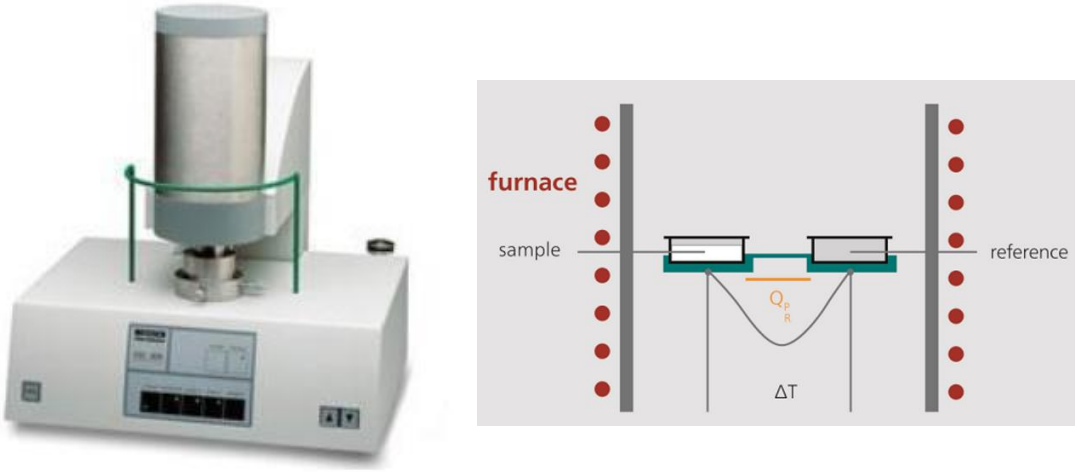

Figure 18. Figure 19. Netzsch DSC 404 C Pegasus on the left and schematic picture of the crucibles on the right [32].

The DSC basically, it is a furnace with two crucibles the sample and the reference (usually empty) where the temperature is known every moment thanks to the temperature sensors and compared it between both crucibles. First of all "base lines" i.e. with the empties crucibles, have to be run it, until the difference between

its results is less than 1mV. Then the DSC was run it with a standard sample and after, finally the sample could be test it. For all the times the DSC was run, it was necessary to set the atmosphere with a gas that prevent the oxidation during the experiment. Then it is necessary to set some variables as well such as the sample's weight, the heating and cooling rate.

DSC record the difference of temperature between both crucibles. Generally, the reference heats faster than the sample due to the heat capacity of the material but at constant heating rate, the temperatures of both crucibles present a parallel increasing so the ΔT plot it is constant until a sample reaction is achieved. The plot of the differences between both temperatures when they are not parallel generates an area correlated with the heat content of the transition (enthalpy) with which it could be possible to calculate the Cp thanks to the standard measure and the software Proteus[32].

In this study, the temperature ratio was 10 K/min either for heating or for cooling. The maximum temperature achieved was programed in 1270 ^{0}C and the atmosphere was argon with a flow of 50 ml/min. Every cycle took four hours and a half and it was necessary at least, to run two times the cycle empty in order to calibrate the device and after the standard sapphire and finally the samples. The standard sapphire used was one of 42,1 mg and it is necessary to calculate the Cp. The samples were machined with a preform of 4 mm of diameter and 0,5 mm height and after adjusted to 42,1 mg like the sapphire. The Cp was calculated with the ratio method in the Proteus software for each segment and after plot it, as it shown in **Figure 20**.

Due to problems with the apparatus where some samples were merged with the crucible and subsequent breakdown of the apparatus. It was not possible to run the sample 4.

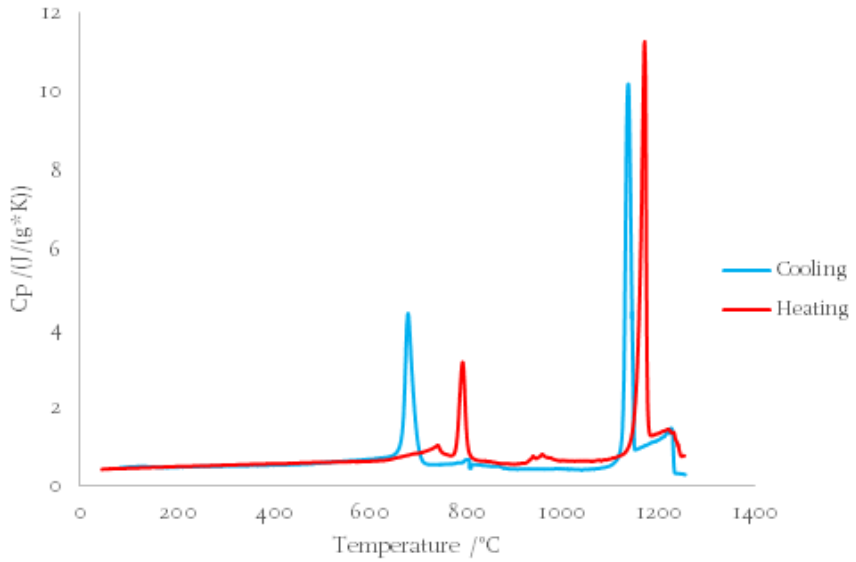

Figure 20. Example of the DSC results.

3.2.3 Laser flash

Laser flash is the most common method for measure the thermal diffusivity due to it is a non-contact, non-destructive method. The apparatus used was the Netzsch LFA 427, shown in **Figure 21**.

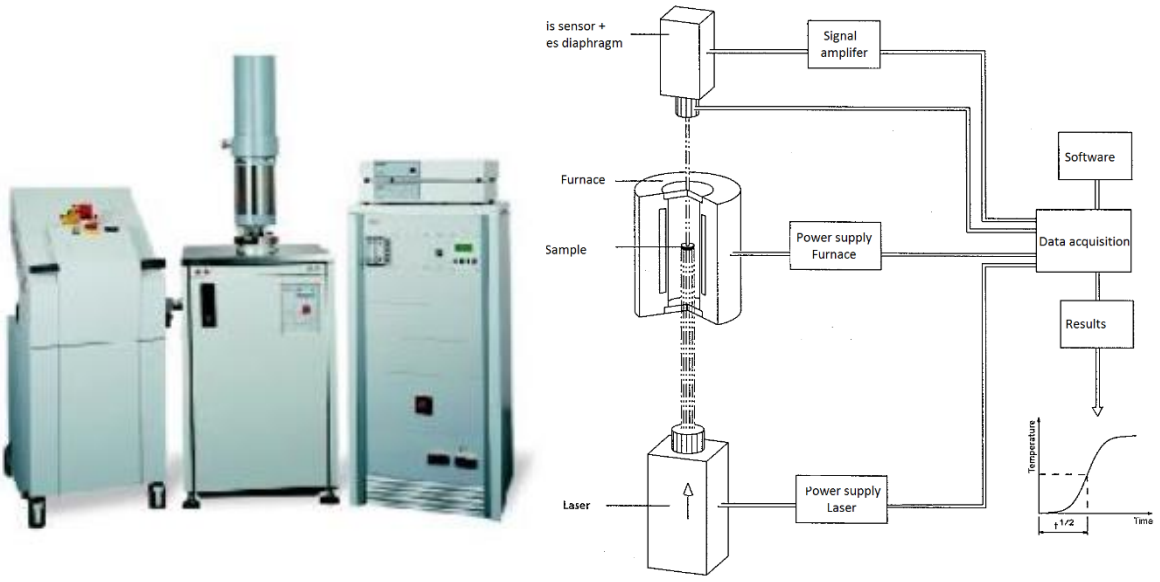

Figure 21. On the left the apparatus used, and on the right a schematic representation [33].

The laser flash, measures the time and the temperature changes in one surface of the sample with an infrared detector, while the other face is reached by a short energy pulse (the laser) that heats the surface. The laser shots were done at different temperatures and with the enough gap between them to stabilize the temperature. The experiment is executed in a protective atmosphere to prevent the oxidation, and under a preprogramed variables such as the cooling and heating rate, maximum temperature, the exactly thickness, the flow rate of the gas, the voltage of the laser, etc. [33].

In this study the samples used were a cylinder 12,5 ± 0,1mm of diameter and 4,375 ± 0,3mm height which was necessary to roughen with an air sand gun to prevent the laser reflected. Once the sample was in the holder and the furnace closed the atmosphere was set it up with argon, and a flow rate of 100ml/min. The cycle was programed with the laser voltage of 450 V, a rate of 10k/min either for heating or for cooling, maximum temperature 900 ^{0}C and the laser's shots were: 10 at room temperature, 10 at 150 ^{0}C and after 5 every 150 ^{0}C until 900 ^{0}C, in the cooling the cycle was the reverse. All this cycle took around 10 hours.

The result were 75 shots which is obtained a plot like the one in the left of **Figure 22**. From that graphic, it was taken just the time corresponding with the 50% of the final temperature [34]. Then the software calculate the thermal diffusivity with the following equation:

$$\propto_D = 0{,}1388 \cdot \frac{L^2}{t} \quad [35] \qquad \text{(Equation 3)}$$

Where:

α_D: thermal diffusivity.

t: is the time corresponding with the 50% of the final temperature.

L: sample thickness.

Finally, the average of all the shots at the same temperature is done and plot it with the temperature as it is possible to see on the right of the **Figure 22**.

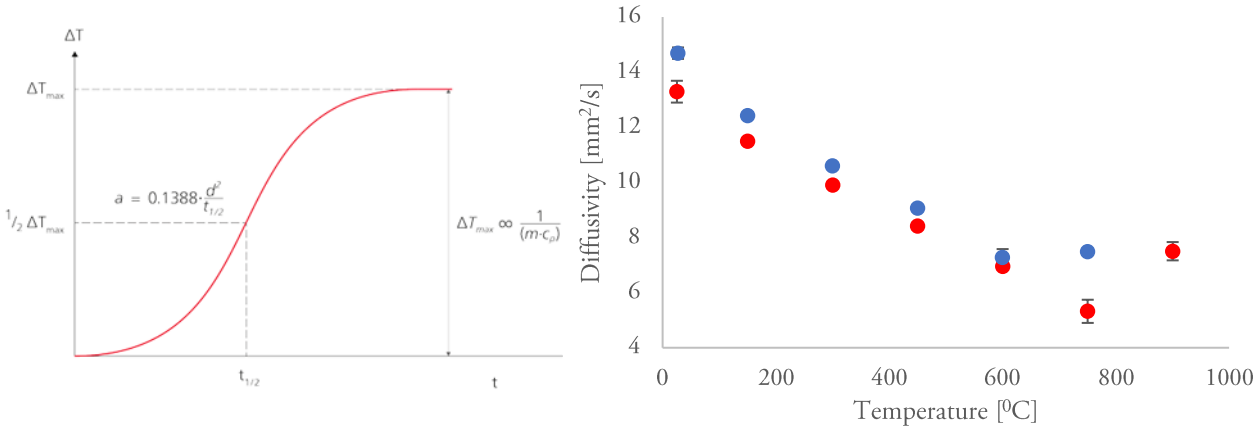

Figure 22. Laser flash results.

3.2.4 Thermal conductivity

Once it was obtained the results it is possible correlated the data in order to calculate the thermal conductivity at different temperatures. The expression which enables to calculate the conductivity is this one:

$$\lambda(T) = \rho(T) \cdot C_P(T) \cdot \alpha_D(T)$$ [36] (Equation 4)

Where:

$\lambda(T)$: is the conductivity at temperature T.

$\varrho(T)$: is the density at temperature T.

$C_P(T)$: is the specific heat capacity at temperature T.

$\alpha_D(T)$: is the thermal diffusivity at temperature T.

As it can be seen $\alpha_D(T)$ and $C_P(T)$ are known, they were calculated with Laser flash and DSC respectively but the $\varrho(T)$ not. The density at room temperature was calculated with the Archimedes' principle and was extrapolate to higher temperature with the following equation:

$$\rho(T) = \frac{\rho_{RT}}{1+3\cdot\alpha_E\cdot(T-T_{RT})}$$ [37] (Equation 5)

Where:

$\varrho(T)$: density at temperature T.

ϱ_{RT}: density at room temperature.

$\alpha_E(T)$: lineal thermal expansion at temperature T.

T_{RT}: room temperature.

So now all the variables are known but tedious calculation were required before the thermal conductivity was calculated, note that not all the apparatus record the data in the same way. For example the laser flash took data in fourteen different temperatures but the DSC took data in 12000 different temperatures. After the interpolation and extrapolation required, the thermal conductivity was calculated from room temperature to 600 ^{0}C and the result looks like the **Figure 23**. The cooling rate was ignored for calculate the conductivity because the data is not comparable, since the DSC melted the material and the dilatometer and the laser flash not.

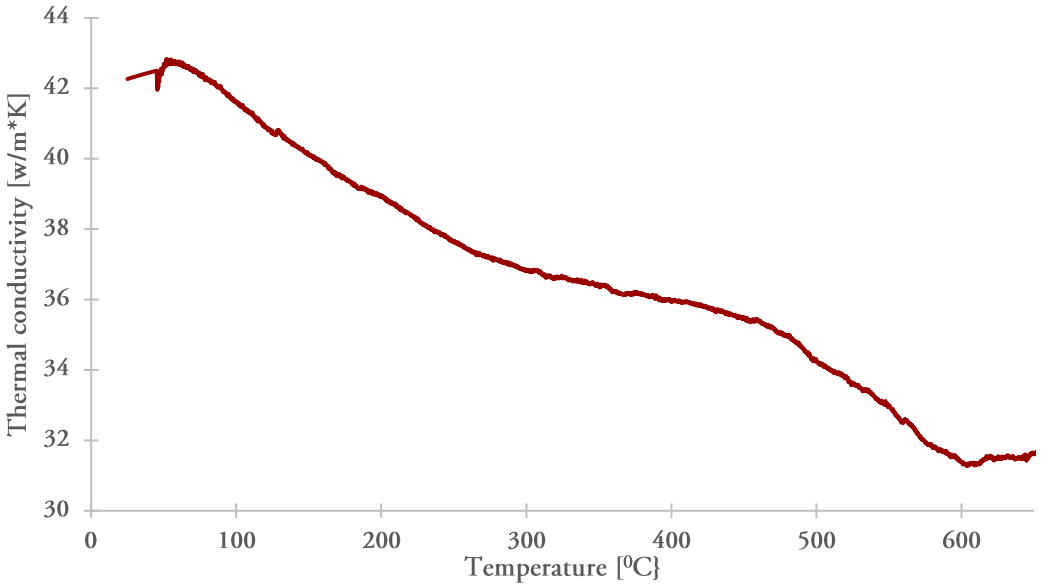

Figure 23. Thermal conductivity.

3.3 Tensile test

The best form to characterizing the mechanical properties of the lamellar cast iron is the ultimate tensile strength in which the strain is controlled until the fracture of the sample. The tensile test has been done on the Zwick/Roell Bus-hypu testing machine.

The tensile bars were machined according with a Volvo standard, where the samples have a 7 ±0,04 mm of diameter in the minimum section, 50 mm of gauge length and 12 mm of diameter in the maximum section with a fillet between both sections of 5 mm radio. For each cone it was taken two tensile bars, so four bars of each composition were tested. The machine was programed with a strain rate of 0,0025

following the standard, SS-EN ISO 6892-1:2009. The measure it was tried to use the extensometer but it did not work properly so it was used the Laser that is less precise. Anyway, for the UTS's measure does not matter.

Several result were taken such as E module, the UTS, the elongation and the force at different points, etc. The **Figure 24** illustrate an example of the results in which is possible to see the tension in function of the strain.

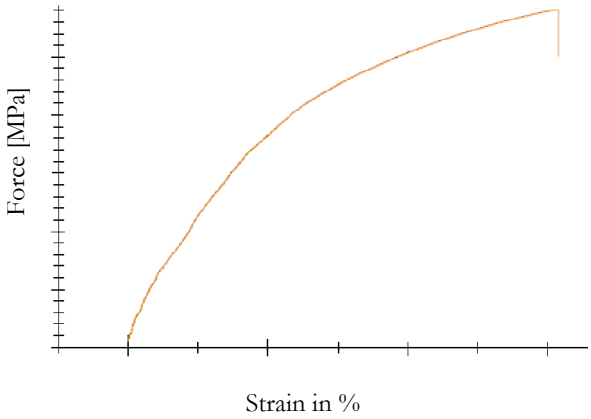

Figure 24. Tensile test graph.

3.4 Microstructure

The microstructure was checked in the microscope Olympus GX71F, in order to know more about how are the samples, with which was worked and explain the results obtained. In the study three different pieces were examined, all of them were taken from the tensile test sample. Two of them are cylinders from the maximum and minimum section and the third one is a transverse section from the minimum section. **Figure 25** shows the disposition of the samples taken.

Figure 25. Tensile test bar, where the three on right are the ones used and in the left we can see where the samples were.

Several processes were required before the examples were ready for the microscope. After cut the samples with the slow speed saw, the samples were mounted in a baquelite holder with a cylindrical shape of thirty millimeters of diameter. This mounting process, was done with the Struers Citopress. Then the samples were grinded manually and after, polished with the machine Struers Tegramin. The samples were ready once they passed through all stages of grinding and polishing and the final rugosity was 1µm. After several micrographs were taken in the in the Olympus GX71F microscope with different magnification.

With 2,5 magnification, it was done the micrograph shown in the **Figure 26** where all the fracture is shown. For that micrograph was necessary to take two micrograph and after with Adobe Photoshop they were merged.

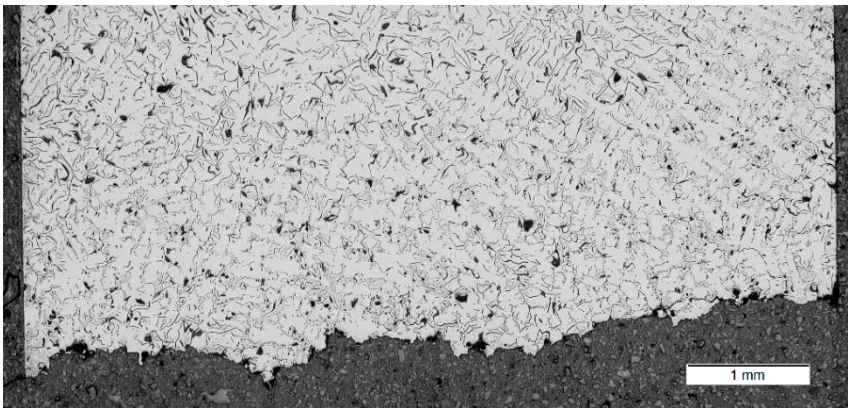

Figure 26. Example of one fracture's micrograph.

It was done a graphite analysis with the Olympus Stream motion software. For that, fifteen micrographs with ten magnification were taken. Five of them from the fracture and the other ten from the 12 millimeters section. The micrographs were randomly taken in the sample, but always with the same pattern. Finally, the micrographs were analyzed in the Strean motion sofware, which returns several parameters such as the graphite fraction, graphite size, graphite form, etc. The **Figure 27** shows a random micrograph which was used for the analysis. The analysis was done following the standard ASTM A 247.

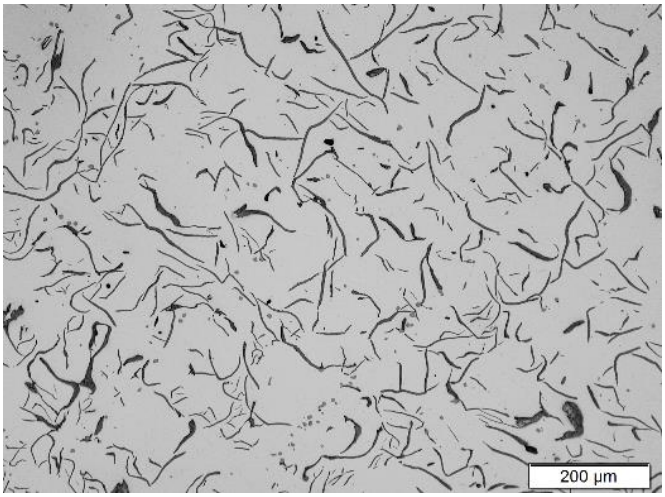

Figure 27. Example of one micrograph that was used in the Stream motion.

Once the not etching micrograph were taken, the next step was to etch the surface of the samples in order to see the matrix and the different components in the microstructure. The etching was done with picric acid, which is very dangerous, explosive, poisonous and flammable, among other features. The etching was done carefully, first the picric had to be warming up, until the 92 ^{0}C. Then with the help of one magnet the samples were submerged in the acid during around 10 minutes. After a good color etching, the sample was ready to be checked in the Olympus GX71F microscope. The structure seen is the one shown in the **Figure 28**.

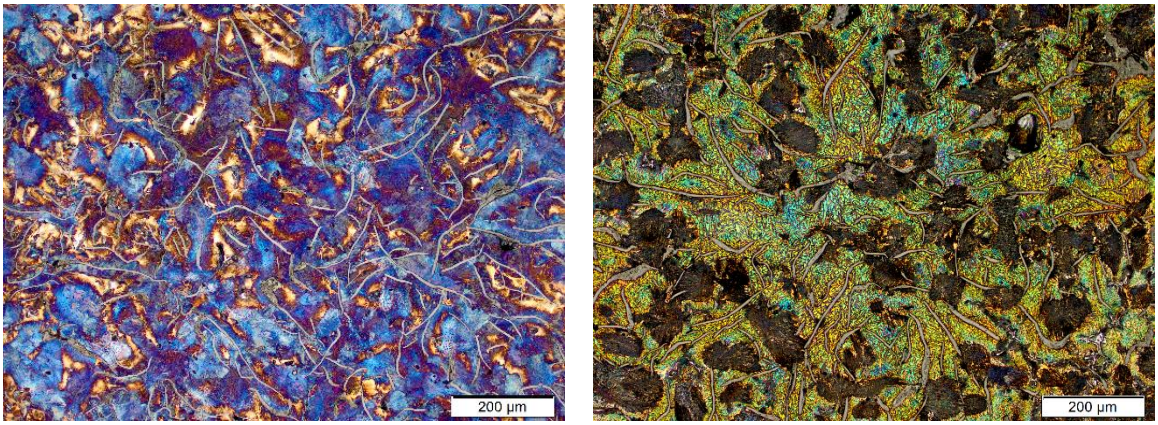

Figure 28. Examples of the microstructure after the etching, left pearlitic matrix and right ausferrite matrix.

4 Findings and analysis

All the results achieved are shown in this section in an objective way. The section is structure in the different devices used along the thesis.

4.1 Dilatometer

From the dilatometer the characteristic value is the thermal expansion. The thermal expansion was calculated with the "least squares" method, which calculate the straight line that best fits in the given data. So there are fifteen different thermal expansion values corresponding with the different lineal parts in the seven different materials. The lineal section corresponds with the two straight parts interrupted by the solid state transformation. An example graph is in **Figure 17**. The individual plots of each material are in the appendices 9.2 and the thermal expansion values are shown in **Table 3**.

Table 3. Thermal expansion values.

	Lineal sections [^{0}C]	*Thermal expansion [K^{-1}]*
A	RT – 725	1,3800E-05
	745,5 – 954	2,2581E-05
2	RT – 735,5	1,4688E-05
	756 – 931,5	2,4908E-05
3	RT – 737	1,5129E-05
	757,5 – 933	2,6009E-05
4	RT – 734,5	1,4376E-05
	755 - 923,5	3,0858E-05
5	RT – 734,5	1,4428E-05
	755,5 – 921	2,9694E-05
6	RT – 736,5	1,4609E-05
	757,5 – 919,5	2,7659E-05
8	RT –– 453,5	1,7260E-05
	463,5 – 727	1,5238E-05
	748 – 934	3,4591E-05

It can be seen that except the 8 composition all the others have a first lineal section until approximately 730 ^{0}C, and another one from around 750 ^{0}C until 930 ^{0}C. So it is possible to relate the thermal expansion with the different Mo content of each composition as it is shown below in the **Figure 29**.

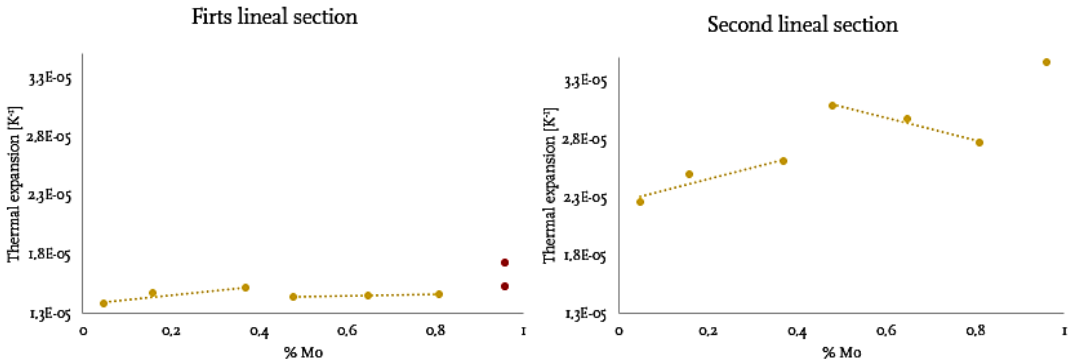

Figure 29. Thermal expansion as function of the Mo percentage. The red points corresponds with the two values of the composition 8 in the first lineal section.

From the dilatometer data, it is possible to see a volumetric change around 730 ^{0}C as well. That volumetric change is possible to relate with the amount of molybdenum and it could be useful to understand, what happened. The graph is sown above in the **Figure 30** where is shown the volumetric changes for the heating and for the cooling. In the figure below, there is a schematic explanation of which

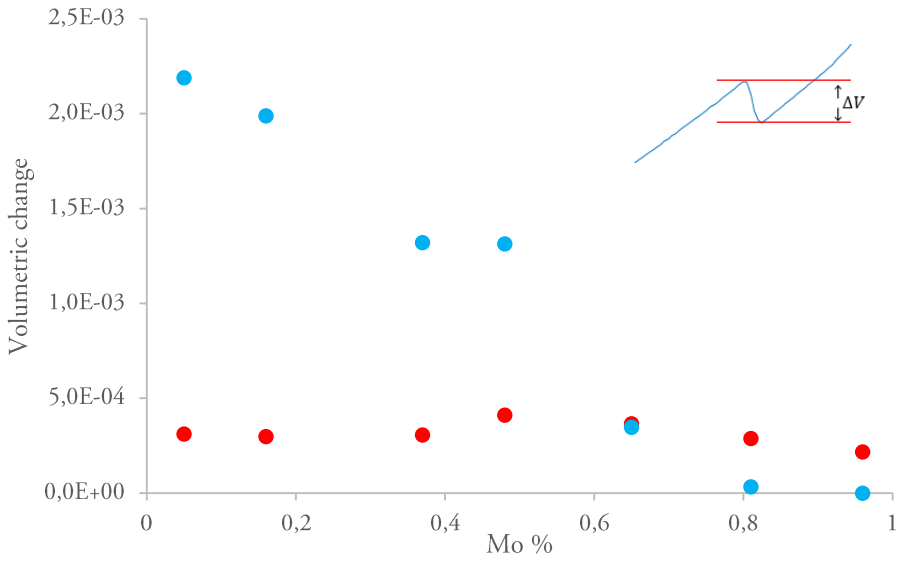

values are represented as well.

Figure 30. Volumetric changes during the heating in red and in blue during the cooling.

4.2 Differential Scanning Calorimetry

The specific heat at constant pressure calculated with the DSC, it is shown below. First in **Figure 31** is shown the heating and a zoon of the data used for calculate the thermal conductivity is done. I.e. from room temperature to 600 ^{0}C. In the **Figure 32** is shown the cooling which was used for calculate an integration very useful for see which compositions react more during the solidification under the same cooling rate.

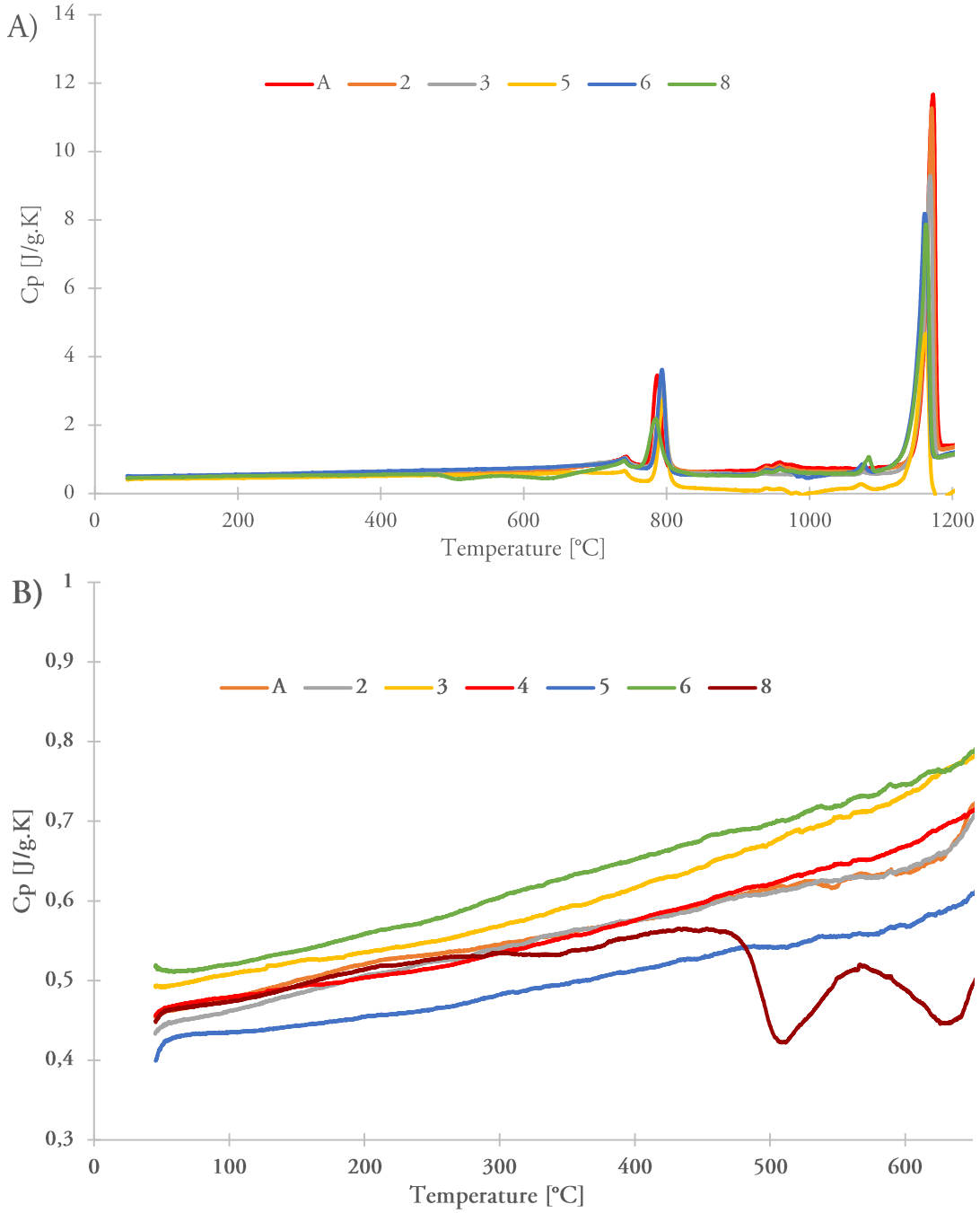

Figure 31. Specific heat during heating, A) is the full graph and B) correspond with the data used for the conductivity including the interpolation of composition 4. Please note that figures have different scales.

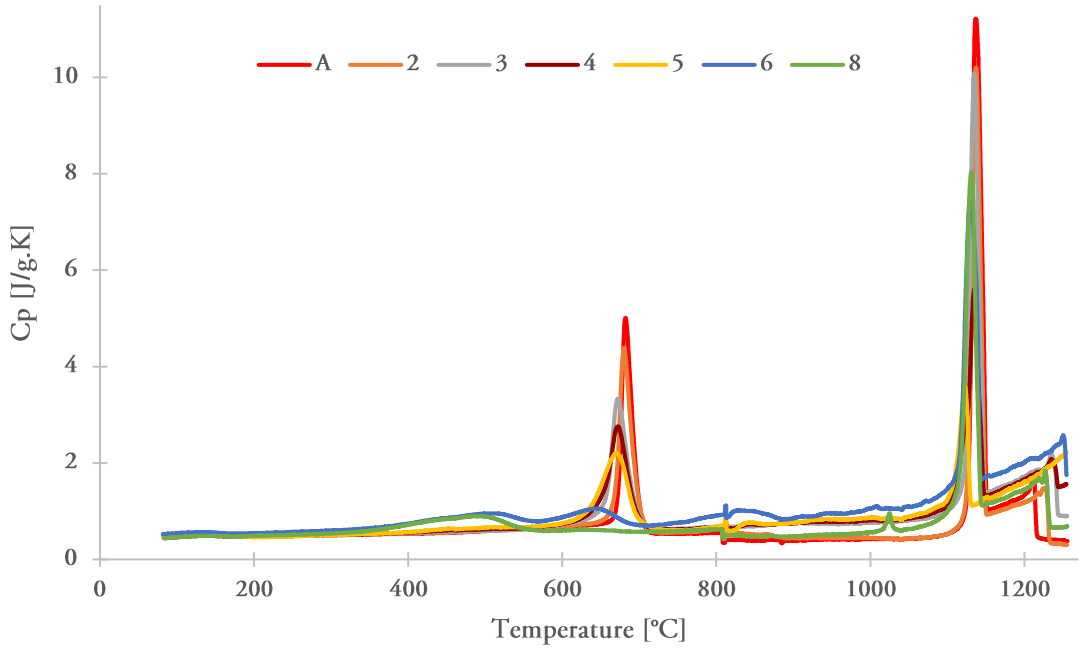

Figure 32. Specific heat during the cooling.

In order to compare the different amounts of energy of each composition during the eutectic transformation. An integration was done under the graphs between 600 and 720 ^{0}C. A zoon of where the integration was done and the result is shown in **Figure 33** and **Figure 34** respectively.

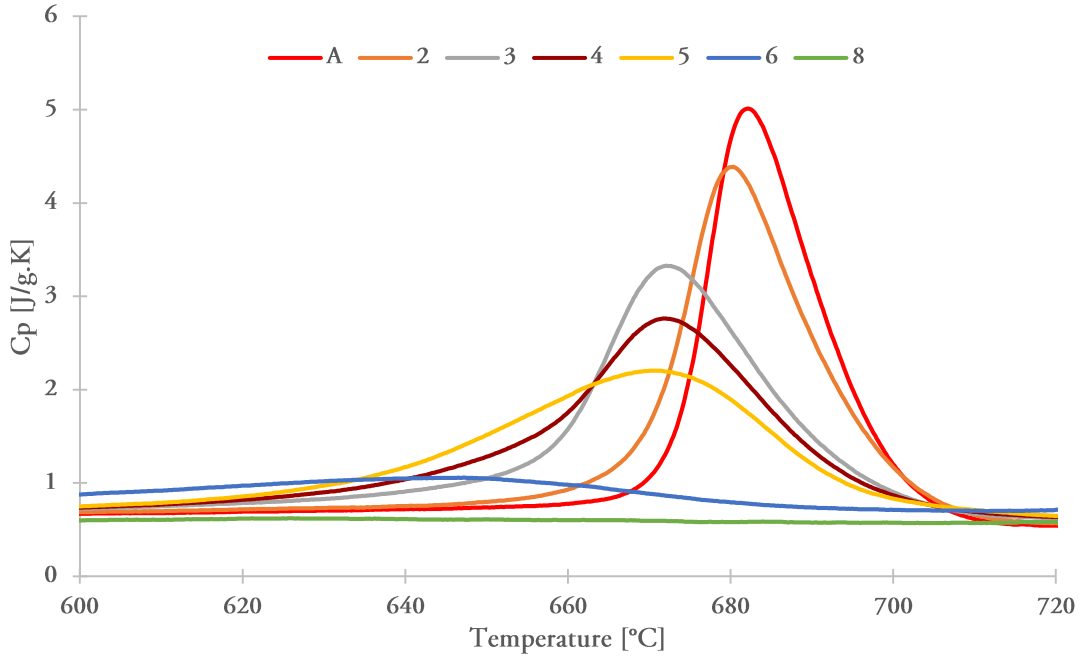

Figure 33. Graphs integrated in the integration interval.

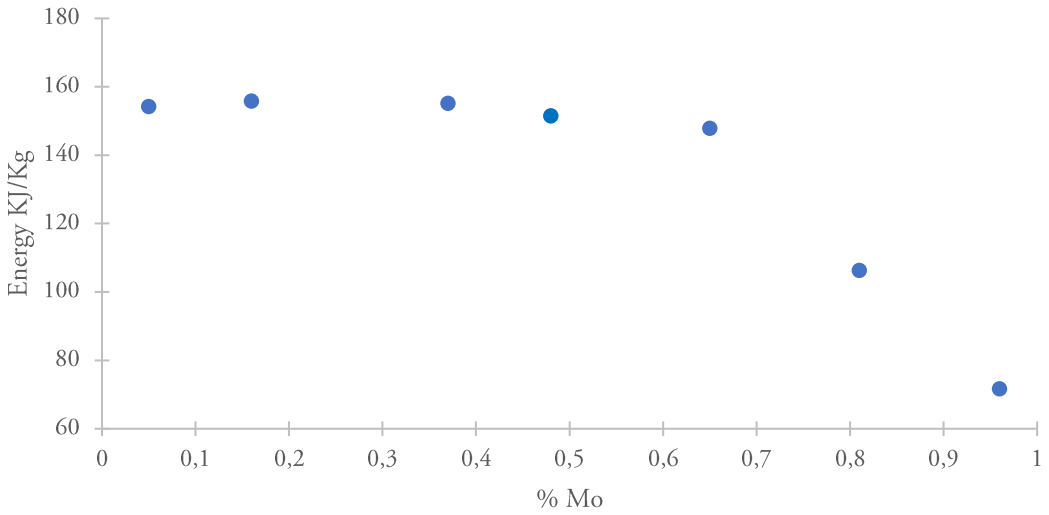

Figure 34. Values of the integration as function of Mo.

4.3 Laser flash

The thermal diffusivity from the laser flash was collected such scatter graph due to the temperature were measured just in 25, 150, 300, 450, 600, 750 and 900 ^{0}C. Therefore, in the **Figure 35** is shown the average of the diffusivity measured in each temperature without the error bars, in order to do it clearer the graph. However, the data of the thermal diffusivity with the standard deviation is attached in the appendix 9.3.

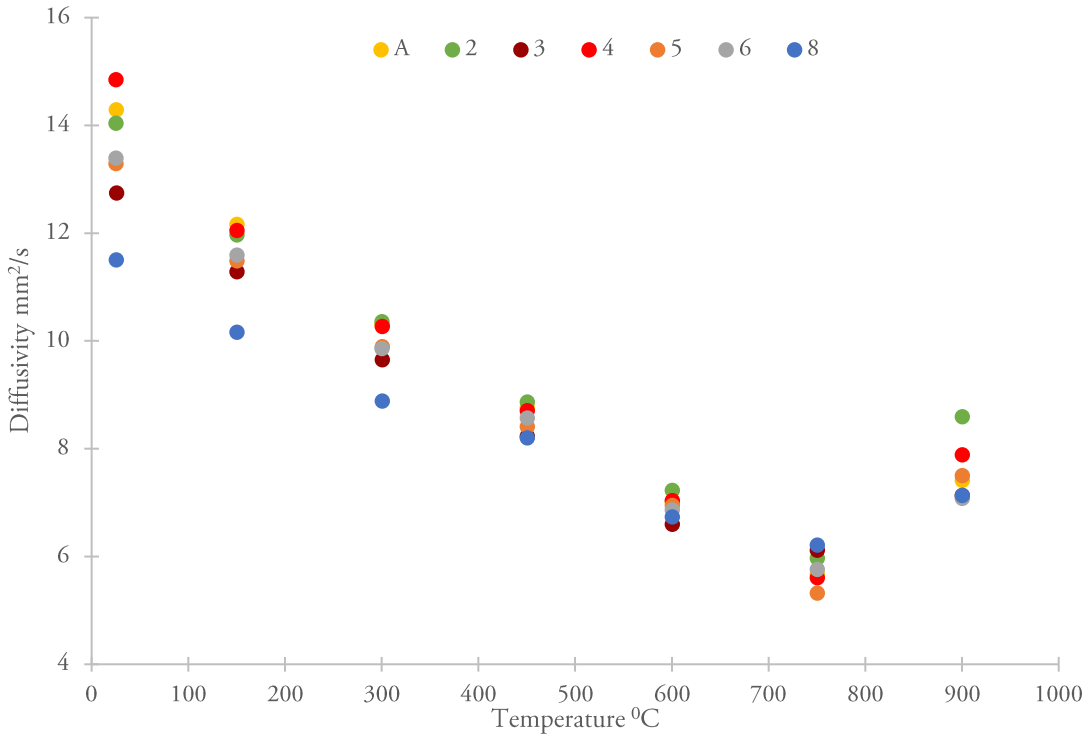

Figure 35. Results of thermal diffusivity.

4.4 Thermal conductivity

The thermal conductivity was calculated in a huge workbook in excel, and the results are shown in the **Figure 36**. The composition 8 had to be cut it around 450 ^{0}C because it does not have a lineal expansion coefficient in this zone.

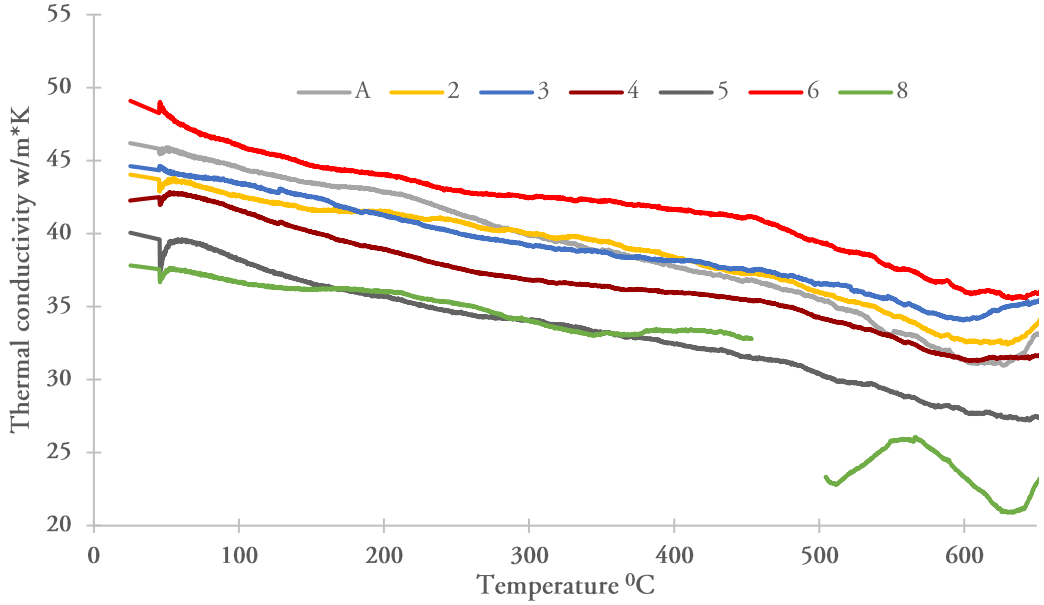

Figure 36. Results of thermal conductivity.

4.5 Tensile test

The average of the Ultimate Tensile Strains of each concentration is exposed in the **Figure 37**. Where X-axis is the molybdenum content and Y-axis the average of the UTS. In the graph, there are an error bar that shows the standard deviation. Two trendlines were added because the behavior of the UTS with the molybdenum at first sight, shows two different tends. Both of them increase with the molybdenum content but there are a notable discontinuity between both. In the appendices 4 it is possible to consult more data about UTS.

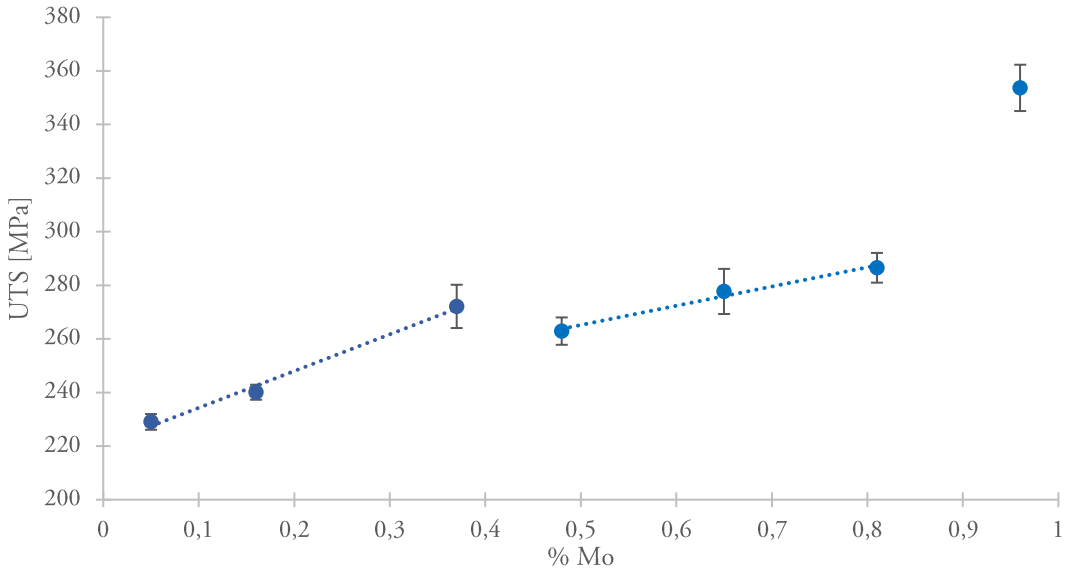

Figure 37. Effect of Molybdenum on UTS.

Even though the main feature of the lamellar grey cast iron in the mechanical properties is the UTS as it was said in the theory, the Emod and the elongation were measured as well. The graph of Emod and the elongation were represented with the molybdenum content. The trend of this line does not fit as good as in the UTS but both of then sown an increase tend. The Emod and the elongation are in **Figure 38** and **Figure 39** respectively.

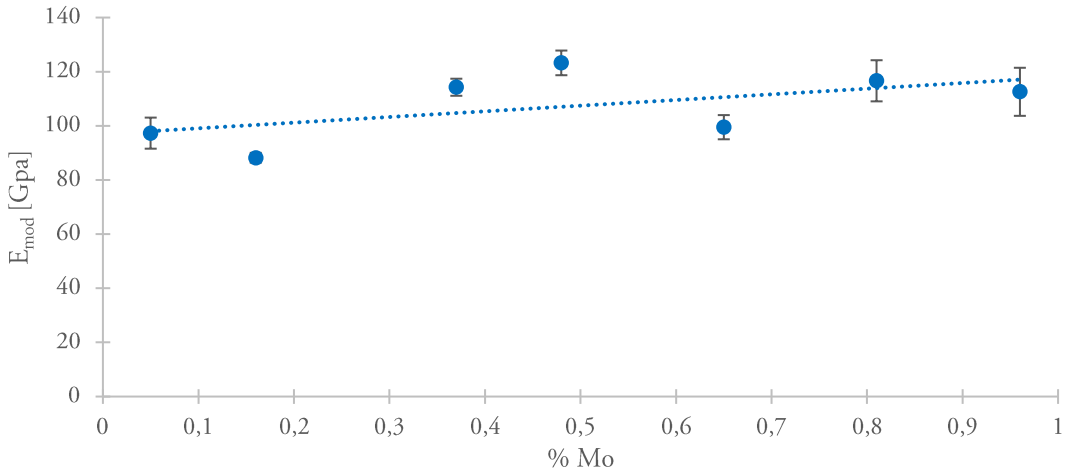

Figure 38. Effect of Molybdenum on E_{mod}.

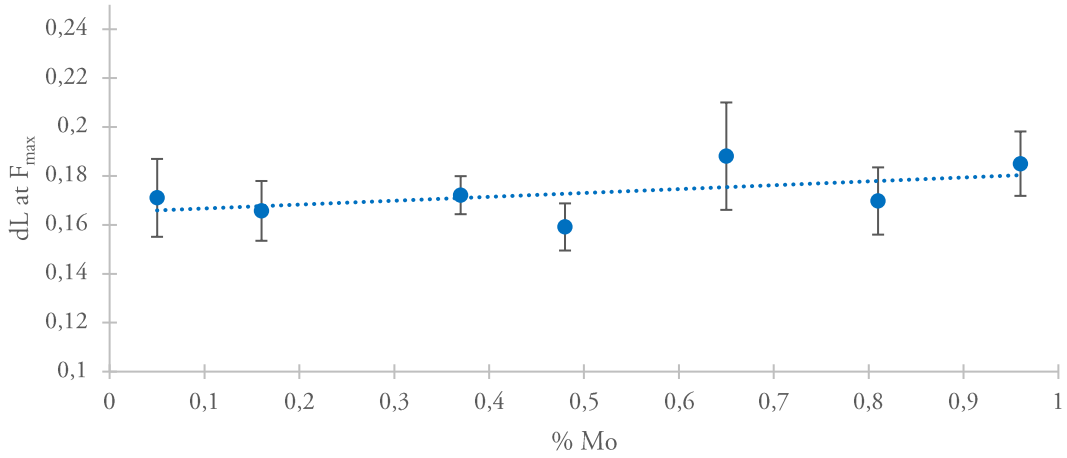

Figure 39. Effect of Molybdenum on dL at F_{max}.

4.6 Graphite

The data given by the Olympus Stream Motion software were exported to excel and after a graphic was done with the graphite shape VII and the Molybdenum content. The graph is in the **Figure 40** and shows a decreasing amount of graphite shape VII as the Mo content increase. The graphite fraction does not show any trend as it possible to see in **Figure 41**.

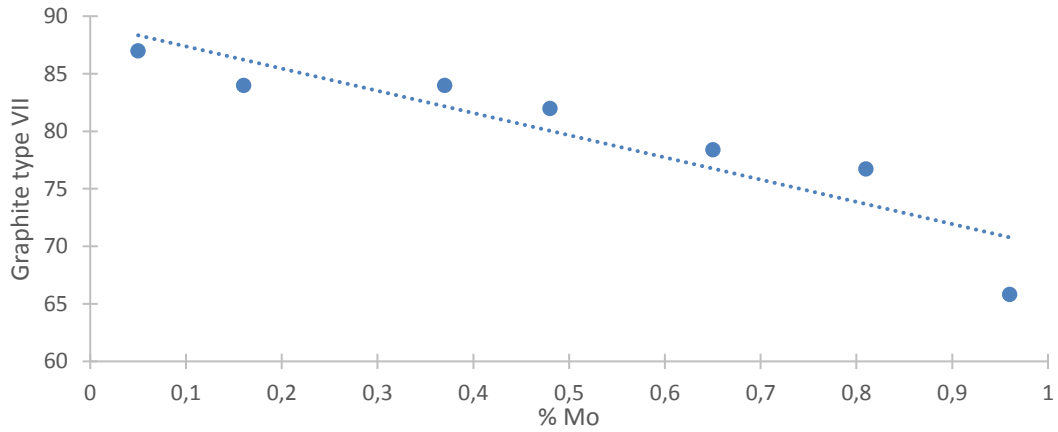

Figure 40. Effect of Mo in the graphite shape.

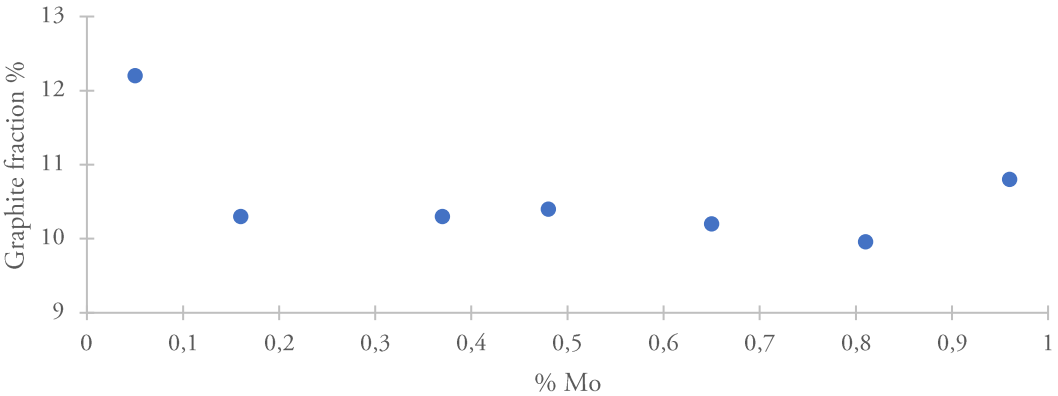

Figure 41. Effect of Mo in the graphite fraction.

The graphite type found was graphite type A and E in different proportions. That proportions were measured and in the **Figure 42** are shown the proportions of each composition in a graphical way. It is not possible to see any relation with the molybdenum content neither.

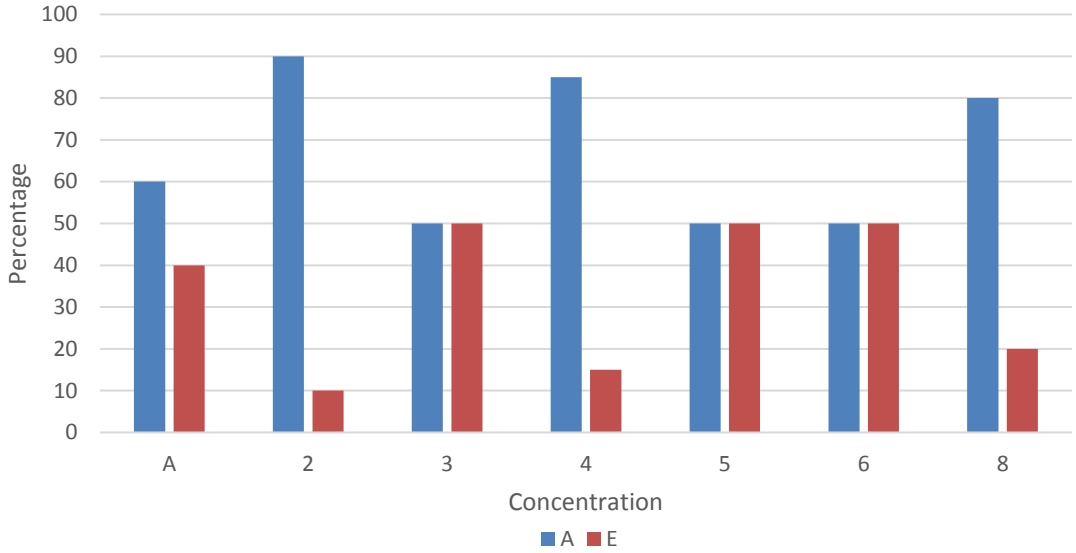

Figure 42. Graphite type of each composition.

4.7 Matrix

Despite it was not made a quantitative analysis, the micrographs from the matrix were very useful to draw the conclusions, because it is possible to see the changes in the microstructure that are occurring as the molybdenum content increases. E.g. The presence of ausferrite with increasing Mo content. In the **Figure 43** are some examples of them, but in appendix 9.5 the micrographs of all compositions are exposed with different magnifications.

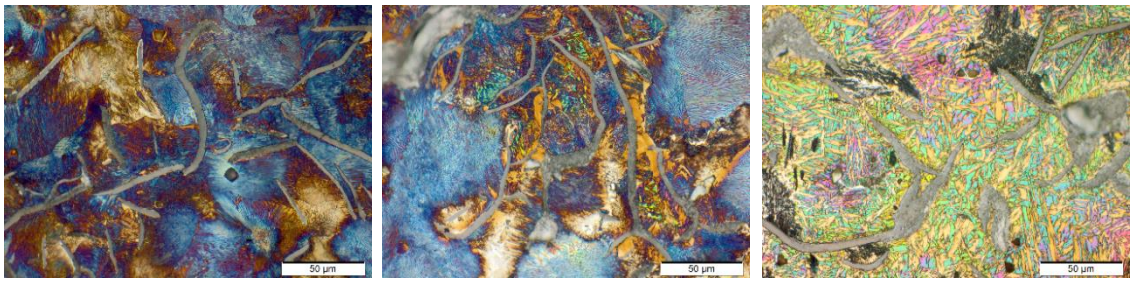

Figure 43. Example of how was appearing the asuferrite. Composition 2, 6 and 8 respectively.

5 Discussion and conclusions

This chapter consist on a discussion of the method and implementation carried out and the results taken from the different experiments and calculation.

5.1 Discussion of method

The discussion of the method is divided in different sections, in order to facilitate the understanding of the reader.

5.1.1 Material

The studied hypoeutectic lamellar cast iron, with different Molybdenum levels was provided by Volvo Powertrain. The cast was done in big mold where it is unknown the disposition of each sample in the mold. Maybe, in order to have more comparable data it would have been more suitable to have the samples from the same zone of the mold. The reason is because the samples from the same part of the mold would have the same cooling rate or at least very similar.

5.1.2 Thermal tests

The LFA and the dilatometer were running from RT to 900 ^{0}C so if it checks the carbon diagram in the **Figure 4**, it is possible to see that it was crossed a eutectoid line, during which is not possible to calculate the thermal conductivity. The DSC was running up to 1200 ^{0}C so the material was remelted, and during eutectoid transformations the thermal conductivity it is not possible to calculate neither.

Besides the thermocouples in the apparatus are not place it in the same way so the eutectoid transformation it was not measured at the same temperature in all the apparatus. As a result of that, there is a big gap in the conductivity graph. For future studies, I will recommend go up to 600 ^{0}C if it is just necessary calculate the conductivity in an operating range for industrial application. On the other hand from a didactic point of view it was really useful to run the apparatus up to 900 ^{0}C and 1200 ^{0}C, especially the dilatometer and the DSC because it has facilitated the understanding of what happens when you add Mo in cast iron.

At the time of collect the data, from the apparatus it was necessary to adapt it, in order to calculate the thermal conductivity. First the DSC start to collect data in 45^{0}C and all the others at 25 ^{0}C so after see that the Cp has a lineal part at the beginning, an extrapolation was doing until 25 ^{0}C. In the laser flash an interpolation was done, the reason for done that was because the diffusivity was measured every 150 ^{0}C, so for do a clearer graph the data between the measured was interpolate like a straight line, along all the temperature point measured by the DSC. After that, the density was calculated easily in all the temperature point measured by the DSC as well, except where the expansion coefficient was not constant. When it was constant, the expansion coefficient was calculated with "least squares" method because it is the best method to find the straight line that fit in different data. After

all the data were in a properly way, the thermal conductivity was calculated according with the equation 4.

5.1.3 Tensile test

In retrospect, the tensile test was wanted to conduct with the extensometer like other studies with lamellar cast iron such as [38]. Due to a technical problem with extensimeter, it was decided to use the laser method. Which is not very precise when it measure the E_{mod} therefore the elastic zone neither but for UTS measure, the accuracy does not depend of the extensimeter. Moreover for use the extensimeter is necessary to stop the strain, in order to remove the extensimeter safely, which it could affect the measure of the UTS.

As it was mention in the theoretical background, there is not an elastic zone in lamellar cast iron so the E modulus does not make too much sense. Therefore, I would not dare to conclude that the use of the extensimeter doesn't make sense in lamellar graphite iron but in this case and for similar studies I will recommend not to use it, because if it is used, the UTS's measure could be affected just for have more accurate data of the E_{mod} which, as it was explained it is not a simple issue in the lamellar cast iron.

5.2 Discussion of findings

The discussion is structured in function of all devices used and all parameter taken from each device are discussed. Besides the order is different than it was using so far. The first study discuss is the tensile test, after it follows the dilatometer, DSC, laser flash and finally the conductivity results. The discussion, it is backed with the micrographs taken of the microstructure's matrix, which there are in appendix 9.5.

5.2.1 Tensile test

From the tensile test, as it was commented before, the relevant data for this thesis is the UTS. The UTS is shown in **Figure 37** as function of the molybdenum content. In that graph, as was commented it is possible to see two different trends and after the sample with more molybdenum as a pick in the UTS.

First trend, samples A, 2 and 3, show an increasing behavior in the UTS as the molybdenum content increase. As it was mention, Mo is known as a pearlite refiner, promote the ausferrite and generates carbides. The micrographs taken of the matrix show full prelatic matrix, and no sign of ausferrite. The optical microscope is not enough to see a refinement in the pearlite's lamellas but it is possible to see the grain size decreasing with the Mo content, **Figure 44**, and therefore increasing the UTS.

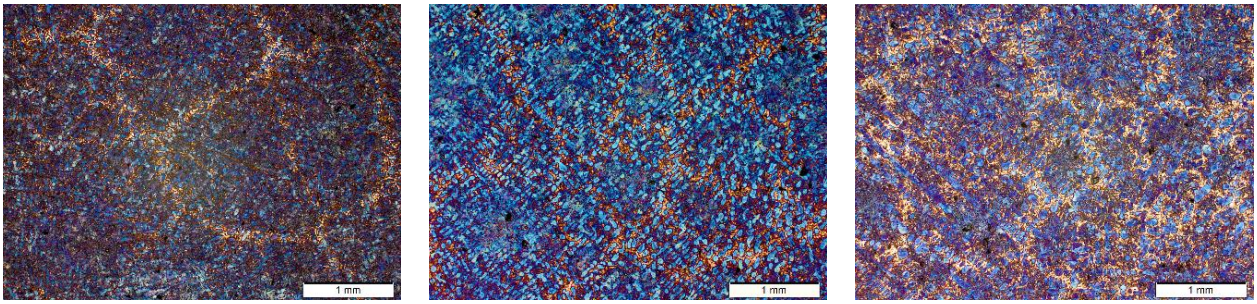

A **2** **3**

Figure 44. Matrix A, 2 and 3 with 2.5 magnification.

Then in **Figure 37**, the following trend, it is the one formed by composition 4, 5 and 6, which have an increasing behavior in the UTS as the molybdenum content increase as well, but breaks with the previous trend. Besides the UTS between 3 and 4 decrease, with values of 272 and 263 MPa respectively. This is a surprising values beforehand, because it wasn't expected a worsening of the properties with a 0,37% content of Mo. It was tried to explain it with the micrographs and with the graphite analysis. It was found that the graphite type E decrease and the type A increase in composition 4, also in the matrix micrographs it could say that the pearlite goes on with the refinement as it shown in **Figure 45** but with a bigger magnification it was found more carbides in composition 4 than in composition 5, as the **Figure 46** shows.

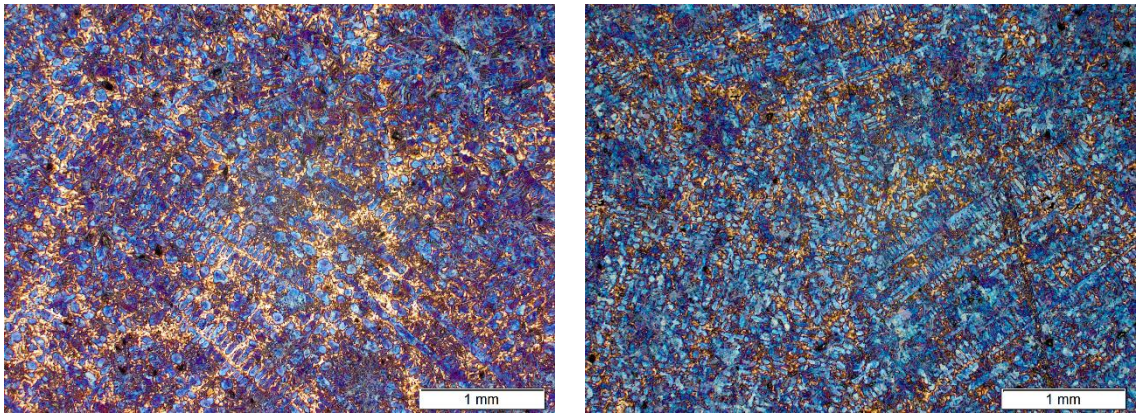

3 **4**

Figure 45. Matrix of composition 3 and 4.

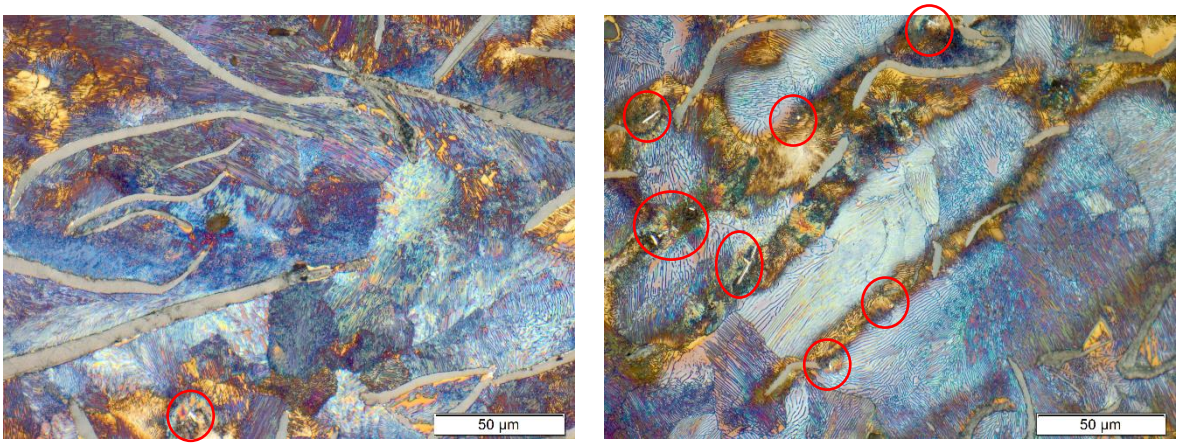

3 **4**

Figure 46. Matrix 3 and 4, showing the carbides.

As it was mentioned the molybdenum produces carbides that worsen the mechanical properties due to the high hardness and in the two micrographs of composition 3 and 4 with 50 magnification shows a significant greater amount of carbides. Furthermore the graphite type E has better mechanical properties than A so that is the reason of why the UTS decrease between 3 and 4.

Once explained the decreasing of UTS it could be reasonable to think that now on the following concentrations with more Molybdenum content, are going to have less UTS because more carbides are going to form. But it is not like that the trend is an increasing one. The reason it is found on the micrographs one more time. The micrographs of the compositions 5 and 6 shown the expected Ausferrite, which results in an improvement in the mechanical properties as reported in [26, 27]. In the **Figure 47** is shown the ausferrite from compositions 5 and 6.

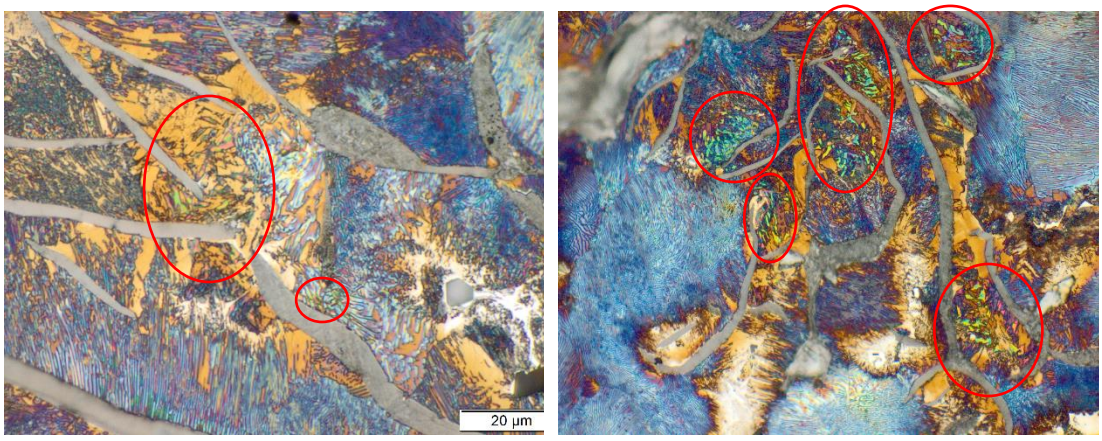

5 **6**

Figure 47. Matrix of compositions 5 and 6

Finally the composition 8 shows the greater UTS, and the answer after see the micrograph of the microstructure and the graphite analysis is undoubtedly because the pearlite matrix persistent until now, turns into an ausferrite matrix. The

micrographs of the composition 8 are in appendix 79 but below in **Figure 48** there is an example of that composition.

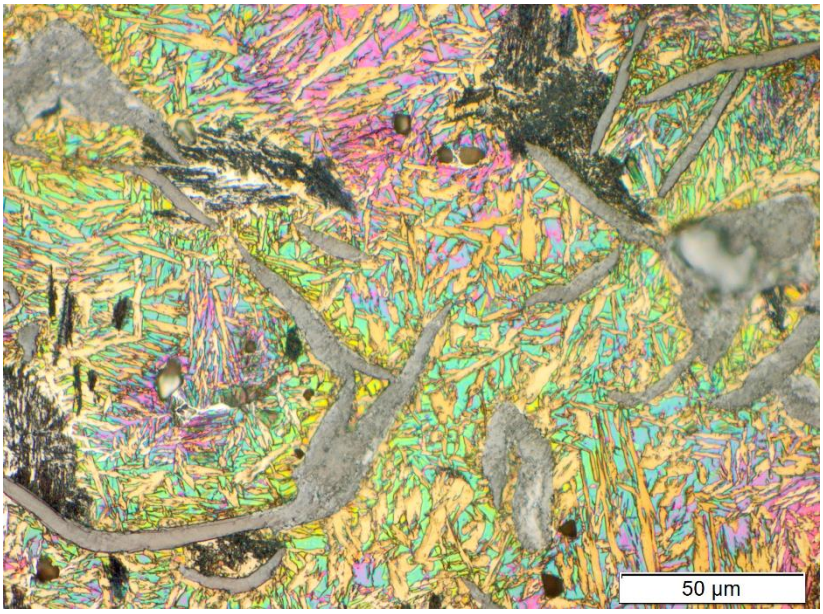

Figure 48. Example of one micrograph from composition 8

5.2.2 Dilatometer

From the dilatometer was taken very useful data to understand what happens with the Mo content increase. Maybe the expansion coefficient is the minor but it deserves to be mention. In the **Table 3** is shown the thermal expansion coefficient and in **Figure 29** is related with the Molybdenum content. It doesn't show a big trend, but it is possible to do the same aggrupation than before. The explanation could be similar. The thermal expansion in the second lineal part is quite bigger than in the first lineal part almost the double. Given that the second part is above the eutectoid line, it could be said that austenite has a big expansion coefficient. That explain the big coefficient for composition 8, which it has ausferrite as matrix. The compositions A, 2 and 3 has an increasing trend with the Mo content, and after the compositions 4, 5 and 6 keep the coefficient constant. A possible reason it could be the same as in the UTS, a refinement of the pearlite increase the expansion but the carbides dissolved in the matrix, made it more rigid, due to the low thermal expansion of both carbon and Mo.

Furthermore, from the dilatometer was taken the measures de volumetric change as it was explained. In the **Figure 30** it was plot, that volumetric changes during the heating and during the cooling. It possible to see that the volumetric change it is bigger in the cooling than in the heating for the composition A, 2, 3, and 4. If one think about the process that the samples have suffered in the dilatometer, and it relates with a diagram TTT that makes sense because the cooling line in the TTT of the dilatometer it would be completely in the pearlite zone due to the slow cooling rate performed in the dilatometer. And the transformation between austenite and pearlite due to the change in the lattices, there is a volumetric change. Then, recalling one of the effects of the Molybdenum mentioned in the theoretical

background, it was that Mo shift the pearlite zone in the TTT diagram as is shown in figure 15. Thus it is suppressed the austempering but similar properties and structure were achieved. As it was said the austempering consists of two parts, first a very fast cooling to avoid the pearlite zone and after an isothermal process during a given time, and finally a slowly cooling. In this case, once the ausferrite start to appear in the microstructure, (in the composition 5) that's mean the Mo shifts enough the pearlite zone and the first cooling (the one done in the foundry) it's getting close to the first cooling of the austempering, the one avoid the pearlite. After, if the sample it is heated and let it with a slow cooling as in the dilatometer, what is being done it is very similar process to austempering. So the result with the composition 5, 6 and 8 it is a volumetric change lower in the cooling than in the heating, because the austenite is promoted. Until the case that in the composition 6 the volumetric change in the cooling almost disappear and in the composition 8 disappear completely.

Finally from the dilatometer it was detected in the curves, a volumetric change around 450^{0}C, in the compositions 5, 6 and 8 during the cooling, and during the heating just it was detected in composition 8 i.e. in the compositions which has more retained austenite. A possible explanation of this phenomenon, it could be that when the austenite doesn't transform itself into pearlite, and it is cooled enough, due to the different expansion coefficient between the Carbon and the Fe, in the austenite lattice don't have enough space for all the C and Fe that were inside when the lattice was expanded. Due to that the lattice it is deformed as the lustration shown in **Figure 49**.

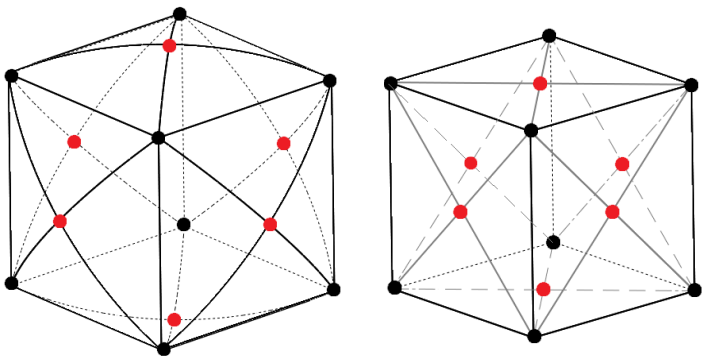

Figure 49. Deformed lattice of austenite.

5.2.3 Differential Scanning Calorimetry

From the DSC data, the heating was used for calculate the conductivity which it is mentioned in the following sections but cooling deserves to be mentioned especially. The cooling it is shown in the figure 32 and around 700 ^{0}C during the eutectic transformation it is possible to see a perfect order, in function of the Mo content. Such order is not possible to see as good in the heating, because in the DSC the material was remelted and cooled under the same condition. This is a prove about the importance of cooling of all the samples, under the same conditions, said in material section in the discussion of the method. The order during the transformation in the graph shows a lower peak as the molybdenum increase, in

order to corroborate that, it was decided to integrate the curve. If it is considered that in the composition 8 no austenite transform into pearlite the in integration on graph 8 it would show the energy necessary to transform the austenite into pearlite. The results of the integration are shown in **Figure 34**. As the results shows a decreasing value. That means each time less austenite is transformed into pearlite.

5.2.4 Laser flash

The results of the diffusivity shown in the **Figure 35**, has an order which, is possible to relate easily with the graphite. The concentrations A, 2 and 4 are the ones with better diffusivity and they have the best graphite from a thermal point of view. They have the ones with more graphite type A. As it was said in the theory the graphite type A has a best thermal properties after type C, but in this case, there is not type C. After in the diffusivity there are another group compound of the samples 6, 5 and 3, which have more graphite type E than A. Finally, the composition 8 it is the one with the worst diffusivity, despite it has more graphite type A than type E, it has a different matrix, asuferrite matrix which has lower diffusivity than pearlitic matrix.

5.2.5 Thermal conductivity

The behavior in the conductivity does not follow any clear pattern, so for future calculations of conductivity I will suggest to remelt the material and cool it under the same conditions, and then take the samples, in order to have more comparable data. As it is possible to see in the cooling of the DSC, the material under the same cooling conditions has an order as function of the molybdenum, but in the heating not, in the heating the values are without any pattern as well, that means the material in the starting conditions is not comparable.

6 Conclusions

Answering the research questions written at the beginning of this report, the present study can conclude:

a. What influence does the molybdenum have on mechanical properties?

The molybdenum has a significant influence in the UTS. In lower quantities less than 0,37% it behaves as a perlitic refiner therefore the UTS increase. Larger quantities of Molybdenum forms carbides, which it is not good from the UTS's view but this effect is counteracted by the ausferrite formation in bigger quantities. While the molybdenum content decreases, there are a concentration where the Molybdenum it is not enough for the formation of ausferrite but it is enough for the formation of the necessary carbides to worsen the properties achieved by the perlite's refinement. This concentration is with the 0,48% of Mo.

a. What influence does the molybdenum have on thermal properties?

In thermal properties, not clear conclusions were achieved, but it is possible to say that when the full ausferrite matrix is achieved, the conductivity is quite lower, than a pearlite matrix.

b. Does molybdenum have any influence on the graphite?

In the graphite, is not detected any clear behavior as the molybdenum increase. The graphite type, graphite fraction are random parameters as molybdenum function.

c. Does molybdenum have any influence on the microstructure?

The molybdenum has a significant influence in the microstructure, since it was detected a refinement of the pearlite, generation of carbides and the appearance of the ausferrite in high molybdenum content.

d. How does molybdenum influence on the solid state transformation?

It can be affirmed that, molybdenum deforms the solid state transformation. In such a way that decrease the volume change and the latent heat during the transformation. In other words, molybdenum shifts the pearlite transformation as molybdenum content increases until at high molybdenum content the solid state transformation disappears.

7 Future work

- Check compositions with more Mo, and see if the UTS continues increasing or not.

- The influences of Mo in a casting with a faster cooling rate in order to achieved ausferrite with less Mo content. Maybe better properties in the full ausferrite matrix are achieved because less carbides are formed.

- Study the influence of Mo in the graphite shape, in samples with the same cooling conditions in order to do not alter the graphite with other factors.

- Study the microstructure of the dilatometer samples and check if there is more ausferrite than in the initial microstructure.

- Measure the distance between the lamellae of the perlitic with the SEM and perform a microhardness of the matrix in order to verify the refinement of the pearlite.

8 References

[1]J R. Davis, ASM specialty handbook: cast irons: ASM international, 1996.

[2] "49st Census of World Casting Production - 2015," Modern Casting, pp. 26-31, 2015. Available: http://www.foundryinfo-india.org/statistics/Dec15%20Census.pdf

[3] Z. Dauter and M. Jaskolski, "How to read (and understand) Volume A of International Tables for Crystallography: an introduction for nonspecialists," Journal of Applied Crystallography, vol. 43, pp. 1150-1171, Oct 2010.

[4] J. A. V. OLAY, "Crystallography geometry and structures," Materials science Universidad de Oviedo, 2014.

[5] F. C. Campbell, Elements of metallurgy and engineering alloys: ASM International, 2008.

[6] J. A. V. OLAY, "Steel and cast," Materials science Universidad de Oviedo, 2014.

[7] G. Krauss, "Principles of heat treatment of steel," American Society for Metals, 1980, p. 291, 1980.

[8] G.M.Goodrich, "introduction to Cast Irons" in ASM Handbook, ASM International, pp. 785 - 811, 2008.

[9] C. F. Walton, Gray and Ductile Iron Castings Handbook: Gray and Ductile Iron Founder's Society Incorporated, 1971.

[10]P. Kumar. (2013). Phase Diagram. Available: http://www.slideshare.net/Pramodkumar2016/phase-diagram-28332778

[11] G. Krauss, "Steels: heat treatment and processing principles," heat treatment and processing principles, ASM International, p. 497, 1990.

[12] M. Ferry and W. Xu, "Microstructural and crystallographic features of ausferrite in as-cast gray iron," Materials characterization, vol. 53, pp. 43-49, 2004.

[13] D. M. Stefanescu, "Classification and basic metallurgy of cast iron," ASM International, Metals Handbook. Tenth Edition., vol. 1, pp. 3-11, 1990.

[14] I. Minkoff, The physical metallurgy of cast iron: Wiley, 1983.

[15] M. C. Flemings, "Solidification processing," Metallurgical transactions, vol. 5, pp. 2121-2134, 1974.

[16] J. Dantzig and M. Rappaz, "Solidification, 2009," ed: EPFL Press, Lausanne, Switzerland, 2009.

[17] J. Campbell, Castings: Butterworth-Heinemann, 2003.

[18] R. Gundlach, J. Janowak, S. Bechet, and K. Rohrigtt, "On the problems with carbide formation in gray cast iron," in MRS Proceedings, 1984, p. 251.

[19] A. Diószegi, "Professor Casting Tecnology, Tekniska Högskolan i Jönköping, Private communication,", 2012.

[20] R. F. Mehl and W. C. Hagel, "The austenite: pearlite reaction," Progress in Metal Physics, vol. 6, pp. 74-134, 1956.

[21] G. Rivera, R. Boeri, and J. Sikora, "Solidification of gray cast iron," Scripta Materialia, vol. 50, pp. 331-335, 2004.

[22] D. Aliya, "Physical metallurgy concepts in interpretation of microstructures," Materials Park, OH: ASM International, 2004., pp. 44-70, 2004.

[23] N. Lepora, "The elements: Molybdenum," The elements: Molybdenum. Marshall Cavcndish 8enchmark, New York, 2007.

[24] K. Hayrynen, D. Moore, and K. Rundman, "Tensile properties and microstructural analysis of Cu-Mo gray cast irons," in One Hundred Second Annual Meeting of the American Foundrymen's Society, 1998, pp. 665-671.

[25] V. L. Diaconu, T. Sjögren, P. Skoglund, and A. Diószegi, "Influence of molybdenum alloying on thermomechanical fatigue life of compacted graphite irons," International Journal of Cast Metals Research, vol. 25, pp. 277-286, 2012/10/01 2012.

[26] W. Xu, M. Ferry, and Y. Wang, "Influence of alloying elements on as-cast microstructure and strength of gray iron," Materials Science and Engineering: A, vol. 390, pp. 326-333, 2005.

[27] W. Xu, M. Ferry, and Y. Wang, "The effect of ausferrite formation on the mechanical properties of gray iron," Scripta materialia, vol. 51, pp. 705-709, 2004.

[28] J. Bevan and W. Scholz, "Effects of Mo on Transformation Characteristics and Properties of High-Strength Ductile Irons," Transactions of the American Foundrymen's Society., vol. 85, 1977.

[29] D. R. P. Askeland, Pradeep P, "The science and engineering of materials," The science and engineering of materials, 2006.

[30] T. Sjögren, "Influences of the graphite phase on elastic and plastic deformation behaviour of cast irons," 2007.

[31] "Method, tecnique, Applications," in Brochure DIL, ed: Netzsch Group, Dilatometer Series DIL 402C., 2016.

[32] "Method, tecnique, Applications," in Brochure DSC 404 C, ed: Netzsch Group, Differential Scaning Calorimetry-DSC 404 C, 2016.

[33] "Method, tecnique, Applications," in Brochure LFA, ed: Netzsch Group, Laser Flash Analysis-LFA. , 2016.

[34] D. Holmgren, "Review of thermal conductivity of cast iron," International Journal of Cast Metals Research, vol. 18, pp. 331-345, 2005.

[35] M. Selin, "Tensile and thermal properties in compacted graphite irons at elevated temperatures," Metallurgical and Materials Transactions A, vol. 41, pp. 3100-3109, 2010.

[36] D. Holmgren and I. L. Svensson, "Thermal conductivity–structure relationships in grey cast iron," International Journal of Cast Metals Research, vol. 18, pp. 321-330, 2005.

[37] D. Holmgren, A. Dioszegi, and I. Svensson, "Effects of nodularity on thermal conductivity of cast iron," International Journal of Cast Metals Research, vol. 20, pp. 30-40, 2007.

[38] V. Fourlakidis, Dendritic Morphology and ultimate Tensile Strength in Lamellar Graphite Iron: School of Engineering, Jönköping University, department of mechanical Engineering, 2014.

9 Appendices

Appendix 1 Chemical composition of each casting.

Appendix 2. Curves of the dilatometer.

Appendix 3. Diffusivity.

Appendix 4. Tensile test

Appendix 5. Matrix micrographs.

Appendix 6. Fracture micrographs.

9.1 Chemical composition of each casting

The chemical composition of the seven alloys that were studied.

Table 4. Composition of the studied samples

Material ID		A	2	3	4	5	6	8
Chemical Composition	**C**	3,40	3,26	3,24	3,28	3,25	3,26	3,24
	Si	1,89	1,89	1,89	1,9	1,88	1,89	1,86
	Mn	0,57	0,60	0,60	0,56	0,56	0,58	0,61
	P	0,05	0,05	0,05	0,05	0,05	0,05	0,03
	S	0,089	0,09	0,09	0,08	0,09	0,08	0,09
	Cr	0,15	0,14	0,13	0,13	0,13	0,13	0,13
	Ni	0,07	0,06	0,06	0,06	0,06	0,06	0,05
	Mo	**0,05**	**0,16**	**0,37**	**0,48**	**0,65**	**0,81**	**0,96**
	Cu	0,90	0,82	0,78	0,76	0,80	0,81	0,93
	Sn	0,05	0,05	0,06	0,04	0,05	0,05	0,05
	V	0,02	0,02	0,02	0,02	0,02	0,02	0,02
	Ti	0,02	0,01	0,01	0,01	0,01	0,01	0,01
	CE	3,90	3,91	3,89	3,93	3,89	3,91	3,87

9.2 Curves of the dilatometer

Plots done with excel from the data of the dilatometer, relative elongation variation of the sample with the temperature. Where the red lines represent the heating process and the blue ones the cooling process.

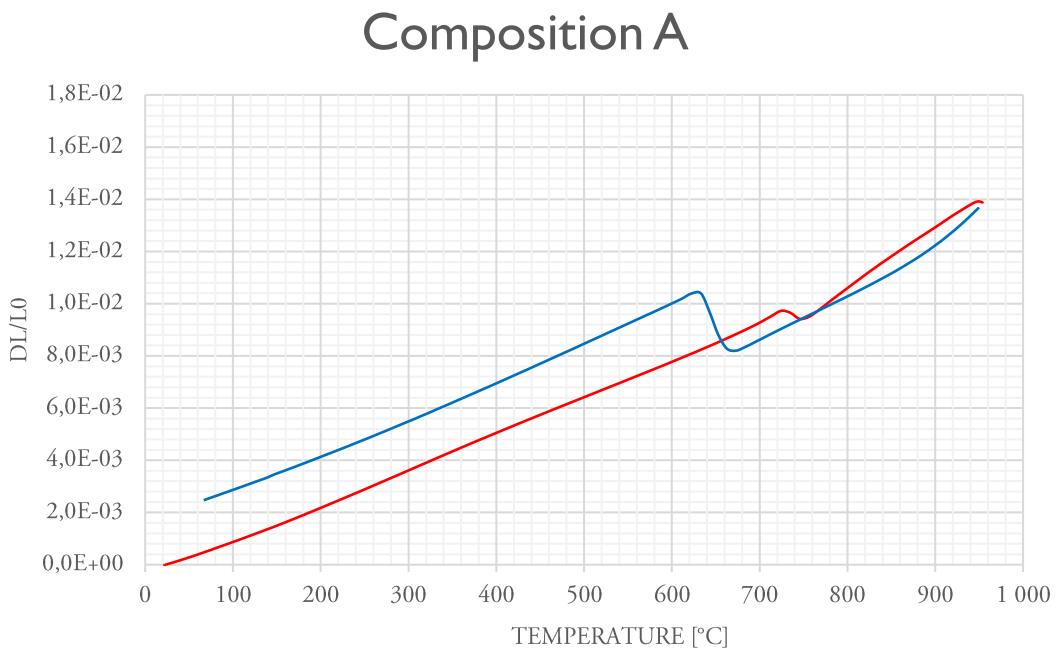

Figure 50. Dilatometer curve of composition A.

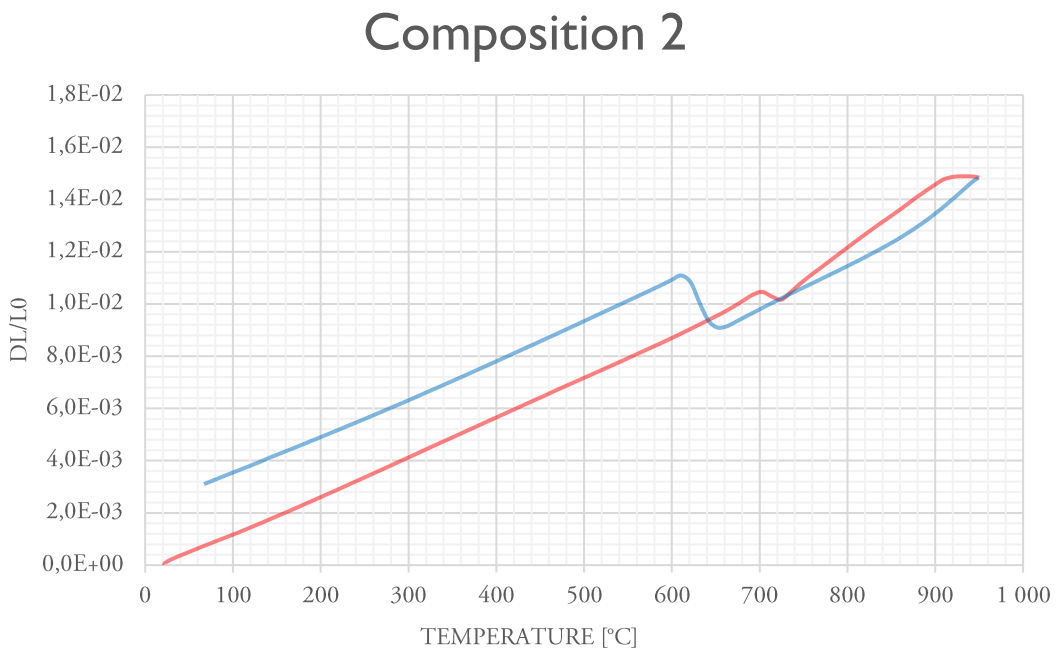

Figure 51. Dilatometer curve of composition 2.

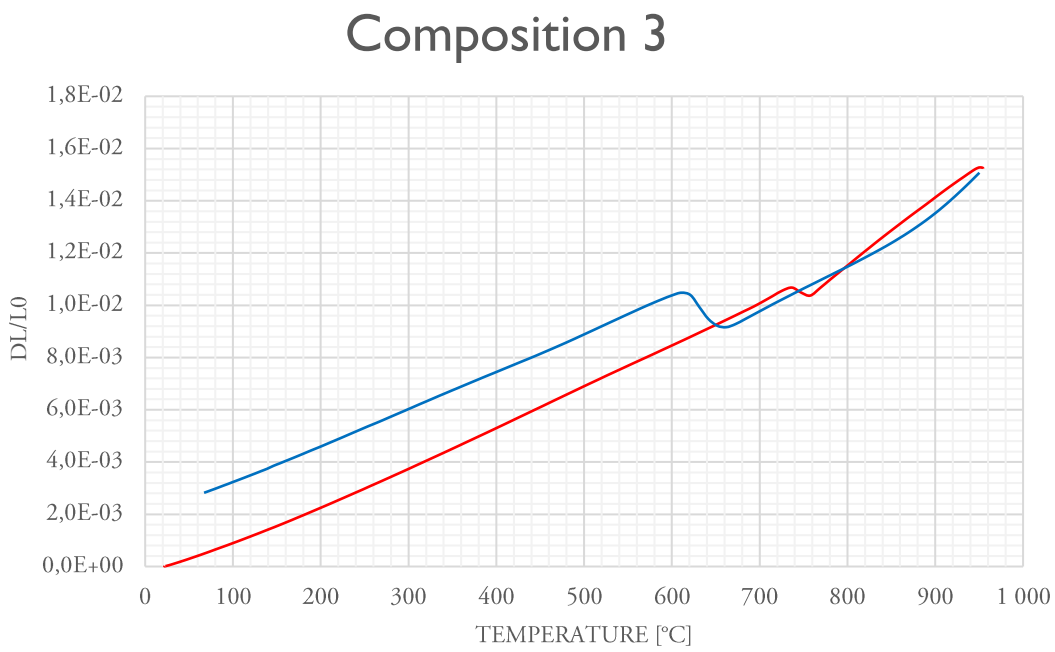

Figure 53. Dilatometer curve of composition 3.

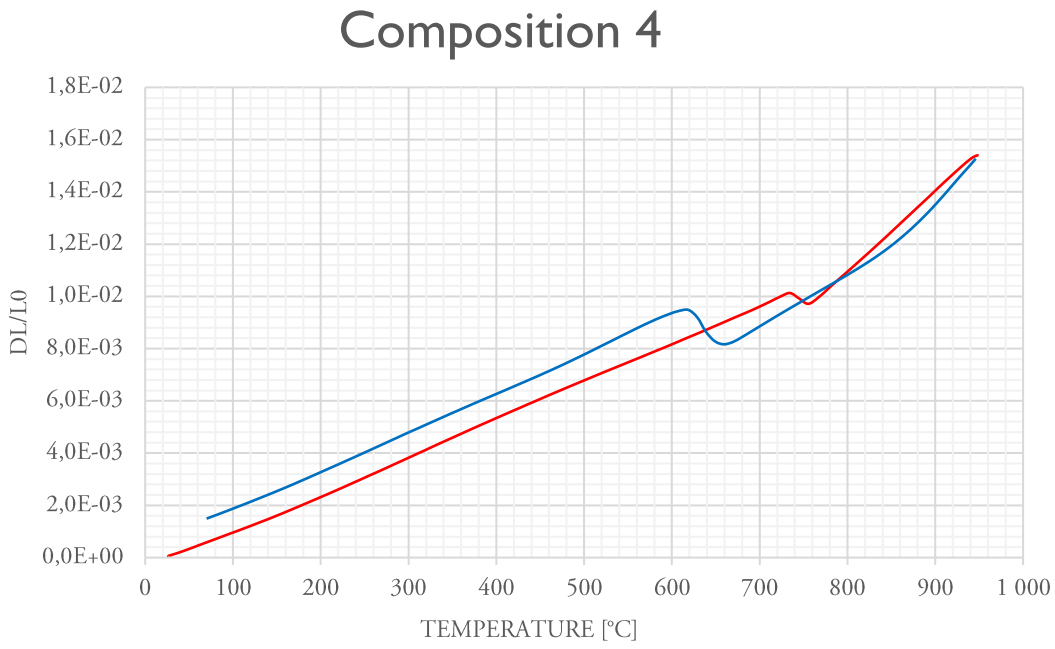

Figure 52. Dilatometer curve of composition 4.

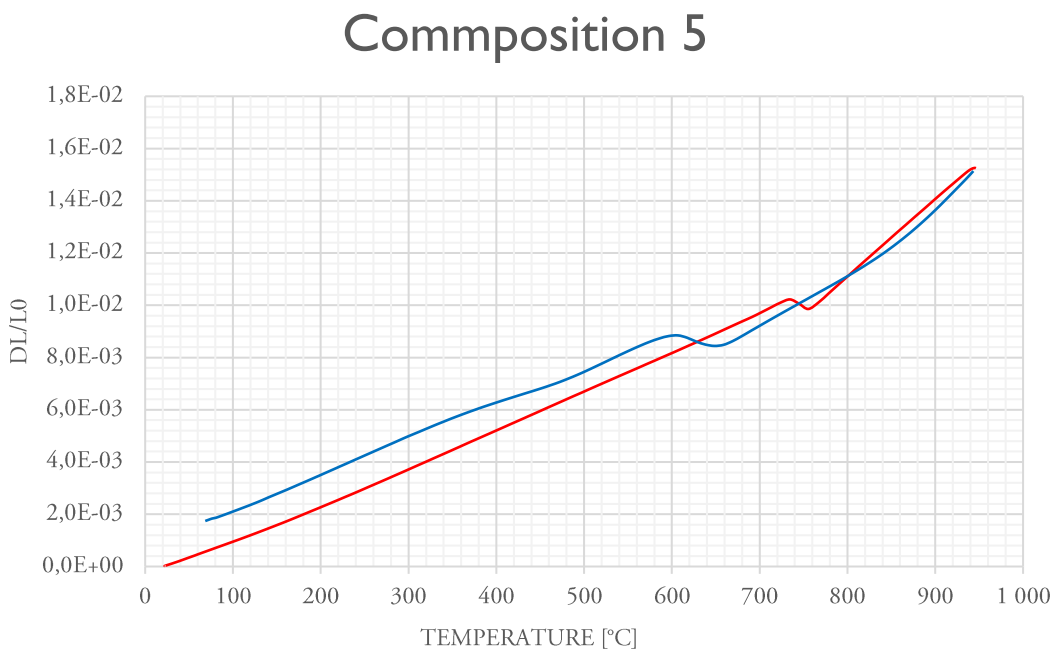

Figure 54. Dilatometer curve of composition 5.

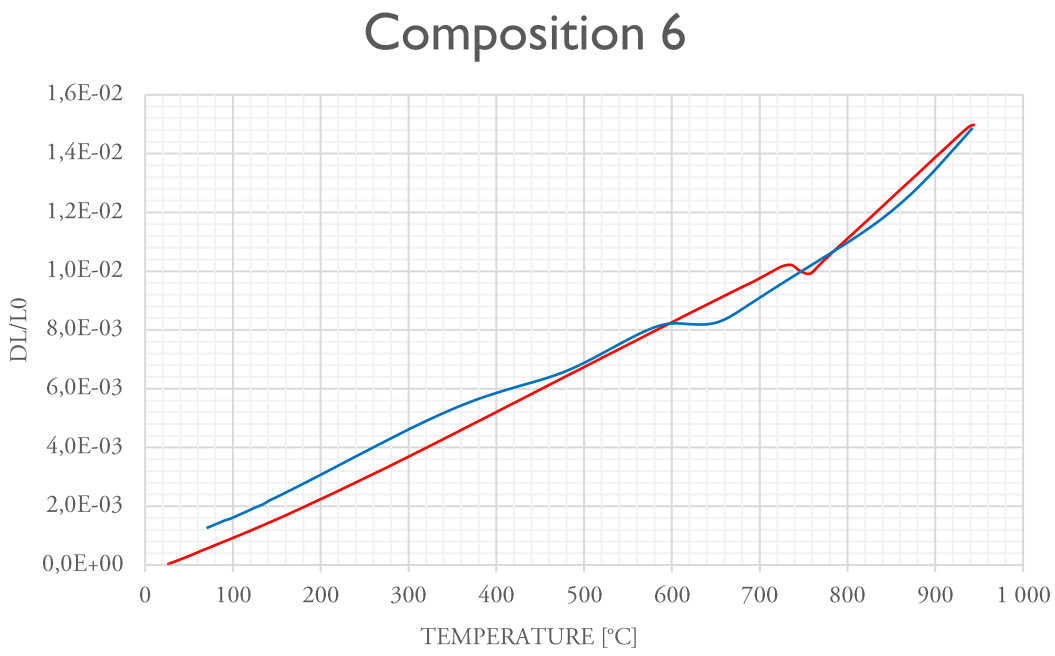

Figure 55. Dilatometer curve of composition 6.

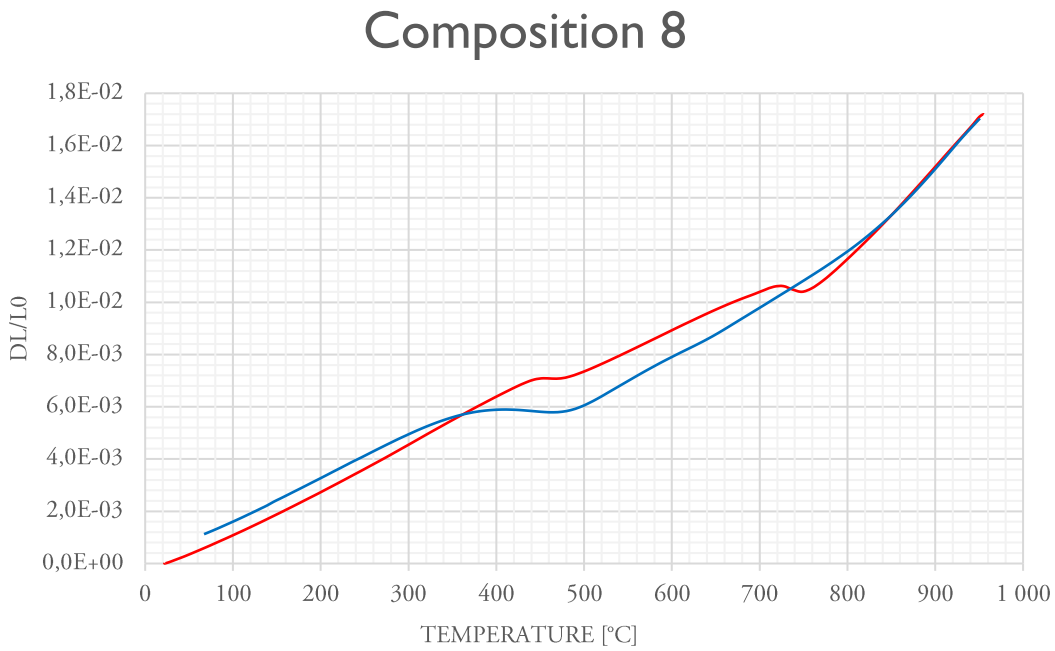

Figure 56. Dilatometer curve of composition 8.

9.3 Diffusivity

The data form the laser flash is shown in the table below, with the average of values and its standard deviation.

Table 5. Diffusivity data.

	Samples	***A***	***2***	***3***	***4***	***5***	***6***	***8***
Shots 1 to 10 at 25 ^{0}C	Diffusivity mm²/s	14,289	14,039	12,744	13,393	13,291	13,393	11,508
	StdDev mm²/s	0,588	0,169	0,621	0,767	0,791	0,767	0,723
Shots 11 to 15 at 150 ^{0}C	Diffusivity mm²/s	12,167	11,968	11,283	11,596	11,489	11,596	10,162
	StdDev mm²/s	0,112	0,0485	0,016	0,057	0,083	0,057	0,041
Shots 16 to 20 at 300 ^{0}C	Diffusivity mm²/s	10,306	10,36	9,651	9,86	9,898	9,86	8,888
	StdDev mm²/s	0,115	0,0295	0,019	0,13	0,081	0,13	0,06
Shots 21 to 25 at 450 ^{0}C	Diffusivity mm²/s	8,77	8,871	8,23	8,574	8,412	8,574	8,203
	StdDev mm²/s	0,038	0,0705	0,099	0,086	0,173	0,086	0,124
Shots 26 to 30 at 600 ^{0}C	Diffusivity mm²/s	7,017	7,231	6,599	6,867	6,95	6,867	6,736
	StdDev mm²/s	0,467	0,353	0,472	0,296	0,199	0,296	0,562
Shots 31 to 35 at 750 ^{0}C	Diffusivity mm²/s	5,672	5,968	6,118	5,764	5,322	5,764	6,215
	StdDev mm²/s	0,494	0,475	0,543	0,504	0,841	0,504	0,805
Shots 36 to 40 at 900 ^{0}C	Diffusivity mm²/s	7,415	8,592	7,131	7,078	7,503	7,078	7,134
	StdDev mm²/s	0,977	0,379	0,5	0,522	0,664	0,522	0,808

9.4 Tensile test

The tables were done in excel from the data of the tensile test, and it is possible to see the UTS, the elongation and the E_{mod} of each specimen.

Table 6. Results of the UTS.

	UTS [MPa]				*Differences in the same cone*		*Statistic calculation*	
Mat ID	***A II***	***A III***	***B II***	***B III***	***A***	***B***	***Average***	***StdDev***
A	238,6	222,7	227,7	227,1	7%	0%	229,03	5,86
2	237,2	234,2	249,2	239,8	1%	4%	240,10	5,62
3	290,7	260,8	252	285	11%	12%	272,13	16,16
4	277,2	267,3	250,5	256,6	4%	2%	262,90	10,21
5		298,9	257,7	276,5		7%	277,70	16,84
6	272	288,7	298,9		6%		286,53	11,09
8	358,2	372,2	330,6		4%		353,67	17,28

Table 7. Results of the E modulus.

	Emod [GPa]				*Differences in the same cone*		*Statistic calculation*	
Mat ID	**A II**	**A III**	**B II**	**B III**	**A**	**B**	**Average**	**StdDev**
A	96,7	111	79,5	102	13%	22%	97,30	11,48
2	83,3	90,6	86,3	92,6	8%	7%	88,20	3,63
3	120	107	121	109	12%	11%	114,25	6,30
4	118	131	111	133	10%	17%	123,25	9,12
5		85,7	92	107		14%	99,50	8,93
6	136	98,9	115		38%		116,63	15,19
8	128	87,7	122		46%		112,57	17,75

Table 8. Results of the elongation.

	dL at Fmax				*Differences in the same cone*		*Statistic calculation*	
Mat ID	**A II**	**A III**	**B II**	**B III**	**A**	**B**	**Average**	**StdDev**
A	0,2134	0,1871	0,1296	0,1541	14%	16%	0,17	0,03
2	0,1878	0,1742	0,1243	0,1766	8%	30%	0,17	0,02
3	0,1843	0,1691	0,148	0,1872	9%	21%	0,17	0,02
4	0,1281	0,178	0,172	0,1585	28%	9%	0,16	0,02
5		0,2482	0,1445	0,1716		16%	0,19	0,04
6	0,1339	0,1747	0,2007		23%		0,17	0,03
8	0,1778	0,2203	0,157		19%		0,19	0,03

This color correspond with missing data due to different technical problem.

9.5 Matrix micrographs

The micrographs of the matrix after the etching are shown below, they are presented in different groups, each group belong to one concentration, and there are six different micrographs with different magnification.

A

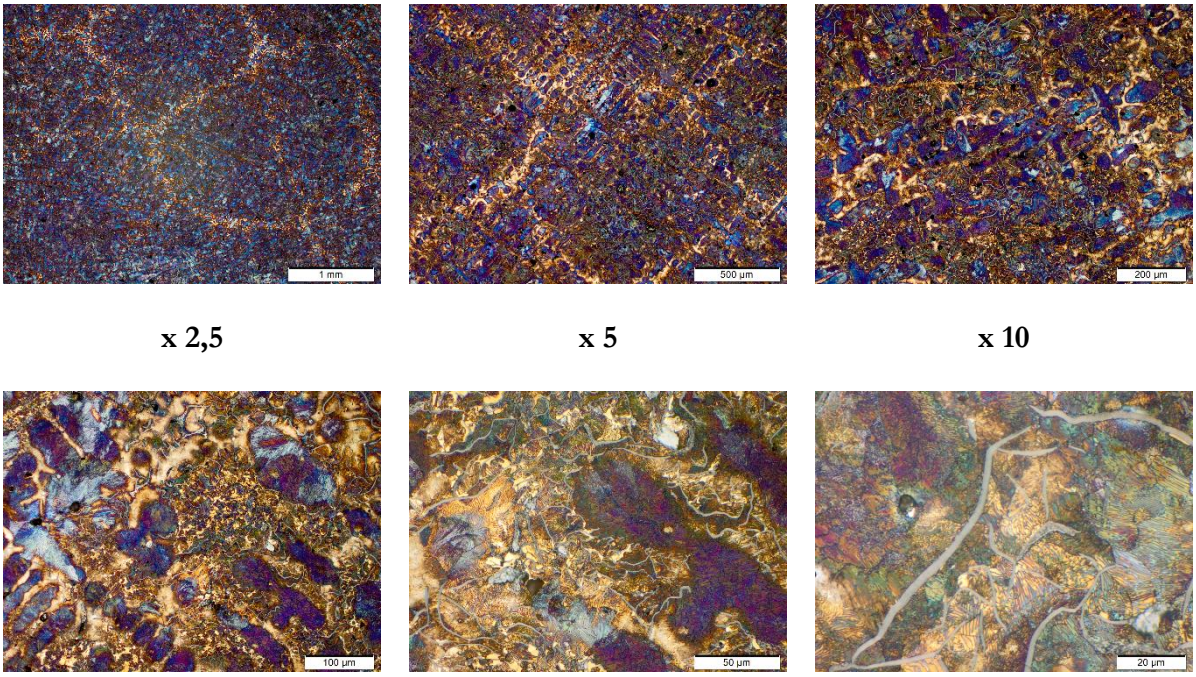

x 2,5 **x 5** **x 10**

x 20 **x 50** **x 100**

Figure 57. Micrographs from the matrix of composition A.

2

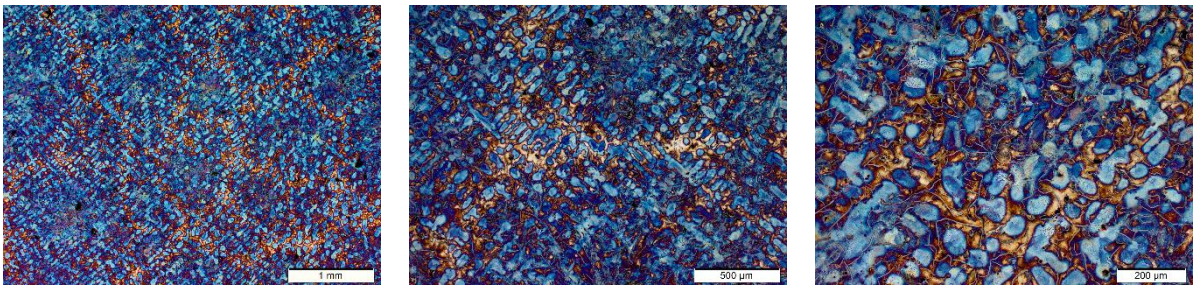

x 2,5 **x 5** **x 10**

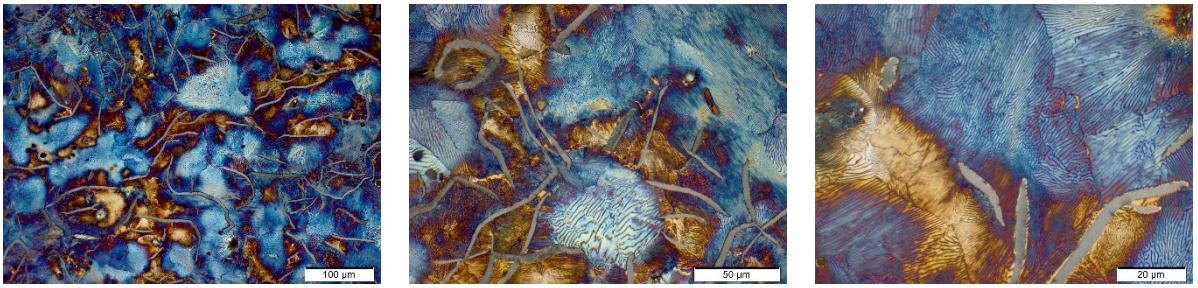

x 20 **x 50** **x 100**

Figure 58. Micrographs from the matrix of composition 2.

3

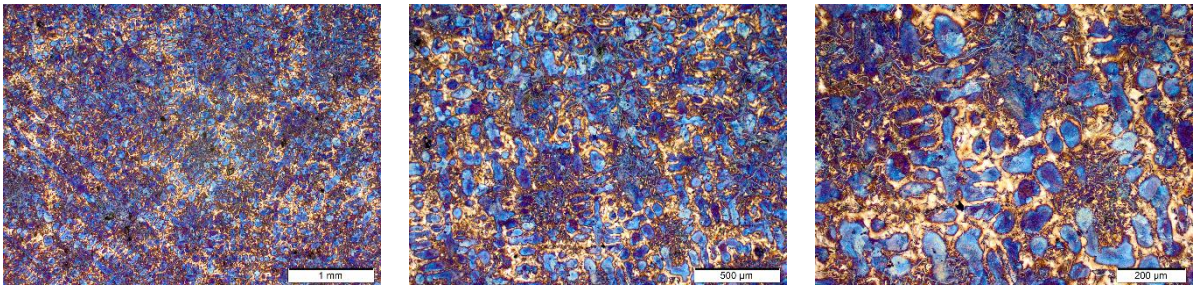

x 2,5 **x 5** **x 10**

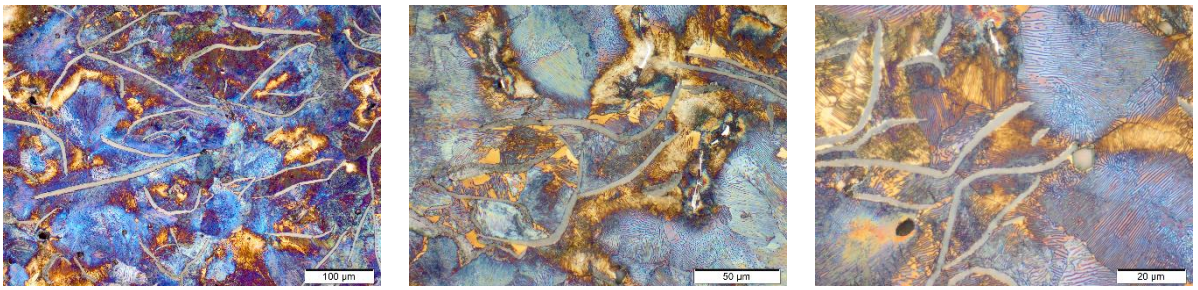

x 20 **x 50** **x 100**

Figure 59. Micrographs from the matrix of composition 3.

4

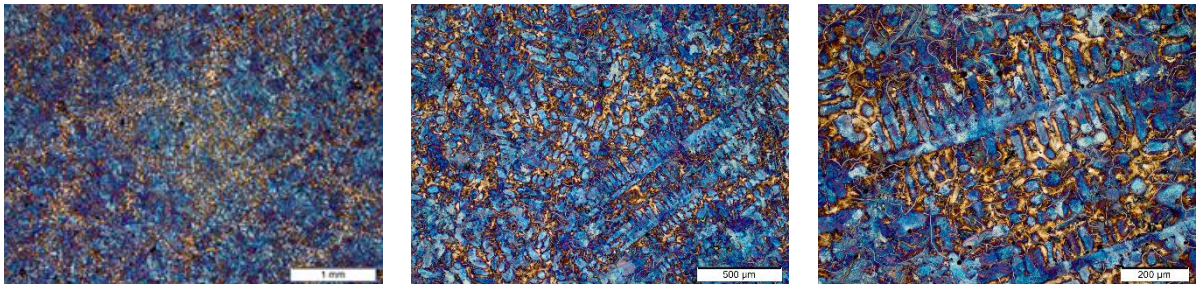

x 2,5 **x 5** **x 10**

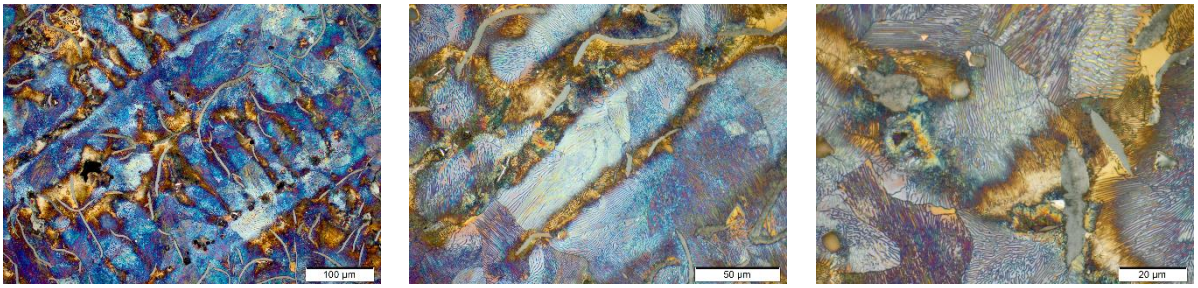

x 20 **x 50** **x 100**

Figure 60. Micrographs from the matrix of composition 4.

5

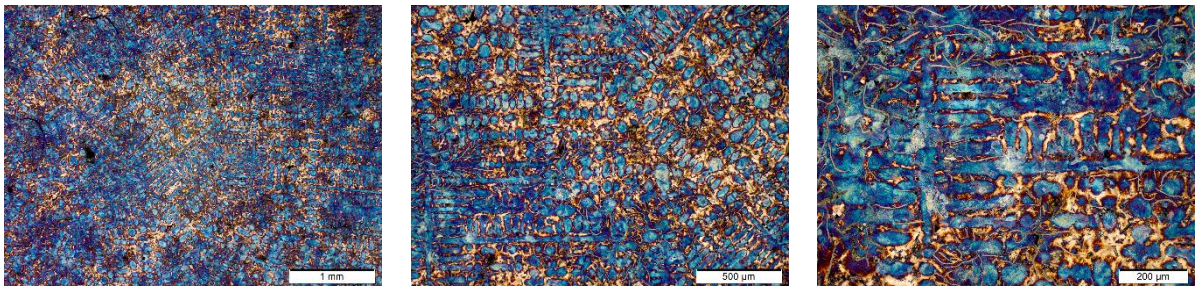

x 2,5 **x 5** **x 10**

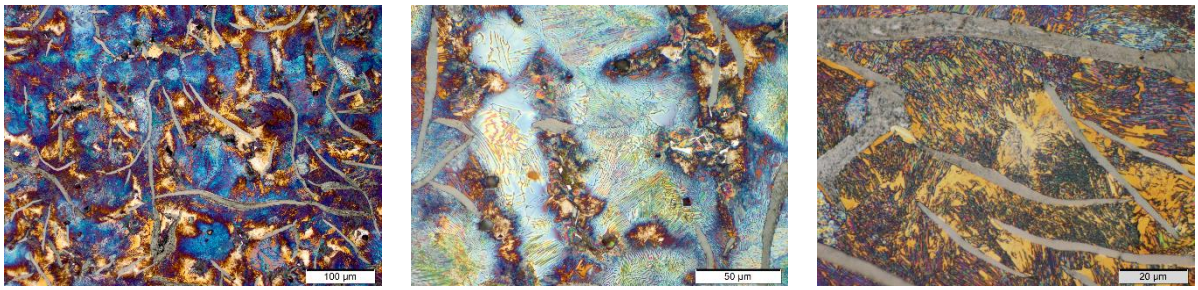

x 20 **x 50** **x 100**

Figure 61. Micrographs from the matrix of composition 5.

6

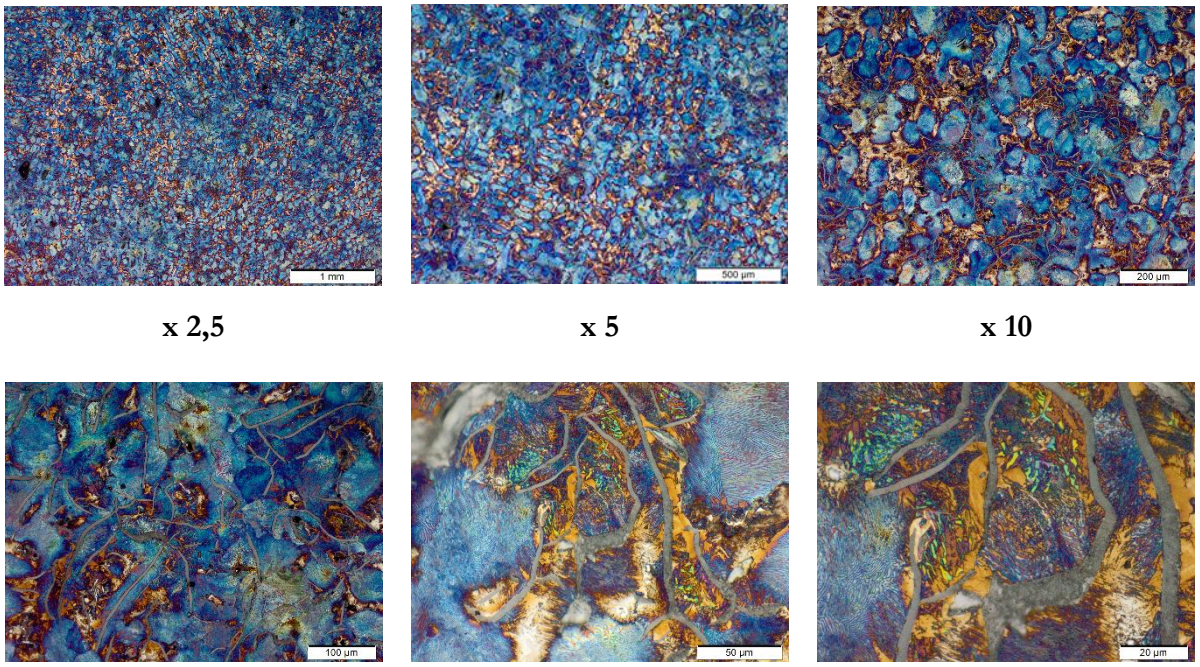

x 2,5 **x 5** **x 10**

x 20 **x 50** **x 100**

Figure 62. Micrographs from the matrix of composition 6.

8

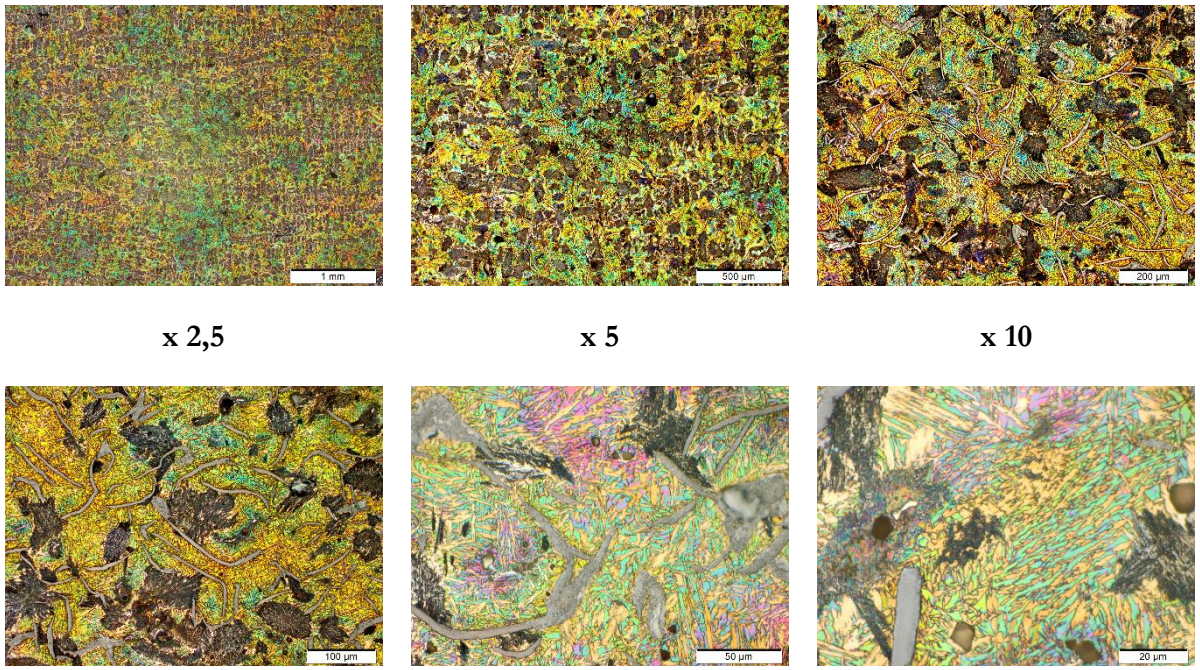

x 2,5 **x 5** **x 10**

x 20 **x 50** **x 100**

Figure 63. Micrographs from the matrix of composition 8.

9.6 Fracture micrographs

The fracture micrographs unetching are shown in the following this appendix. The micrographs were taken with 2.5 magnification and after merged with Adove Photoshop.

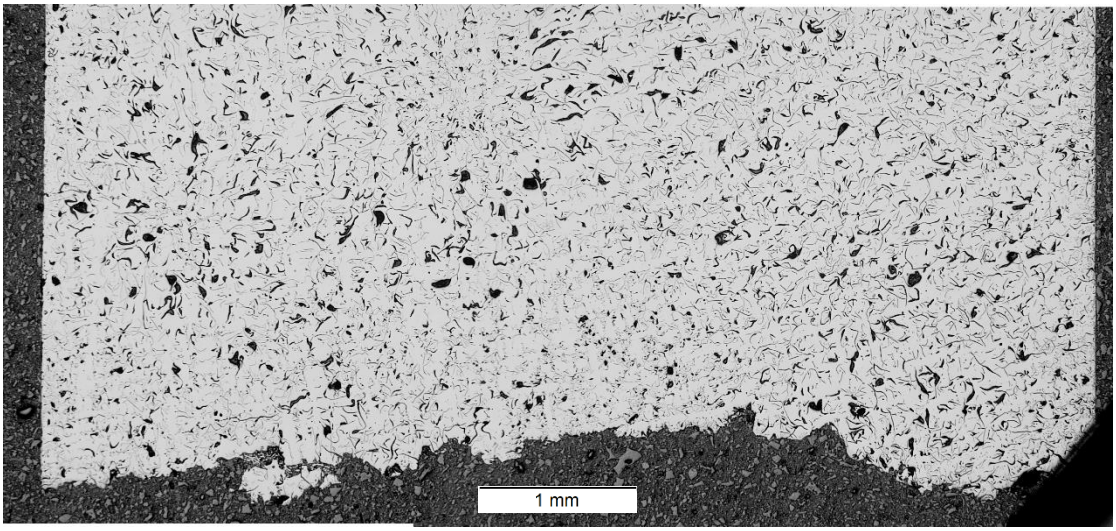

Figure 64. Fracture of the composition A.

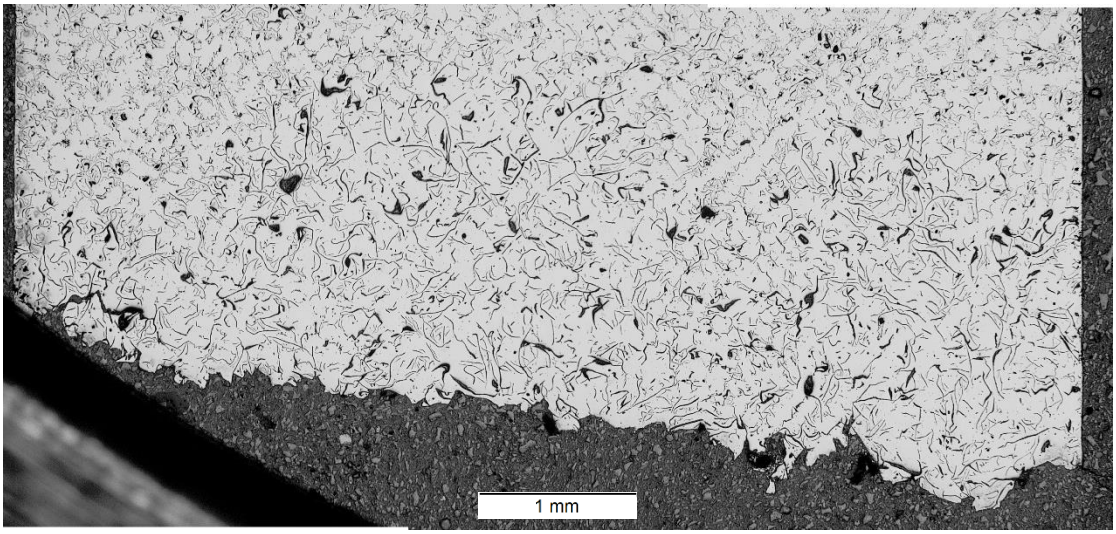

Figure 65. Fracture of composition 2.

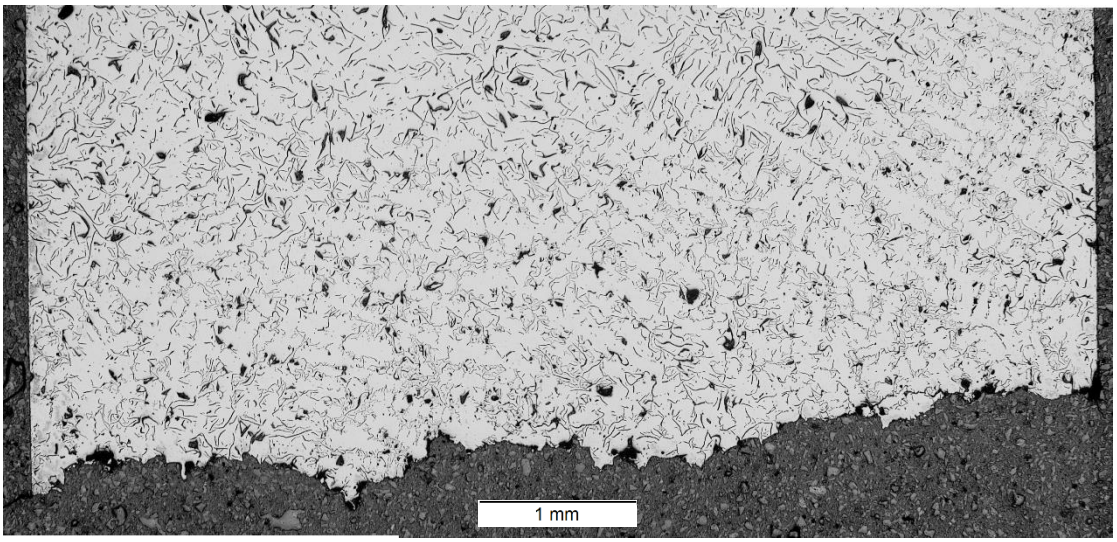

Figure 66. Fracture of composition 3.

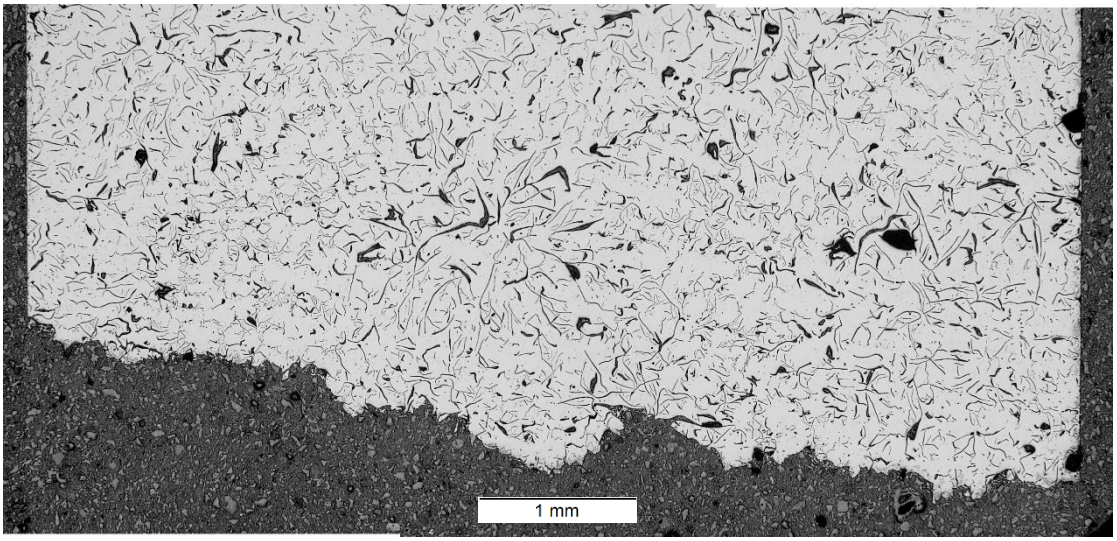

Figure 67. Fracture of composition 4.

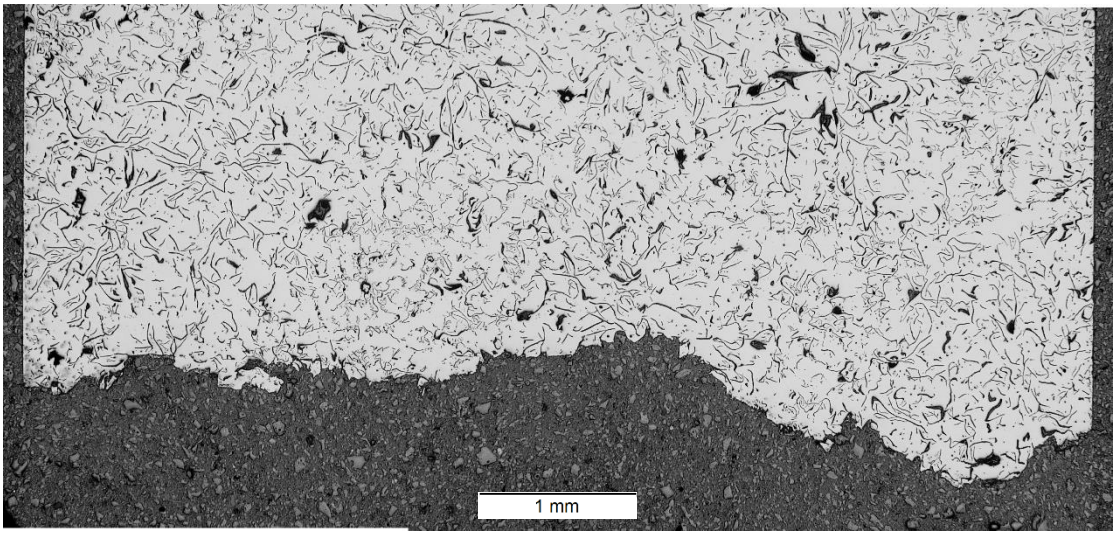

Figure 68. Fracture of composition 5.

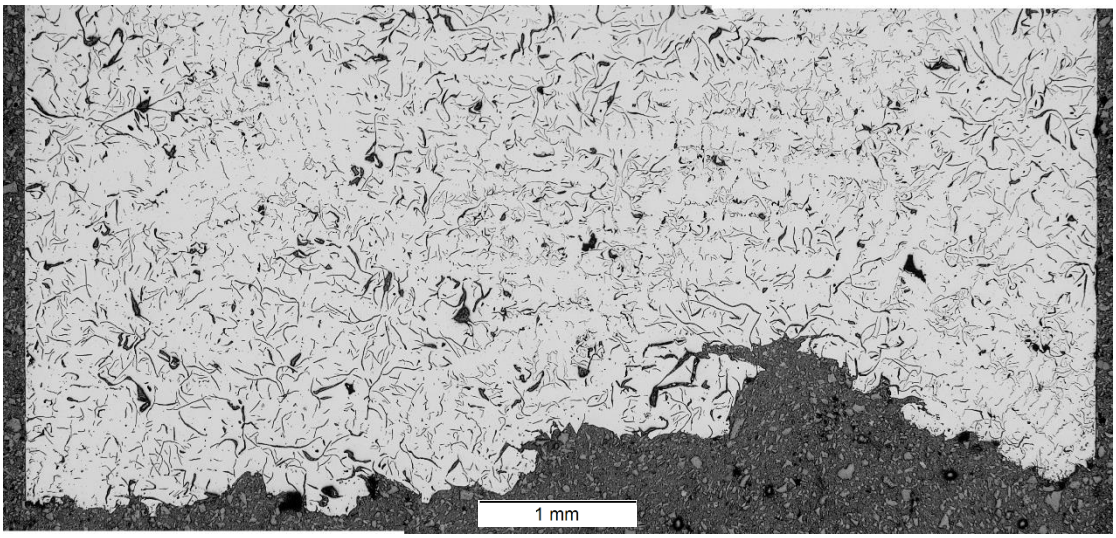

Figure 69. Fracture of composition 6.

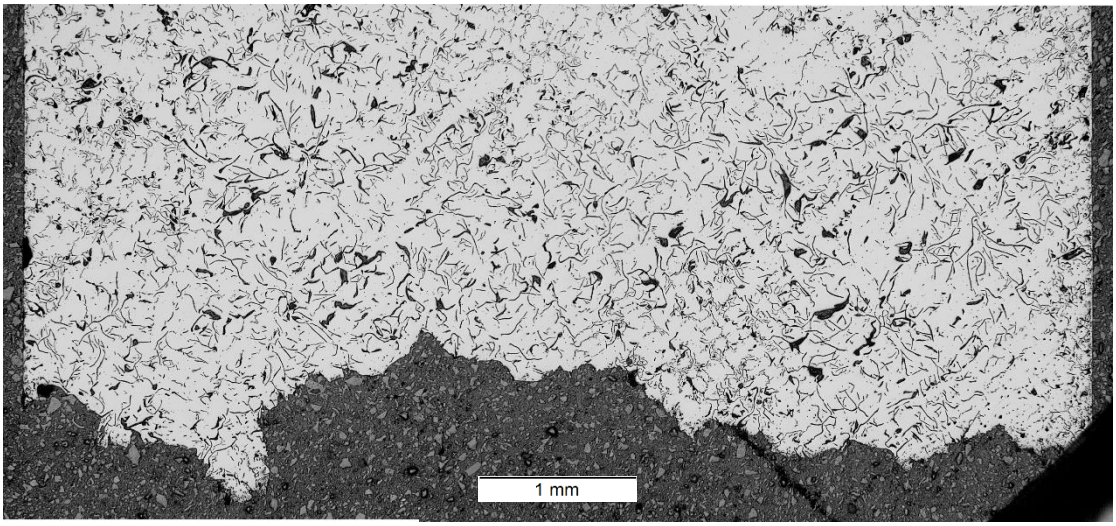

Figure 70. Figure of comosition 8.